Summer 8-15-2020

Delineating the Role of MiR-124 for the Activation of Neuronal Program

Ya-Lin Lu
Washington University in St. Louis

WASHINGTON UNIVERSITY IN ST. LOUIS

Division of Biology and Biomedical Sciences
Developmental, Regenerative and Stem Cell Biology

Dissertation Examination Committee:
Andrew S. Yoo, Chair
Shiming Chen
Harrison Gabel
Shin-ichro Imai
Kristen Kroll

Delineating the Role of MiR-124 for the Activation of Neuronal Program

by
Ya-Lin Lu

A dissertation presented to
The Graduate School
of Washington University in
partial fulfillment of the
requirements for the degree
of Doctor of Philosophy

August 2020
St. Louis, Missouri

Table of Contents

List of Figures

List of Tables

Chapter 3

Acknowledgments

My thesis work would not have been possible without the mentorship of my advisor, Dr. Andrew Yoo. His unwavering support and confidence in my scientific work has allowed me to come this far. To past and current Yoo lab members, I appreciate all your help and I am forever grateful for your friendships. I would also like to thank the faculties and staff in DBBS and the Department of Developmental Biology for this amazing learning experience. I am indebted to my two previous mentors, Dr. Jun-An Chen and Dr. Matthew Jones-Rhoades. Both have taught me so much early in my scientific career. To my classmates and peers, thank you for making this journey memorable. And of course, nothing would have been possible without the unconditional support from my family.

Ya-Lin Lu

Washington University in St. Louis

August 2020

Abstract of the Dissertation

Delineating the Role of MiR-124 for the Activation of Neuronal Program

by

Ya-Lin Lu

Doctor of Philosophy in Biology and Biomedical Sciences

Developmental, Regenerative and Stem Cell Biology

Washington University in St. Louis, 2020

Andrew S. Yoo, Chair

The ectopic expression of two brain-enriched microRNAs (miRNAs), miR-9/9* and miR-124 (miR-9/9*-124), can robustly and efficiently reprogram human skin fibroblasts into neurons. The miRNAs act as repressors of non-neuronal genes in fibroblasts for the induction of the neuronal program. This process is analogous to neurogenesis in vivo when the expression of miR-9/9* and miR-124 represses anti-neurogenic genes such as REST or NRSF (neuron-restrictive silencer factor/repressor element-1 silencing transcription factor). Although we have some mechanistic insights into how miR-9/9*-124 drives fate conversion by acting as negative regulators of gene expression, little remained understood of the role of miRNAs as positive regulators of gene expression for the activation of neuronal fate. In this thesis, we present our current understanding of how miR-9/9*-124 drives neuronal reprogramming as well as the mechanistic insights into

how miR-9/9*-124 can promote expression of neuronal genes. Based on Argonuate (AGO) HITS-CLIP, we uncovered that AGO is bound to neuronal transcripts that are progressively upregulated during reprogramming. Such observation suggests that contrary to the canonical repressive roles of miRNAs, miR-9/9*-124 may be playing a positive role in the expression of bound neuronal transcripts. Using PTB family of RNA-binding proteins as an example, we delineate a mechanism by which miR-124 can simultaneously repress PTBP1, the non-neuronal PTB homolog, while promoting the upregulation of PTBP2, the neuronal PTB homolog, in neurons. This process requires the synergism of miRNA targeting as well as a family of neuronal ELAVL proteins (nELAVLs). We further showed that this miRNA- and nELAVL-mediated upregulation of PTBP2 is neither unique to the conversion process nor PTBP2 transcript alone, but also in primary human neurons and is likely a mechanism used to regulate other neuronal transcripts. With PTBP2 expression induced in neurons, PTBP2 is involved in the alternative splicing of numerous neuronal transcripts. Such transcript includes a subunit of the chromatin remodeling complex, DPF1. Although detailed function of DPF1 remains unclear in neurons, different PTBP2-mediated DPF1 spliced isoforms are likely involved in the interaction of different modified histones for the establishment of a neuronal chromatin landscape.

Chapter 1: Introduction

In part from:

Mechanistic insights into microRNA-induced neuronal reprogramming of human adult fibroblasts.

Ya-Lin Lu & Andrew S. Yoo

Front. Neurosci. 02 August 2018

Overcoming epigenetic barriers through direct cellular reprogramming has allowed scientists to rapidly acquire cell types of interest for regenerative therapies and disease modeling. Direct conversion of mouse fibroblasts into functional neurons have been demonstrated through the use of transcription factors (Blanchard et al., 2015; Chanda et al., 2014; Son et al., 2011; Vierbuchen et al., 2010). Empirically, however, obtaining mature human neurons from adult human fibroblasts with transcription factors have been challenging (Caiazzo et al., 2011). To enhance reprogramming efficiency and to promote neuronal maturation, small chemical molecules (Ladewig et al., 2012; Liu et al., 2013; Pfisterer et al., 2016; Smith et al., 2016) and RNA molecules, miRNAs (Abernathy et al., 2017a; Ambasudhan et al., 2011; Victor et al., 2014; Yoo et al., 2011), have been used in conjunction with transcription factors to robustly generate functional neurons from human fibroblasts. The mechanism(s) by which miR-9/9* and miR-124 collectively drive robust neuronal fate conversion remains an ongoing investigation, but by examining specific microRNA targets, my thesis work aims to elucidate how miRNAs promote the neuronal program during the direct conversion of human fibroblasts to neurons.

MiR-9/9* and miR-124 (miR-9/9*-124) are efficient reprogramming effectors that, when ectopically expressed in human adult fibroblasts (HAFs), induce an extensive reconfiguration of the chromatin accessibility landscape leading to the erasure of fibroblast fate and activation of the neuronal program (Abernathy et al. 2017). The conversion process by miR-9/9*-124 shares similarities to molecular cascades underlying neurogenesis during neural development such as the downregulation of REST, a well-established transcription repressor of neuronal genes (Ballas et al., 2005; Lee et al., 2018; Schoenherr and Anderson, 1995) and switching of homologous chromatin modifiers from non-neuronal to neuronal counterparts including DNMT3B to DNMT3A, subunits of BAF/BRM-associated factor (BAF) complexes, and TOP2A to TOP2B

(Abernathy et al. 2017; Lee et al. 2018; Lessard et al. 2007; Staahl et al. 2013; Watanabe et al. 1994; Yoo et al. 2009; Tsutsui et al. 2001). Although the direct repression by brain-enriched miRNAs on non-neuronal targets, for instance, *REST* (Packer et al., 2008; Visvanathan et al., 2007), *ACTL6A* (Yoo et al., 2009), and *PTBP1* (Makeyev et al., 2007) for the induction of neuronal counterparts offer a classic representation of miRNAs acting as negative regulators of downstream target genes, how these miRNAs function in the midst of neuronal milieu remains unknown.

The robustness of miRNA-based neuronal reprogramming allows for the investigation of the pathways downstream of miR-9/9*-124 that promote neuronal identity (Abernathy et al. 2017). In my thesis work, we employed high-throughput sequencing of RNA isolated by crosslinking immunoprecipitation (HITS-CLIP) of Argonaute (AGO) during miR-9/9*-124-mediated neuronal reprogramming of human fibroblasts to map miR-9/9*-124-target interactions at the onset of neuronal fate acquisition. Unexpectedly, we identified a suite of neuronal genes enriched with AGO binding, in particular, corresponding to the binding sites of miR-124. The upregulation of these neuronal genes required miR-124, suggesting that miR-124 not only function as a repressor, but also as an effector to promote neuronal gene expression. Although the ability of miRNAs as a positive effector of downstream target genes has been implicated before (Truesdell et al., 2012; Vasudevan et al., 2007; Vasudevan and Steitz, 2007), little is known about the molecular mechanism that governs a miRNA's activity as an activator in neurons.

Among the genes identified to be targeted and upregulated by miR-124 was *PTBP2*, a neuron-enriched RNA-binding protein (RBP). We elected to further focus on *PTBP2* to understand the mechanism underlying miR-124 as an activator because the miR-124-PTBP2 axis

presented intriguing questions. A non-neuronal homolog *PTBP1* (Boutz et al., 2007) and *PTBP2* both contain miR-124 target sites at their 3'UTRs (Makeyev et al., 2007; Y. Xue et al., 2016). Why is there selective repression on *PTBP1* while *PTBP2* escapes the repression by miR-124 in neurons? The current view on the initial activation of *PTBP2* points to the activity of PTBP1 as a repressor of *PTBP2* that is relieved upon miR-124 expression at the onset of neuronal differentiation (Makeyev et al., 2007). However, the mechanism by which *PTBP2* expression persists while being targeted by miR-124 remains unknown. In this study, we describe a series of experiments to provide evidence for an RNA-binding protein, ELAVL3, induced in neurons, directly acting on *PTBP2* 3'UTR to mediate the mode of miR-124 as an activator. This synergism between miR-124 and ELAVL3 drives the neuronal program in human neurons and thus the successful conversion of human fibroblasts.

The miR-124-mediated induction of PTBP2 is essential for neuronal reprogramming as knockdown of PTBP2 results in dysregulated spliced isoforms of neuronal transcripts, including *DPF1*. DPF1 is a subunit of the neuron-specific chromatin remodeling BAF complex. Like the switching of PTB proteins, non-neuronal PHF10 switches for neuronal DPF1 and/or DPF3 subunit in neurons (Lessard et al. 2007). We uncovered that PTBP2 mediates the alternative splicing of *DPF1* in neurons to generate an isoform with shortened PHD. This splicing event is likely required to enhance the binding of DPF1 to histone modifications in neurons. In my thesis, we propose a model in which the bifunctional activity of miR-124 is determined by the concurrent availability of RBPs for the proper splicing of *DPF1* and reconfiguration of the BAF complex assembly in human neurons.

Chapter 2: Current understanding of miR-9/9*-124-based neuronal reprogramming of human fibroblasts

From:

Mechanistic insights into microRNA-induced neuronal reprogramming of human adult fibroblasts.

Ya-Lin Lu & Andrew S. Yoo

Front. Neurosci. 02 August 2018

Abstract

The use of transcriptional factors as cell fate regulators are often the primary focus in the direct reprogramming of somatic cells into neurons. However, in human adult fibroblasts, deriving functionally mature neurons with high efficiency requires additional neurogenic factors such as microRNAs (miRNAs) to evoke a neuronal state permissive to transcription factors to exert their reprogramming activities. As such, increasing evidence suggests brain-enriched miRNAs, miR-9/9* and miR-124, as potent neurogenic molecules through simultaneously targeting of anti-neurogenic effectors while allowing additional transcription factors to generate specific subtypes of human neurons. In this review, we will focus on methods that utilize neuronal miRNAs and provide mechanistic insights by which neuronal miRNAs, in synergism with brain-region specific transcription factors, drive the conversion of human fibroblasts into clinically relevant subtypes of neurons. Furthermore, we will provide insights into the age signature of directly converted neurons and how the converted human neurons can be utilized to model late-onset neurodegenerative disorders.

MiRNAs as potent cell fate regulators

Traditionally, transcription factors, in particular, pioneer transcription factors, have been viewed as regulators and determinants of cell fate. With domains that can interact directly with chromatin and/or other modifier proteins, transcription factors have been widely used for cellular reprogramming (Iwafuchi-Doi and Zaret, 2016, 2014), including the generation of induced pluripotent stem cells (iPSC) from somatic cells (Takahashi and Yamanaka, 2006). Increasing studies across different cellular contexts have revealed that miRNAs are also potent cell fate regulators as miRNAs not only target large repertoire of genes in genetic networks but also

epigenetic regulators necessary for the remodeling of the chromatin (Gruber and Zavolan, 2013; Ivey and Srivastava, 2010; Rajman and Schratt, 2017; Yoo et al., 2009). Subsequently, miRNAs have been used to generate iPSCs (Anokye-Danso et al., 2011), cardiomyocytes (Jayawardena et al., 2012), and neurons (Yoo et al., 2011) from fibroblasts.

MiR-9/9* and miR-124 are neurogenic molecules

The acquisition of neuronal fate requires the downregulation of the neuron-restrictive silencer factor (NRSF) or repressor element-1 silencing transcription factor (REST) that represses neuronal genes in non-neuronal cells, including the neuron-specific miRNAs, miR-9/9* and miR-124 (miR-9/9*-124) (Conaco et al., 2006; Deo et al., 2006; Lagos-Quintana et al., 2002; Lim et al., 2005). Both miR-9/9* and miR-124 are highly abundant in neuronal tissues (He et al., 2012; Lagos-Quintana et al., 2002; Lim et al., 2005), and are essential for neuronal differentiation (Cheng et al., 2009; Dajas-Bailador et al., 2012; Q. Xue et al., 2016) and the maintenance of neuronal identity through the repression of anti-neural genes including cofactors of the REST complex, RCOR1 and SCP1 (Packer et al., 2008; Visvanathan et al., 2007). As overexpression of miR-9/9* (Leucht et al., 2008; Zhao et al., 2009) and/or miR-124 (Akerblom et al., 2012; Cheng et al., 2009; Krichevsky et al., 2006) in stem cells or neural progenitors resulted in the precocious acquisition of neuronal fate, demonstrating the function of miRNAs in the activation of neuronal program (Lim et al., 2005). Subsequently, knockdown of REST can directly convert adult somatic cells into neurons in part due to the induction of neuron-specific miRNAs, miR-9/9* and miR-124 (Drouin-Ouellet et al., 2017). Therefore ectopic expression of miR-9/9*-124 was also shown to drive the direct conversion of primary human dermal fibroblasts into functional neurons (Yoo et al., 2011). Interestingly, miR-124 alone has been used

to in neuronal reprogramming with the help of transcriptional factors (Ambasudhan et al., 2011; Jiang et al., 2015). Here, we review current understanding of the properties of miR-9/9* and miR-124 in both developmental and cellular reprogramming contexts highlighting their synergistic roles in coordinating the molecular switching of several critical non-neuronal to neuronal components during mammalian neurogenesis. We will mainly focus on the molecular switches critical in epigenetic regulation such as chromatin remodeling and DNA methylation, and transcriptome dynamics such as alternative splicing underlying the adoption of the neuronal identity. Our discussion will also include molecular pathways that occur during *in vivo* neurogenesis and are also recapitulated in the miRNA-directed reprogramming of human fibroblasts into neurons for the successful overcoming of cell fate barriers.

MiRNAs orchestrate the composition of BAF chromatin remodeling complexes

Spatial and temporal reciprocity of homologous gene or isoform expression during neurogenesis is a recurring theme. Previous studies have indicated that the neurogenic and reprogramming activity of miR-9/9* and miR-124 may be in part through the direct targeting of subunits of the ATP-dependent BRG/BRM associated factor (BAF) chromatin remodeling complexes (Staahl et al., 2013; Staahl and Crabtree, 2013; Yoo et al., 2009). Mammalian BAF complexes are large multi-subunit complexes combinatorically assembled in a cell type-dependent manner. The combinatorial assembly of different homologs and splice variants of BAF subunit families confers functional specificity as each subunit contains functional domains that recognized DNA and/or modified histones (Wu et al., 2009; Zheng et al., 2012). For example, embryonic stem cell (ESC) BAF (esBAF) is characterized by BAF53a and a

homodimer of BAF155, as opposed to a heterodimer of BAF155 and BAF170 in differentiated cells (Ho et al., 2009b; Weidong Wang et al., 1996; W Wang et al., 1996). The esBAF complex is involved in maintaining pluripotency by establishing an ESC-specific chromatin state permissive for transcription factors and signaling molecules to access ESC-associated genes (Ho et al., 2009a; Kidder et al., 2009). Although BAF complexes are traditionally known to antagonize the function of polycomb repressive complexes (PRC) to promote chromatin accessibility for gene activation (Ho et al., 2011; Kennison, 1995), studies have also suggested that BAF complexes can synergize with PRC for gene regulation (Ho et al., 2011).

The BAF complex is crucial for mammalian nervous system as mutations to BAF subunits have been implicated in neurological disorders such as Coffin-Sirius syndrome due to mutation in BRG1 (Ronan et al., 2013; Tsurusaki et al., 2012) and SS18L1/CREST in amyotrophic lateral sclerosis (Chesi et al., 2013). During neural development, several BAF complex subunit switches to form the neuron-specific BAF (nBAF) complex (Staahl and Crabtree, 2013). The assembly of the nBAF complex requires the switching of progenitor subunits (BAF53a, BAF45a and SS18) to neuronal subunits (BAF53b, BAF45b or BAF45c and SS18L1/CREST) between the proliferating ventricular zone and the post-mitotic zone (Lessard et al., 2007; Olave, 2002; Staahl et al., 2013; Wu et al., 2007; Yoo et al., 2009). These molecular switches also occur during miRNA-mediated direct conversion of human fibroblasts into neurons (Staahl et al., 2013), in which the reciprocal switching of BAF53a to BAF53b is directly orchestrated by miR-9/9* and miR-124 (Staahl et al., 2013; Yoo et al., 2009) (Figure 1). The assembly of the nBAF complex is essential for proper neuronal function in learning and memory as loss of function of either BAF53b or SS18L1/CREST dramatically reduced dendritic outgrowth and morphology (Aizawa et al., 2004; Staahl et al., 2013; Vogel-Ciernia et al., 2013; Wu et al., 2007). The function of

chromatin remodeling by BAF complex was also found to be critical for neuronal reprogramming as loss of BRG1 during miRNA-mediated reprogramming abolished the chromatin landscape permissive to the activation of the neuronal program (Abernathy et al., 2017a).

Switching of chromatin modifiers are crucial for cell fate conversion

The switching of other homologous epigenetic regulators also occur during neurogenesis and neuronal reprogramming, though may not be direct targets of miR-9/9*-124. These include the switching of DNA topoisomerase II (TOP2) that functions to decatenate and catenate chromatin, from non-neuronal TOP2A to neuronal TOP2B (Thakurela et al., 2013; Tiwari et al., 2012; Tsutsui et al., 2001a; Watanabe et al., 1994). TOP2A is expressed in mitotic cells and interacts with BAF complexes to modulate chromatin accessibility (Dykhuizen et al., 2013; Miller et al., 2017; Ken Tsutsui et al., 2001; Wijdeven et al., 2015). On the other hand, TOP2B is required for neuronal differentiation *in vitro* and *in vivo* (Tiwari et al., 2012; Ken Tsutsui et al., 2001; Yang, 2000). Consistent with neuronal differentiation, miR-9/9*-124 instruct the similar switch of TOP2 homologs during neuronal reprogramming of human adult fibroblasts by inducing a rapid reduction of TOP2A in fibroblasts for the selective expression TOP2B in converted neurons (Abernathy et al., 2017a) (Figure 1).

Similarly, the reconfiguration of the epigenetic landscape during neuronal reprogramming also involves changes in DNA methylation patterns (Abernathy et al., 2017a). Regarding the reprogramming activities of the miRNAs, it has been shown that ectopic expression of miR-9/9*-

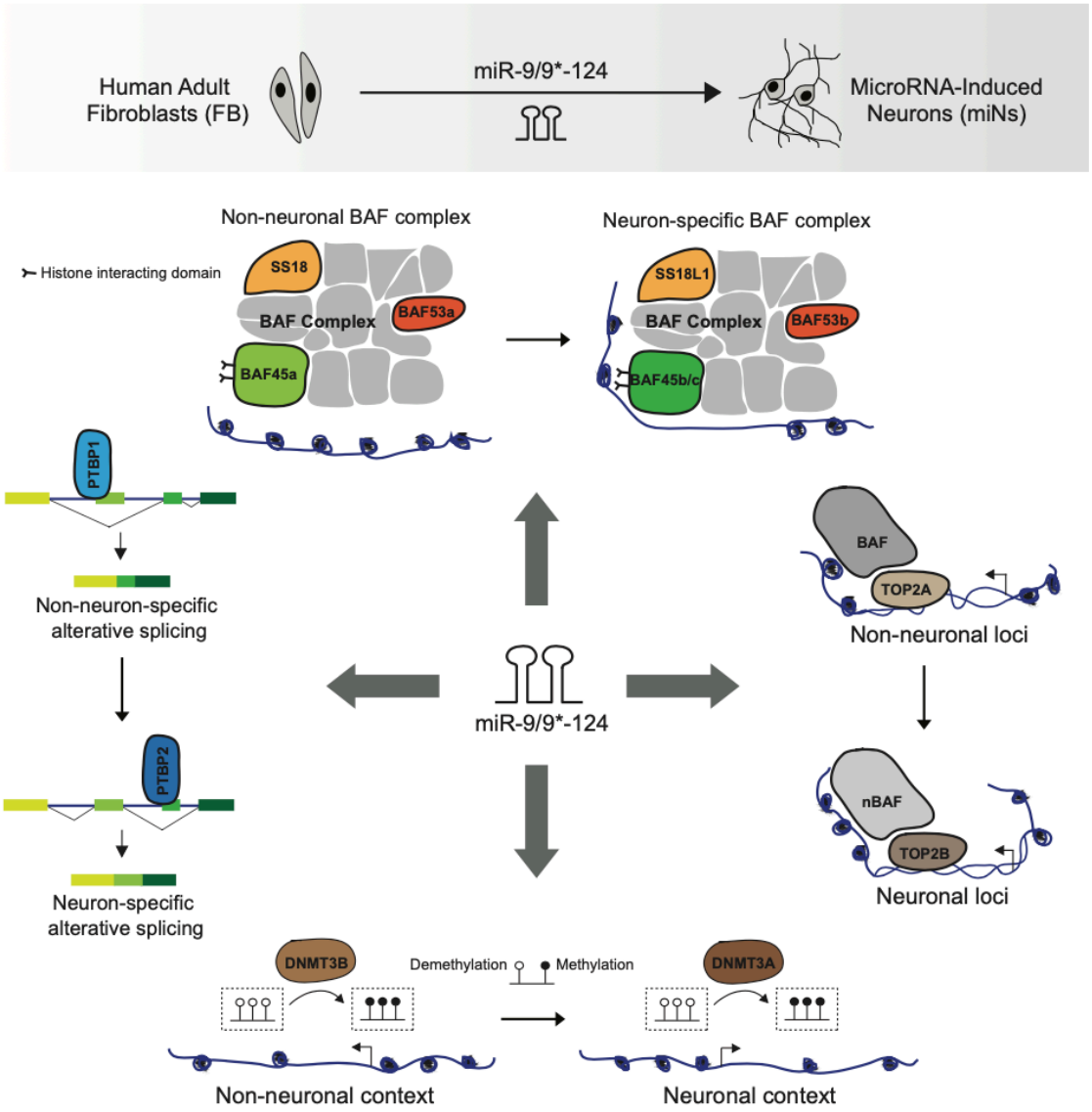

Figure 1. MiR-9/9*-124-mediated neuronal reprogramming of human adult fibroblasts. Ectopic expression of miR-9/9*-124 in human adult fibroblasts leads to the switching of several non-neuronal to neuronal components for neural fate acquisition. MiRNAs orchestrate the genetic switching of epigenetic regulators including the BAF complex subunits (BAF53a, BAF45a and SS18 to BAF53b, BAF45b/c and SS18L1), TOP2A to TOP2B, and DNMT3B to DNMT3A. These coordinated molecular switches underlie the establishment of a neuronal epigenetic landscape during neuronal reprogramming. Additionally, the switching of PTB proteins, from PTBP1 to PTBP2, mediated by miR-124 activates neuron-specific alternative splicing program.

124 in fibroblasts recapitulated the molecular switching of de novo methyltransferases, DNMT3B to DNMT3A, similarly to neural differentiation *in vivo* (Abernathy et al., 2017a; Feng et al., 2005; Watanabe et al., 2006) (Figure 1). DNMT3A has been implicated in various aspects of neuronal development, including synaptic plasticity (Colquitt et al., 2014; Feng et al., 2010), but it remains unclear how DNMT3A modulates gene expression in the nervous system. Although DNA methylation is viewed as a repressive mark, methylation marks deposited by DNMT3A have also been associated with enhanced gene expression through antagonizing PRC2 activity (Wu et al., 2010). The dramatic change in DNA methylation profile in miRNA-induced neurons also involves the induction of a family of demethylase, ten-eleven translocation (TET) family proteins (TET1/2/3) (Abernathy et al., 2017a), implicated in neuronal development (Hahn et al., 2013; Zhang et al., 2013). It should be noted, however, what additional molecules interact with DNMT3A and TET proteins during neuronal reprogramming to influence DNA methylation at specific loci remains largely unknown.

Although the mechanisms underlying the switching of epigenetic effectors remain to be precisely defined, it is clear that miR-9/9*-124 promote neuronal identity during the direct reprogramming of human fibroblasts through establishing an epigenetic state permissive for the downstream acquisition of neuronal fate. The reciprocal temporal and spatial switching of chromatin modifiers observed both during neurogenesis and neuronal reprogramming highlight the complex and dynamic epigenetic regulations required to overcome cell fate barriers.

MiR-124-mediated PTB switching regulates neuronal splicing profile

In addition to epigenetic regulators, post-transcriptional regulation of gene expression appears to be integral for neuronal reprogramming. The expression of PTB (polypyrimidine tract-binding) proteins, PTBP1 and PTBP2, are mutually exclusive and exhibit reciprocal switching during neural fate acquisition (Boutz et al., 2007). PTB proteins are RNA-binding proteins that bind to U-rich tracts primarily in introns for the post-transcriptional regulation of mRNAs, including alternative splicing (Keppetipola et al., 2012; Wagner and Garcia-Blanco, 2001). PTBP1 is expressed in non-neuronal cells and neural progenitors whereas the expression of its neuronal homolog, PTBP2 (nPTB), a splicing target of PTBP1, is primarily restricted to post-mitotic neurons in the nervous system (Boutz et al., 2007; Makeyev et al., 2007). PTBP1 represses PTBP2 expression by introducing a premature stop through the skipping of PTBP2 exon (Boutz et al., 2007). During development, the expression of miR-124 at the onset of neurogenesis mediates the switching of PTB proteins by targeting the 3'UTR of PTBP1, thereby alleviating PTBP1-mediated repression of PTBP2 in neurons (Makeyev et al., 2007). Although PTB proteins exhibit functional redundancy (Spellman et al., 2007), PTBP2 in neurons are essential for the proper splicing of various transcripts involved in neuronal function (Boutz et al., 2007; Li et al., 2014; Licatalosi et al., 2012; Zheng et al., 2012). Interestingly, ablating PTBP1 function in several cell types, including mouse embryonic fibroblasts, though insufficient in human fibroblasts, led to the direct conversion into neurons (Xue et al., 2013; Y. Xue et al., 2016), suggesting the significance of PTBP2 for the induction of neuronal fate. In addition to the activation of PTBP2 upon neural fate acquisition, PTBP2 level attenuates later in development for neuronal maturation (Li et al., 2014; Y. Xue et al., 2016). The attenuation of PTBP2 can be recapitulated with sequential knockdown of both PTB proteins resulting in the reprogramming of human adult fibroblasts into neurons (Y. Xue et al., 2016). The proposed mechanism is that

PTBP2 reduction initiates a regulatory loop that activates downstream BRN2 for miR-9 expression, which dampens PTBP2 activity through 3'UTR targeting (Y. Xue et al., 2016). Together, PTBP2 level is dynamically regulated throughout neuronal differentiation and is essential as PTBP2 knockout results in neuronal death (Li et al., 2014; Y. Xue et al., 2016).

The use of miRNA-induced neuronal ground state for subtype-specific neuronal reprogramming

As neurological disorders affect distinct neuronal subtypes, the generation of neuronal subtypes has been of interest not only for dissecting the underlying mechanisms behind subtype-specific neuronal conversion, but also for the implication of the reprogrammed neurons in disease modeling. MiR-9/9*-124 have been shown to induce a "default" neuronal state characterized by enhanced accessibility of chromatin regions encompassing neuronal genes (Figure 2). These regions include genes specifically expressed in distinct neuronal subtypes, yet remain inactivated, thereby providing the chromatin environment that is open and permissive for subtype-defining inputs of transcription factors (Abernathy et al., 2017a). Furthermore, unlike iPSC-based reprogramming methods, direct neuronal conversion bypasses an embryonic intermediate (Lapasset et al., 2011; Miller et al., 2013), thereby retaining the age signatures of starting fibroblasts including the epigenetic clock (Horvath, 2013), age-associated changes in transcriptome and microRNAs, reactive oxygen species (ROS) levels, DNA damage and telomere lengths (Huh et al., 2016; Mertens et al., 2015; Tang et al., 2017). As direct neuronal conversion can faithfully recapitulate age-associated phenotypes, directly reprogrammed neurons hold promise in the modeling of adult-onset neurodegenerative diseases and necessitates the control of subtype-specificity during neuronal reprogramming.

The use of synergism between miRNAs and subtype-defining transcription factors to obtain subtype-specific neurons has been successful in generating cortical neurons (Yoo et al., 2011), striatal medium spiny neurons (Victor et al., 2014), and spinal cord motor neurons (Abernathy et al., 2017a) (Figure 2). For instance, heterogeneous population of excitatory and inhibitory neurons belonging to the cortex can be obtained with the use of miR-9/9*-124 in combination with NEUROD2, ASCL1, and MYT1L (DAM) cocktail from adult fibroblasts (Yoo et al., 2011). However, it remains to be tested whether layer-enriched transcription factors would be able to further guide the cortical lineage to neurons with layer-specific identities. Since previous studies demonstrated the plasticity of cortical neurons being able to transition between cortical layer fates (De la Rossa et al., 2013; Rouaux and Arlotta, 2013, 2010), it raises the potential that a similar approach may be taken in a cellular reprogramming context.

An enriched population of striatal medium spiny neurons (MSN), the neuronal subtype primarily degenerated in Huntington's disease (HD), can be derived using miR-9/9*-124 in conjunction with CTIP2, DLX1/2, and MYT1L (CDM) factors (Victor et al., 2014). More than 70% of cells express DARPP32, a marker of MSNs, and when injected into the stratum of mouse pups, the converted MSNs incorporate and project to the substantia nigra and globus pallidus *in vivo* with electrophysiological properties similar to neighboring endogenous mouse MSNs (Victor et al., 2014). Interestingly, applying the MSN-specific neuronal conversion approach in fibroblast samples from symptomatic patients has proven to be successful in generating patient-specific MSNs manifesting hallmark HD pathology, including HTT aggregation, spontaneous neuronal death, and increased DNA damage (Victor et al., 2018). Importantly, the manifestation of HD-associated phenotypes was dependent on the specificity of the type of neurons generated

and the age status in converted neurons, further highlighting the importance of age and subtype-specificity in modeling adult-onset diseases (Victor et al., 2018).

Spinal cord motor neurons are most susceptible to degeneration in amyotrophic lateral sclerosis (ALS) and spinal muscular atrophy (SMA) diseases, and devising a conversion protocol could be instrumental to the study and modeling of motor neuron (MN) diseases. Using a combination of NEUROG1, SOX11, ISL1, and LHX3 (NSIL), MNs can be generated from fibroblasts of ALS patients in which the patient-derived MNs manifest various ALS pathologies, including FUS protein mislocalization and neuronal degeneration (Liu et al., 2016). Alternatively, miRNAs in conjunction with two transcription factors, ISL1 and LHX3, have been shown to generate functional mature MNs that display transcriptional signatures similar to *in vivo* mouse spinal MNs (Abernathy et al., 2017a). Despite the robustness in generating a highly enriched population of spinal cord MNs, it remains to be demonstrated whether the MNs derived through the miRNA-induced neuronal state can be used to model ALS or SMA.

The use of transcription factors only, ASCL1, NURR1, and LMX1A, to directly convert fibroblasts of healthy and Parkinson's disease (PD) patients into dopaminergic cells is possible but with limited efficiency in human cells (Caiazzo et al., 2011). Interestingly, reprogramming efficiency improved with the addition of neuronal miRNA, miR-124, and shRNA against p53, to the transcription factor cocktail using adult fibroblasts (Jiang et al., 2015). One of the proposed mechanisms behind this enhancement is due to the activation of TET proteins, in particular TET1, during reprogramming, as knockdown of TET1 results in increased cell death while overexpression enhances the overall number of TUBB3 and TH positive cells (Jiang et al., 2015). The induction of TET family members has also been observed in miR-9/9*-124-mediated reprogramming (Abernathy et al., 2017a).

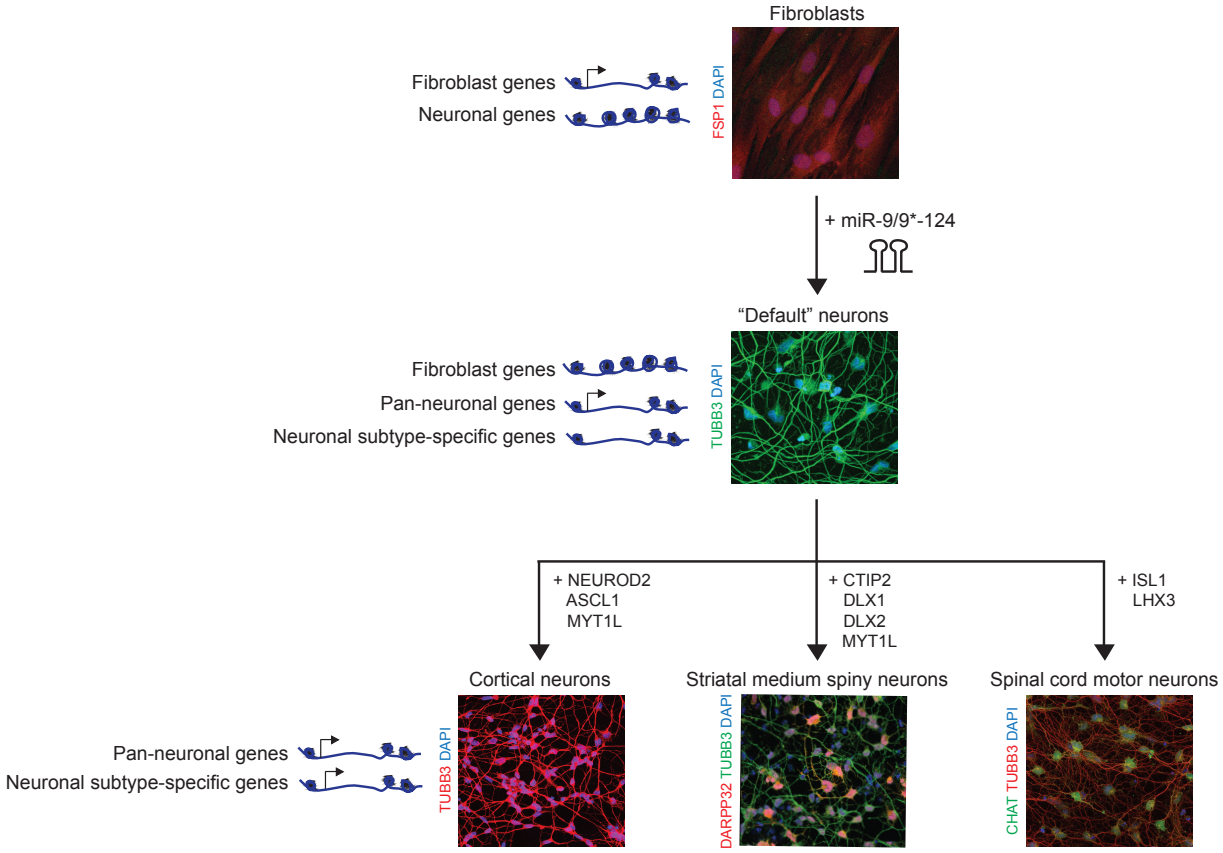

Figure 2. Synergism between microRNAs and transcription factors for subtype-specific neuronal reprogramming of human adult fibroblasts. MiR-9/9*-124 mediate the erasure of fibroblast fate through remodeling of a fibroblast-specific chromatin landscape and transcriptome profile and promote a neuronal chromatin landscape and transcriptome. MiRNA alone generates a default neuronal state characterized by the reconfiguration of the chromatin state permissive to the subtype-defining inputs of transcription factors. With distinct combinations of transcription factors, the miRNA-based conversion have been successfully employed to generate cortical neurons (Yoo et al., 2011), striatal medium spiny neurons (Victor et al., 2014) and spinal cord motor neurons (Abernathy et al., 2017).

The generation of additional neuronal subtypes, including serotonergic neurons for the study of neuropsychiatric disorders such as schizophrenia (Vadodaria et al., 2016; Xu et al., 2016) and sensory neurons for the study of pain sensation (Blanchard et al., 2015; Wainger et al., 2015) have been demonstrated using the transcription factor approach. It remains to be tested whether miR-9/9*-124 could be combined with similar transcription factors to enhance overall conversion efficiency in human cells.

Summary

MiR-9/9*-124-mediated direct conversion of human adult fibroblasts into functional neurons reconfigures and establishes a pan-neuronal epigenetic landscape permissive on which brain region-enriched transcription factors can act and generate specific neuronal subtype. MiR-9/9*-124 are potent neurogenic molecules as they mediate numerous genetic switches that occur during neurogenesis, in which many include epigenetic players and pro-neurogenic effectors that are important to overcome cell fate barriers and activate neuronal fate programs. As miRNAs regulate expression of multiple genes, the pro-neural environment established by the miRNAs allow for the use of this paradigm for the study of neural fate acquisition. To better understand and address the role of brain-enriched miRNAs, examining miRNA-mRNA network would provide invaluable insights to the acquisition of neuronal fate. Though much remains to be uncovered, with the maintenance of age of starting fibroblasts preserved after cellular conversion, modeling age-dependent neurodegenerative diseases through direct reprogramming allows for the faithful recapitulation of age-associated pathogenesis for mechanistic studies of the disease.

Chapter 3: Synergism between microRNA-124 and ELAVL3 drives neuronal gene upregulation in human neurons

In part from:

MiR-124 synergism with ELAVL3 enhances target gene expression to promote neuronal maturity.

Ya-Lin Lu, Yangjian Liu, Matthew J. McCoy & Andrew S. Yoo

In submission

Abstract

Neuron-enriched microRNAs (miRNAs), miR-9/9* and miR-124 (miR-9/9*-124), direct cell fate switching of human fibroblasts to neurons when ectopically expressed by repressing anti-neurogenic genes. How these miRNAs function after the onset of the transcriptome switch to a neuronal fate remains unclear. Here, we identified direct targets of miRNAs by Argonaute (AGO) HITS-CLIP as reprogramming cells activate the neuronal program and reveal the role of miR-124 that directly promotes the expression of its target genes associated with neuronal development and function. The mode of miR-124 as a positive regulator is determined by a neuron-enriched RNA-binding protein, ELAVL3, that interacts with AGO and binds target transcripts, whereas the non-neuronal ELAVL1 counterpart fails to elevate the miRNA-target gene expression. Although existing literature indicate that miRNA-ELAVL1 interaction can result in either target gene upregulation or downregulation in a context-dependent manner, we specifically identified neuronal ELAVL3 as the driver for miRNA target gene upregulation in neurons. In primary human neurons, repressing miR-124 and ELAVL3 led to the downregulation of genes involved in neuronal function and process outgrowth, and cellular phenotypes of reduced inward currents and neurite outgrowth. Results from our study support the role of miR-124 promoting neuronal function through positive regulation of its target genes.

AGO binds both downregulated and upregulated genes during miR-9/9*-124-mediated direct neuronal reprogramming of human fibroblasts

Previous studies showed that the ectopic expression of miR-9/9*-124 in human adult fibroblasts (HAFs) induces a neuronal state characterized by the appearance of neuronal markers

(such as MAP2, TUBB3, NCAM, and SNAP25) (Figure 1A) and electrical excitability (Abernathy et al. 2017). To identify target genes of miR-9/9*-124 as reprogramming cells transition to neuronal identity, we carried out AGO HITS-CLIP after two weeks into reprogramming, a time point when neuronal genes are activated (Abernathy et al. 2017), to identify transcripts bound with AGO loaded with miR-9/9* or miR-124 over the non-specific miRNA (miR-NS) control ($Log_2FC \geq 1$; adj.P-value < 0.05). We compared these hits to the list of differentially expressed genes (DEGs) (by RNA-seq analysis; $-1 \leq Log_2FC \geq 1$; adj.P-value < 0.05) at day 20 of miRNA-induced neurons (miNs) (Abernathy et al. 2017). As expected, we found target transcripts that were downregulated consistent with the repressive mode of miRNAs (Figure 1B, 113 genes labeled as green dots) including some known targets, *SHROOM3* and *PHF19* (Lu et al., 2018; Neo et al., 2014; Zhou et al., 2014). Interestingly, we also discovered 453 unique gene transcripts with enriched AGO binding, which were upregulated in day 20 miNs (Figure 1B, red dots). By gene ontology (GO) analysis, these upregulated genes with enriched AGO loading in response to miR-9/9*-124 were associated with various neuronal processes such as synaptic transmission and regulation of membrane potential (red), in contrast to non-neuronal, downregulated target genes (green) (Figure 1C). Moreover, when examined against the time-course transcriptome analysis during neuronal reprogramming (Abernathy et al. 2017), the expression of the identified neuronal target genes showed continuous upregulation during later time point of neuronal conversion (Figure 1D). For example, neuronal transcripts such as *MAP2*, *PTBP2*, and *SLC4A8* that were highly expressed in day 20 miNs harbored AGO binding sites at the 3'UTR (Figure 1E). To determine the fraction of upregulated neuronal genes that are likely actual targets of miR-9/9* and/or miR-124, we extracted the AGO-enriched sequences and

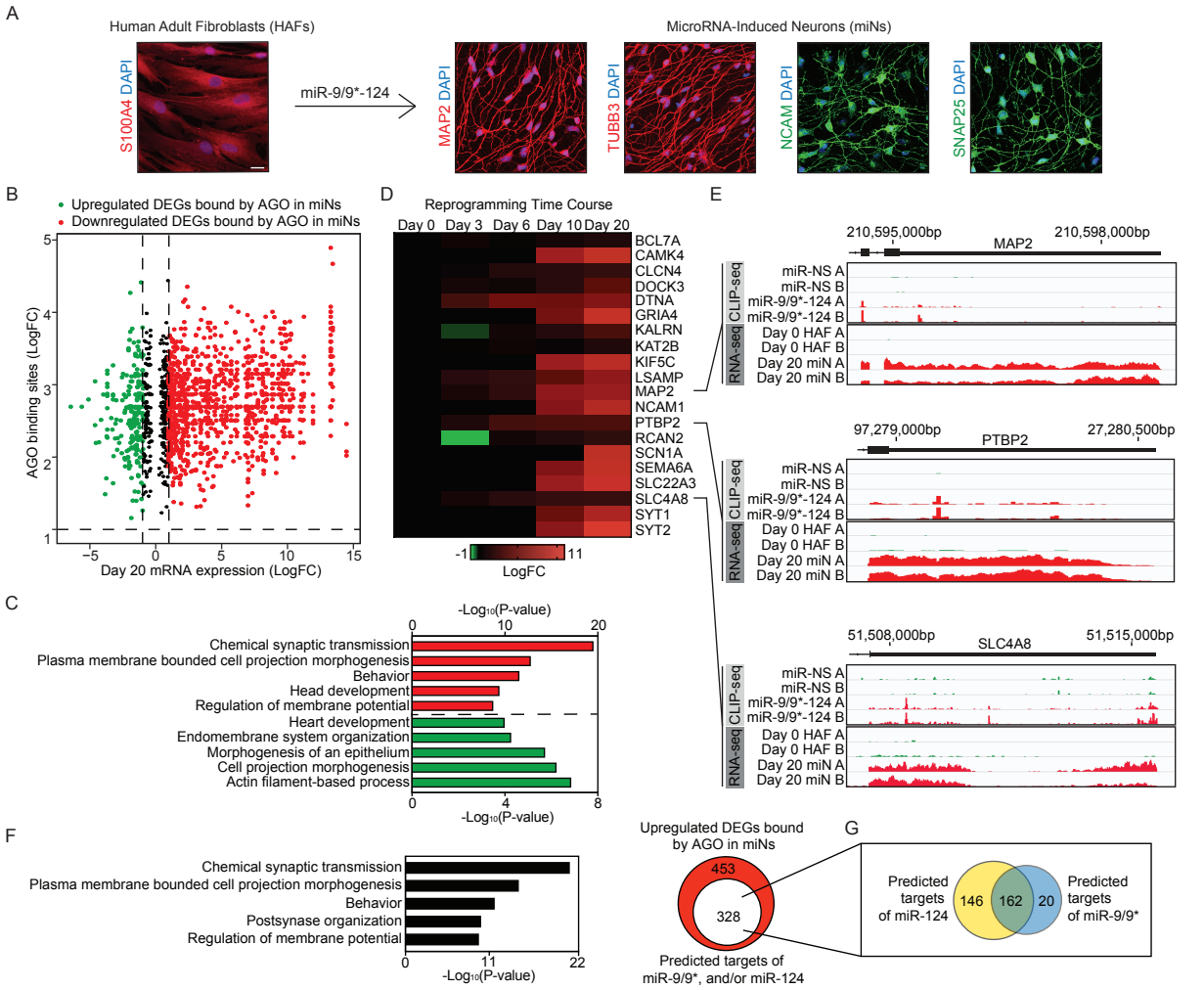

Figure 1. Enrichment of AGO binding on transcripts of neuronal genes upregulated during miR-9/9*-124-mediated neuronal conversion
(A) Examples of miR-9/9*-124-mediated direct reprogramming of human adult dermal fibroblasts (HAFs) into neurons (miNs). Photographs show immunostaining of the fibroblast marker (S100A4) and neuronal markers (MAP2, TUBB3, NCAM, and SNAP25). Scale bar = 20 μm.
(B) A volcano plot of differentially expressed genes at day 20 miNs and enrichment of AGO binding in response to miR-9/9*-124 expression identified by AGO HITS-CLIP analysis. Red dots, day 20 mRNA expression Log2FC ≥ 1; adj.P-value < 0.05, AGO binding Log2FC ≥ 1, adj.P-value < 0.05. Green dots, day 20 mRNA expression Log2FC ≤ -1; adj.P-value < 0.05, AGO binding Log2FC ≥ 1, adj.P-value < 0.05.
(C) Top biological GO terms of upregulated (red) and downregulated (green) DEGs in day 20 miNs differentially bound by AGO.
(D) Time course heatmap of select upregulated DEGs enriched for AGO binding with miR-9/9*-124 expression.
(E) Track views of AGO CLIP-seq tracks (top) and RNA-seq tracks (bottom) for gene examples showing the enrichment of AGO binding miR-9/9*-124 expression (over control miR-NS) and increased transcript levels at 3'UTRs.
(F) Of the 301 unique upregulated DEGs identified in (A), 207 are predicted to harbor miR-9/9* and/or miR-124 sites at the AGO-enriched regions through RNAhybrid prediction. The graph indicates top biological GO terms associated with the 328 upregulated DEGs containing miR-9/9* and/or miR-124 target sites.
(G) Breakdown of the 328 upregulated DEGs in (F) based on common or specific targets of miR-9/9* and/or miR-124.

predicted the duplex formation by either miR-9/9* and/or miR-124 through RNAhybrid (a maximum free energy threshold of -20 kcal/mol) (Rehmsmeier, 2004). Of the 453 upregulated DEGs in miNs bound by AGO (Figure 1B), 328 (~72%) gene transcripts are predicted to contain miR-9/9* and/or miR-124 binding sites (Figure 1F). These transcripts harboring miR-9/9*-124 sites are also associated with the similar set of neuronal GO terms in Figure 1C as they include a selection of genes important for neuronal function (Figures 1F). Of these upregulated miR-9/9*-124 target genes, more than 94% of the total genes (308 of 328 genes) contain miR-124 target sequence alone (45%) or with miR-9/9* sites, while less than 6% of the genes (20 genes) contain miR-9/9* target sites only (Figure 1G). These results collectively demonstrate that the AGO-loaded transcripts differentially (up or down) respond to miR-9/9*-124 during neuronal conversion.

MiR-124 target genes are upregulated during neuronal conversion

As a large fraction of the upregulated genes contained miR-124 target sequences (Figure 1G), we further tested if the upregulated genes were *bona fide* targets of miR-124 by knocking down miR-124 expression through the use of a tough decoy (TuD) to inhibit miRNA activity (Bak et al., 2013; Haraguchi et al., 2009). The effect of the lentivirus-based TuD for miR-124 (TuD-miR-124) was monitored after transduction by following the concurrent expression of TurboRFP reporter built in the lentiviral vector and measuring the mature miR-124 level. TuD-miR-124 yielded more than 60% reduction of miR-124 expression in comparison to the control, non-specific miRNA tough decoy (TuD-miR-NS) (Figure S1A-S1B). We then performed RNA-seq analysis on day 20 miNs treated with either TuD-miR-NS or TuD-miR-124 to see whether any of the miR-124 target would fail to be upregulated with TuD-miR-124 treatment (Figure 2A, S1C). When compared with upregulated DEGs in day 20 miNs that were also enriched for AGO

binding (Figure 1), we identified 192 genes ($Log_2FC \leq 0.5$; adj.P-value < 0.01) that failed to be upregulated upon miR-124 reduction (Figure 2A, Table S1). With GO analysis, these identified genes were associated with neuronal terms involved in various synaptic processes (Figure 2B).

To further analyze miR-124-target interactions, we looked into the potential duplex formations between miR-124 and the identified AGO HITS-CLIP peak regions using RNAhybrid (a maximum free energy threshold of -20 kcal/mol) (Rehmsmeier, 2004). Of the upregulated transcripts that harbor AGO-enriched peaks, we identified a spectrum of miR-124 and target mRNA duplex configurations ranging from the canonical 2-8 seed base pairing to non-canonical base pairing starting at position 3 and 4 (Figures 2C, S1D, and S2). These examples include *MAP2* 3'UTR, in which miR-124 base pairing is predicted to start at position 3, while miR-124 target sequences on *PTBP2* 3'UTR at the two peaks are predicted to start at position 1 and position 2, respectively (Figure 2C). Interestingly, across the predicted miR-124:target duplex configurations, we observed consistent auxiliary 2-3 base pairing at the 3' end of miR-124 (Figure S1D).

Our results so far indicate that miR-124 can target and promote the expression of select neuronal genes when cells acquire the neuronal fate during neuronal conversion. We wondered if the active mode of miR-124 would be specific to neuronal cell types. We cloned the 3'UTRs of several identified, upregulated targets (*MAP2*, *PTBP2*, *BCL7A*, *KALRN*, *SEMA6A*, *RCAN2*) into a luciferase reporter construct and transfected into a non-neuronal cell type, HEK293T (a human embryonic kidney cell line), with a miR-9/9*-124 expression construct. After 48 hours post-transfection, we found that unlike reprogrammed neurons, miR-9/9*-124 instead, repressed the luciferase signal in HEK293T cells in comparison to the control miR-NS, while the non-target control, *PGK1* 3'UTR was unaffected (Figure 2D). This result suggests that additional

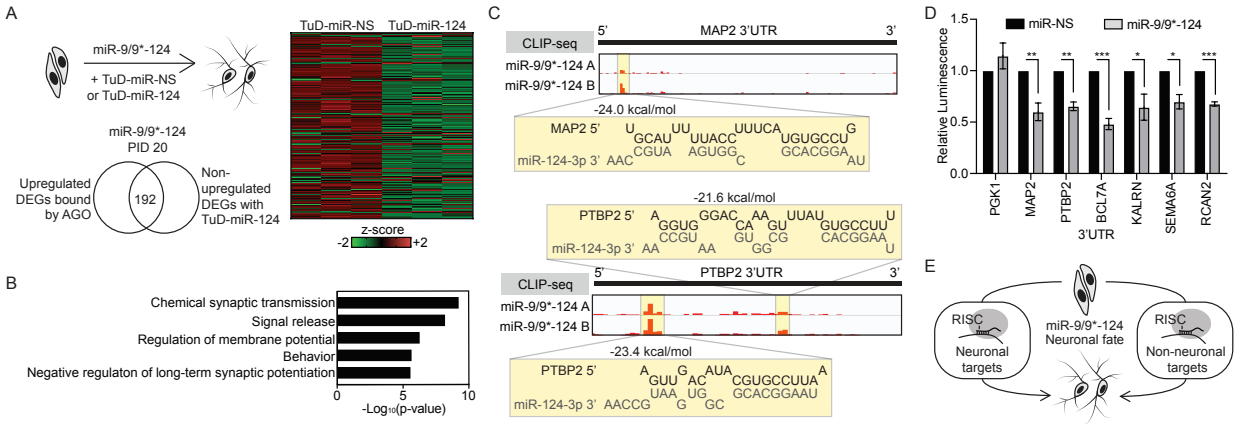

Figure 2. Identification of miR-124 target genes that fail to be upregulated upon the inhibition of miR-124 during miRNA-mediated neuronal conversion
(A) Left, miR-124 activity is reduced through the use of tough decoy (TuD). By overlapping with upregulated DEGs bound by AGO (Figure 1), 192 genes were identified as genes that fail to be increased upon the reduction of miR-124. Right, a heatmap of z-scores of the 192 genes from RNA-seq comparing miNs between TuD-miR-NS and TuD-miR-124 treatments.
(B) Top biological GO terms associated with the 192 genes identified in (A).
(C) Predicted binding of miR-124 to the 3'UTR sequences of neuronal target genes, for example, *MAP2* and *PTBP2*, according to RNAhybrid prediction at the highlighted AGO HITS-CLIP peaks.
(D) Luciferase assays in HEK293T cells of upregulated neuronal target genes of miR-124 selected from A). In the non-neuronal context of HEK293T cells, 3'UTRs from the neuronal genes are targeted and repressed, instead, by miR-9/9*-124. Luminescence measured after 48 hrs of transfection and normalized to miR-NS control of each condition. Data are represented by mean ± SEM from three independent experiments (from left, ** P = 0.0094, P = 0.0011; *** P < 0.001; * P = 0.048, P = 0.012; *** P < 0.001).
(E) A diagram of the observed phenomenon in which miR-9/9*-124 can promote neuronal identity by simultaneously targeting both non-neuronal genes for repression while promoting the expression of neuronal genes during neuronal conversion.

determinants available in neuronal cells may be in play to govern the activity of miR-124 as a positive regulator while simultaneously functioning to repress non-neuronal targets (Figure 2E).

PTBP1 and PTBP2 3'UTR as targets of miR-124

To further dissect the mechanism underlying the dual modes of miR-124 on its targets, we elected to focus on *PTBP2* from the list of our identified neuronal targets because i) *PTBP2* and its non-neuronal homolog, *PTBP1*, both contain miR-124 sites in their 3'UTRs (Figure 3A), and ii) both *PTBP1* and *PTBP2* 3'UTRs are targeted and repressed by miR-124 in HEK293T cells (Figure 3A), and iii) contrastingly, as observed in the human brain, qPCR analysis showed that the neuronal conversion established the mutually exclusive expression between *PTBP1* and *PTBP2* (Figure 3B). Therefore, the PTB homologs represent an ideal example to investigate how two closely related targets respond differently to miR-124.

The 3'UTRs of human *PTBP1* and *PTBP2* contain two predicted target sites for miR-124 (yellow bar) and one site for miR-9 (blue bar) (Figure 3A). Luciferase reporter assays in the non-neuronal HEK293T cells showed that miR-9/9*-124 or miR-124 alone (but not miR-9/9* alone) repressed both *PTBP1* and *PTBP2* through their 3'UTRs indicating that miR-124 is the primary miRNA targeting both PTB 3'UTRs (Figure 3A). Mutating the two miR-124 sites in *PTBP2* 3'UTR (s1 and s2) rendered the 3'UTR insensitive to miR-124 (Figure S3A). While our results pointing to the ability of miR-124 to target and repress 3'UTRs of both *PTBP1* and *PTBP2* in cell lines were consistent with previous findings (Makeyev et al., 2007; Xue et al., 2016), it remains unknown how miRNA-mediated neuronal conversion of HAFs establishes the mutually exclusive expression of PTBP1 and PTBP2 as seen in the human brain (Figure 3B) and in *in vivo* neurons (Boutz et al., 2007).

Because *PTBP1* and *PTBP2* are regulated differentially in miNs, we asked whether the repressive activity of miR-124 on *PTBP2* 3'UTR could be reversed with a prolonged neurogenic input by miR-9/9*-124 in HEK293T cells. We expressed a destabilized EGFP reporter containing *PTBP1* 3'UTR, *PTBP2* 3'UTR, or control 3'UTR (CTL) that lacks a 3'UTR in HEK293T cells with the miR-9/9*-124 expression construct (Figure S3B). Analogous to PTBP2 upregulation during neuronal reprogramming of HAFs, we observed the selective repression of EGFP with *PTBP1* 3'UTR but not *PTBP2* 3'UTR (Figures S3B-C). These results suggest that with the prolonged neurogenic input, *PTBP2* 3'UTR responds to miR-124 differentially from when measured after 48 hours with miRNA expression in HEK293T cells (Figures 2A and 3A).

MiR-124 accentuates PTBP2 expression beyond the induction mediated by the downregulation of PTBP1

Previous studies have shown that during development, PTBP1 destabilizes *PTBP2* transcript in non-neuronal cells by alternative splicing, and at the onset of neurogenesis, miR-124 directly represses *PTBP1* resulting in PTBP2 induction (Boutz et al., 2007; Makeyev et al., 2007). Upon miR-9/9*-124 expression in HAFs, we observed the concomitant downregulation and upregulation of endogenous PTBP1 and PTBP2, respectively (Figure 3B). As expected, the initial PTBP2 upregulation was abrogated when *PTBP1* cDNA was overexpressed (Figure 3C), supporting the role of PTBP1 reduction as the initiation step of PTBP2 expression. We then sought to stratify the contribution of PTBP1 repression alone versus the input of miRNAs to the overall PTBP2 level. When PTBP2 protein levels were compared between PTBP1 knockdown with a short hairpin RNA (shRNA) and miR-9/9*-124 expression, we found that miR-9/9*-124 enhanced the PTBP2 level by approximately a two-fold increase over the PTBP1 knockdown

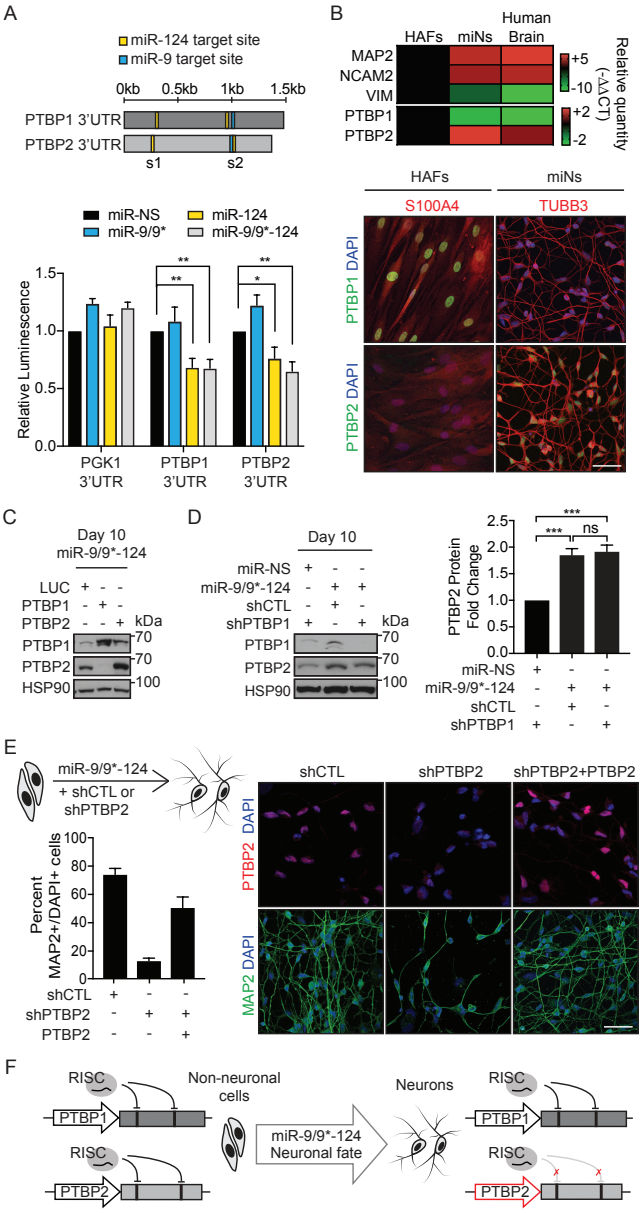

Figure 3. MiR-124 targets both PTBs, but differentially regulate PTB expression during neuronal conversion.
(A) Top, a schematic diagram of PTB 3'UTRs with miR-124 (yellow) and miR-9 (blue) target sites. S1 and s2 refer to the two conserved miR-124 target sites on PTBP2 3'UTR. Bottom, luciferase assays with luminescence measured after 48 hrs of transfection and normalized to miR-NS control in each condition. Data are represented by mean ± SEM from four independent experiments. Two-way ANOVA followed by Dunnett's test (from left, PTBP1 3'UTR ** P = 0.0043, 0.0034; PTBP2 3'UTR * P = 0.0355, ** P = 0.0016)
(B) Top, A heatmap of gene expression assessed by qPCR in starting HAFs, day 30 miRNA-induced neurons (miNs), and human brain RNA. Bottom, PTB switching is recapitulated during the miRNA-mediated direct conversion of HAFs into neurons. HAFs and day 30 miNs immunostained for PTBP1 and PTBP2, along with a fibroblast marker, S100A4, and a pan-neuronal marker, TUBB3. Scale bar = 50 μm.
(C) Initial induction of PTBP2 by the reduction of PTBP1 by either shRNA or miRNAs during miRNA-mediated neuronal reprogramming. PTBP1 overexpression in the miR-9/9*-124 expression background suppresses the PTBP2 induction.
(D) Left, an immunoblot showing that PTBP1 knockdown in HAFs resulted in induction of PTBP2, but PTBP2 expression becomes more pronounced in the presence of miR-9/9*-124 compared to PTBP1 knowdown only. Right, quantification of PTBP2 band intensity as relative fold changes compared to PTBP1 knockdown alone. Data were normalized to HSP90 from four independent experiments. The plots were represented in mean ± SEM. One-way ANOVA followed by Tukey's test (from top *** P = 0.0002, 0.0004; ns P = 0.8925).
(E) Top left, a schematic diagram of the experimental procedure. Right, photographs of day 30 miNs treated with CTL shRNA, PTBP2 shRNA, or PTBP2 shRNA with PTBP2 cDNA. Cells were immunostained for PTBP2 and MAP2. Bottom left, quantification of the percentage of MAP2-positive cells with two or more neurite processes over the total number of DAPI-positive cells. Scale bar = 50 μm. Data are represented as mean ± SEM. One-way ANOVA followed by Tukey's test (*** P < 0.0001; ** P 0.0016). shCTL n = MAP2 356/482; shPTBP2 n = MAP2 31/239; shPTBP2+PTBP2 n = MAP2 225/454.
(F) A model of differential miR-124 activity on PTB 3'UTRs during neuronal conversion.

alone condition (Figure 3D). In fact, PTBP2 was more upregulated with miR-9/9*-124 despite the more pronounced reduction of PTBP1 with shRNA (Figure 3D), demonstrating that miR-9/9*-124 accentuate PTBP2 expression beyond the level induced by PTBP1 downregulation.

Functional significance of PTBP2 expression for neuronal conversion

To probe the functional importance of *PTBP2* expression, we knocked down *PTBP2* with an shRNA during neuronal conversion. *PTBP2* shRNA completely impaired the induction of neurons marked by the loss of MAP2 expression, a neuronal marker (Figure 3E). The effect of shRNA was specific to *PTBP2* knockdown as supplementing *PTBP2* cDNA rescued the reprogramming defect (Figure 3E). These findings were somewhat surprising as the results from a previous study indicated that sequential reduction of PTBP2 by shRNA was found to promote maturation of reprogrammed neurons (Xue et al. 2016); however, our results indicate that at least at the initiation of reprogramming, PTBP2 is critical. While it is not clear why shRNA- versus miRNA-based reprogramming approaches lead to these different results, our results demonstrate the essential role of PTBP2, at least, at the onset of neuronal conversion. Furthermore, knocking down PTBP2 in primary cultured human neurons resulted in increased cell death as measured with SYTOX assay (Figure S4A-B), consistent with previous studies that showed the essential function of PTBP2 in primary neurons (Li et al., 2014).

We also performed Human Clariom D Assay in HAFs expressing the non-specific control miR-NS, miR-9/9*-124, or miR-9/9*-124 with *PTBP2* shRNA to identify genes whose expression and alternative splicing patterns were affected by the reduction of PTBP2. By two weeks, miR-9/9*-124-expressing cells showed significant downregulation of *PTBP1* and other

fibroblast-enriched genes such as *FBN1* and *S100A4*, and upregulation of *PTBP2* and neuronal genes (for example, *NEFM,* and *SNAP25*) in comparison to the control miR-NS (FC $\geq$ 1.5, ANOVA p-value < 0.05) (Figure S4C) (Abernathy et al., 2017). Alternative splicing events mediated by PTBP2 were examined by comparing spliced events between *PTBP2* shRNA and control shRNA (shCTL) conditions. We found that reducing PTBP2 led to changes in splicing events (-2 $\leq$ splicing index $\geq$ 2, ANOVA p-value < 0.05) indicated by red (positive splicing index) and green dots (negative splicing index) (Figure S4D). This analysis identified known splicing targets of PTBP2, such as the exon skipping or exclusion in *UNC13B*, *DLG4*, and *CADM3*, and inclusion in *DNM1* and *SMARCC2* transcripts (Figure S4D) (Li et al., 2014; Licatalosi et al., 2012; Vuong et al., 2016; Zheng et al., 2012). Comparing genes upregulated in response to miR-9/9*-124 to genes associated with PTBP2-mediated alternative splicing (differential splicing events between miR-9/9*-124-shCTL and shPTBP2 conditions), identified 1183 differentially spliced transcripts of genes involved in processes such as neuronal differentiation and signaling (Figure S4E) (Table S2). Altogether, our results support the role of PTBP2 as a crucial regulator of the neuronal program.

Differential sequence composition between PTBP1 and PTBP2 3'UTRs

Using PTBP1 downregulation and PTBP2 upregulation as a model, we sought to identify effectors that determine miR-124 function as a positive regulator. RNA-binding proteins (RBPs) have been shown to interact with miRNA-loaded RISC complexes to modulate target gene expression (Iadevaia and Gerber, 2015; Jiang and Coller, 2012; Plass et al., 2017). We ran the sequence of *PTBP2* 3'UTR through three RBP motif prediction databases, including RBPDB

(Cook et al., 2011), RBPmap (Paz et al., 2014), and beRBP (Yu et al., 2018) (Figure S5A). Across the three databases, two RBPs, ELAVL1 and PUM2, were consistently predicted to bind to *PTBP2* 3'UTR (Figure S5A). As PTBP2 upregulation occurs in neurons, we focused on the family of RBPs whose expression is neuronally enriched. Whereas *ELAVL1* and Pumilio family RBPs, *PUM2* or its homolog, *PUM1*, are ubiquitously expressed (Lin et al., 2018; Okano and Darnell, 1997; Spassov and Jurecic, 2002), other ELAVL family members, *ELAVL2*, *ELAVL3*, and *ELAVL4* (collectively referred to as neuronal *ELAVLs*, *nELAVLs*), have been shown to be neuronally enriched (Okano and Darnell, 1997). We also examined the HITS-CLIP data of nELAVLs in the human brain (Scheckel et al., 2016) and found nELAVLs to be highly enriched at *PTBP2* 3'UTR, in contrast to *PTBP1* 3'UTR (Figure S5B-C). Interestingly, *PTBP2* 3'UTR contains AU-rich elements (AREs) that ELAVLs have been shown to bind to (Ince-Dunn et al., 2012; Scheckel et al., 2016), in contrast to *PTBP1* 3'UTR that lacks the ARE (Figure S5B). Moreover, nELAVL binding mapped to the ARE around the first miR-124 site (s1; seed, highlighted in red) *PTBP2* 3'UTR (Figure S5C). We thus examined by qPCR if nELAVLs are induced during neuronal conversion as well as other brain-enriched RBP markers including NOVA-, RBFOX-family proteins, and SSRM4. We found selective upregulation of nELAVLs with other neuronal RBPs in miNs similarly to the human brain, in contrast to the ubiquitous expression of *ELAVL1* (Figure 4A) (Okano and Darnell, 1997). To determine if nELAVL induction occurs concurrently with PTBP2 upregulation, we assessed ELAVL expression at multiple time points of neuronal conversion. We found that the transcriptional activation of nELAVLs, with *ELAVL3* being the most robust one (blue), aligned with the upregulation of *PTBP2* (black) by nine days into reprogramming (Figure 4B).

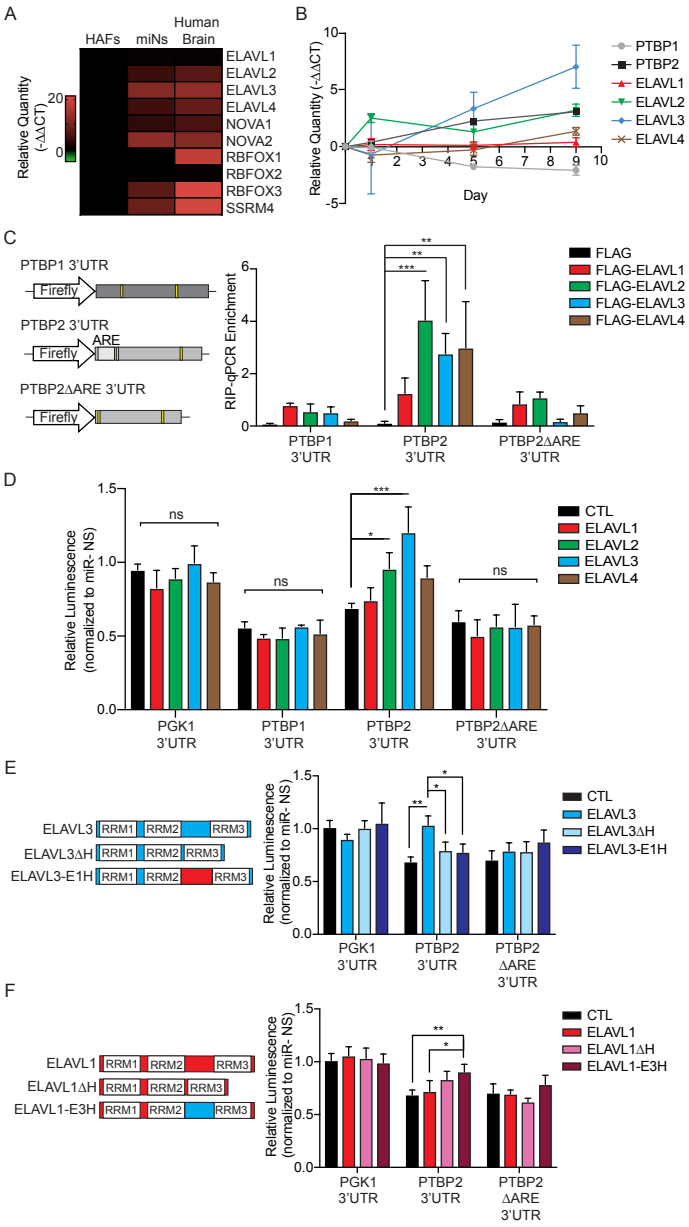

Figure 4. MiRNA-mediated PTBP2 upregulation requires nELAVL binding at PTBP2 3'UTR

(A) An expression heatmap of neuronal-enriched RBPs determined by qPCR in starting HAFs, day 20 miNs, and human brain RNA.

(B) Time course qPCR assays of PTB and ELAVL transcripts during neuronal reprogramming.

(C) Left, a diagram of luciferase constructs containing different PTB 3'UTRs: PTBP1 3'UTR, and PTBP2 3'UTR with and without (PTBP2ΔARE) the AU-rich element (ARE) used for RIP and luciferase assays. Right, RIP of individual FLAG-tagged ELAVLs 48 hrs after transfection. Enrichment normalized to input determined by qPCR for PTBP1 or PTBP2 3'UTR. Data are represented by mean ± SEM from three independent experiments. Two-way ANOVA followed by Dunnett's test (from left, PTBP2 3'UTR *** P = 0.0001, ** P = 0.0086, 0.0042).

(D) Luciferase assays with the addition of individual ELAVLs in the luciferase constructs containing the control PGK1, PTBP1, PTBP2 or PTBP2ΔARE 3'UTR. Luminescence was measured 48 hrs after the transfection and normalized miR-9/9*-124 to miR-NS control of each condition. Data are represented by mean ± SEM from at least three independent experiments. Two-way ANOVA followed by Dunnett's test (* P = 0.0312, *** P = 0.0001).

(E) Left, a schematic diagrm of ELAVL3 hinge mutants. Right, luciferase assays with the addition of wild-type ELAVL3 or ELAVL3 hinge mutants (ELAVL3Δ H: ELAVL3 hinge deletion; ELAVL3-E1H: ELAVL3 with ELAVL1 hinge). Luminescence was measured 48 hrs after transfection and normalized miR-9/9*-124 to miR-NS control of each condition. Data are represented by mean ± SEM from at least four independent experiments. Two-way ANOVA followed by Tukey's test (from left ** P = 0.0020, * P = 0.0435, * P = 0.0286).

(F) Left, a schematic diagram of ELAVL1 hinge mutants. Right, luciferase assays with the addition of wild-type ELAVL1 or ELAVL1 hinge mutants (ELAVL1 ΔH: ELAVL1 hinge deletion; ELAVL1-E3H: ELAVL1 with ELAVL3 hinge). Luminescence was measured 48 hrs after transfection and normalized miR-9/9*-124 to miR-NS control of each condition. Data represented in mean ± SEM from at least four independent experiments. Two-way ANOVA followed by Tukey's test (** P = 0.0069, * P = 0.0260).

MiRNA-mediated PTBP2 induction requires ELAVL3 binding at PTBP2 3'UTR

We then tested whether ARE within *PTBP2* 3'UTR would serve as a sequence that binds ELAVL proteins by expressing 3'UTRs of *PTBP1*, *PTBP2,* or *PTBP2* without ARE (*PTBP2ΔARE* 3'UTR) with individual FLAG-tagged ELAVLs (ELAVL1-4) in HEK293T cells (Figure 4C). RNA-immunoprecipitation (RIP) of FLAG-ELAVLs with FLAG antibody, followed by qPCR for detecting the loaded 3'UTRs using primers specific for either *PTBP1* or *PTBP2* displayed significant enrichment for *PTBP2* 3'UTR with nELAVL (ELAVL2, 3, and 4) pull-downs, while the binding of ELAVL1 to *PTBP2* 3'UTR was minimal. We could not detect significant enrichment for *PTBP1* 3'UTR for any of the ELAVLs (Figure 4C). Importantly, deleting ARE in *PTBP2* 3'UTR (*PTBP2ΔARE* 3'UTR) abolished the binding of nELAVL proteins to *PTBP2* 3'UTR (Figure 4C) indicating that ARE within *PTBP2* 3'UTR serves to recruit nELAVLs.

We then asked whether adding nELAVLs to the non-neuronal context of HEK293T cells, thereby reconstituting nELAVLs that become available during neuronal conversion, would alleviate miR-124-mediated repression of PTBP2 and enhance PTBP2 expression. Adding individual ELAVLs to control *PGK1* 3'UTR had no effect on luminescence (relative luminescence of ~ 1; *PGK1* 3'UTR histograms) (Figure 4D). Luciferase activities with *PTBP1* 3'UTR remained repressed upon miR-9/9*-124 expression compared to the control miR-NS irrespective of the ELAVL addition (relative luminescence of < 1; *PTBP1* 3'UTR histograms) (Figure 4D). MiR-9/9*-124 led to the repression *PTBP2* 3'UTR in the absence of ELAVLs (black, relative luminescence ratio < 1; *PTBP2* 3'UTR histograms) (Figure 4D). However,

adding ELAVL2 (green) and ELAVL3 (blue) significantly alleviated miR-9/9*-124-mediated repression on *PTBP2* 3'UTR, with especially ELAVL3 (blue) having the most significant effect on elevating the luciferase activity in comparison to the control construct (Figure 4D). To examine the requirement of ARE, we repeated the ELAVL addition experiments using the luciferase cassette with *PTBP2* 3'UTR lacking the ARE sequence (*PTBP2ΔARE*). Deleting ARE abolished the effect of ELAVL3 (blue) on *PTBP2* (*PTBP2ΔARE* 3'UTR histograms), which stayed repressed (Figure 4D), demonstrating the requirement of ELAVL3 and ARE for *PTBP2* upregulation by miR-124.

Selective activity of ELAVL3 on PTBP2 3'UTR is dependent on the hinge region

ELAVL1-4 members exhibit high sequence homology across all three functional RNA recognition motifs (RRMs) except for the non-conserved spacer region (also referred to as hinge region) flanked by RRM2 and RRM3 (Hinman et al., 2013; Okano and Darnell, 1997). To better understand the specificity of ELAVL3 on *PTBP2* 3'UTR regulation, we mutagenized the hinge region of *ELAVL1* and *ELAVL3* by deleting or swapping the hinge region (H) between *ELAVL1* and *ELAVL3*. Deleting the H in *ELAVL3* (*ELAVL3ΔH*) (light blue) abrogated the alleviating effect on *PTBP2* 3'UTR repression, whereas no effect was observed with *PGK1* 3'UTR (Figure 4E, *PGK1* 3'UTR histograms). Moreover, replacing the *ELAVL3* H with *ELAVL1* H (*ELAVL3-E1H*) (dark blue) led to the failure of alleviating the *PTBP2* 3'UTR repression (Figure 4E), and none of the *ELAVL3* variants (wild-type and mutants) had any effect on *PTBP2ΔARE* 3'UTR (Figure 4E, *PTBP2ΔARE* 3'UTR histograms). These results indicate that the specificity of ELAVL3 to *PTBP2* 3'UTR is mediated by the *ELAVL3* H region. This notion is further

supported by the increase in the luminescence readout of *PTBP2* 3'UTR in HEK293T cells when *ELAVL1* H is replaced by *ELAVL3* H (*ELAVL1-E3H*) (dark red) compared to wild-type *ELAVL1* (red) (Figure 4F, *PTBP2* 3'UTR histograms).

ELAVL3 promotes PTBP2 expression during neuronal reprogramming

To further examine if ELAVL3 would be critical for PTBP2 upregulation during the neuronal conversion of HAFs, we knocked down *ELAVL3* by shRNA (shELAVL3) to assess PTBP2 expression and neuronal reprogramming. Knocking down ELAVL3 resulted in the significant downregulation of PTBP2 expression as determined by immunostaining, qPCR, and immunoblotting analyses, and impairment of the conversion process (Figures 5A-C). This knockdown effect was specific for ELAVL3 downregulation as PTBP2 expression and neuronal fate acquisition could be rescued by overexpressing *ELAVL3* cDNA in the presence of shELAV3 (Figure 5A). It is noteworthy that reducing the function of other nELAVLs (ELAVL2 and 4) had a milder effect on PTBP2 expression (Figures 5B-C), highlighting the role of ELAVL3 as a primary driver for PTBP2 upregulation with miR-124.

Synergism between nELAVL and AGO requires miR-124 site in PTBP2 3'UTR

We further tested whether the miR-124 sites within *PTBP2* 3'UTR would also be critical for mediating the PTBP2 upregulation with ELAVL3. By mutating the miR-124 seed-match sequences within *PTBP2* 3'UTR (*PTBP2Δs1s2* 3'UTR), adding ELAVLs failed to enhance the luciferase activity over the control (CTL, black; relative luminescence ratio unchanged;

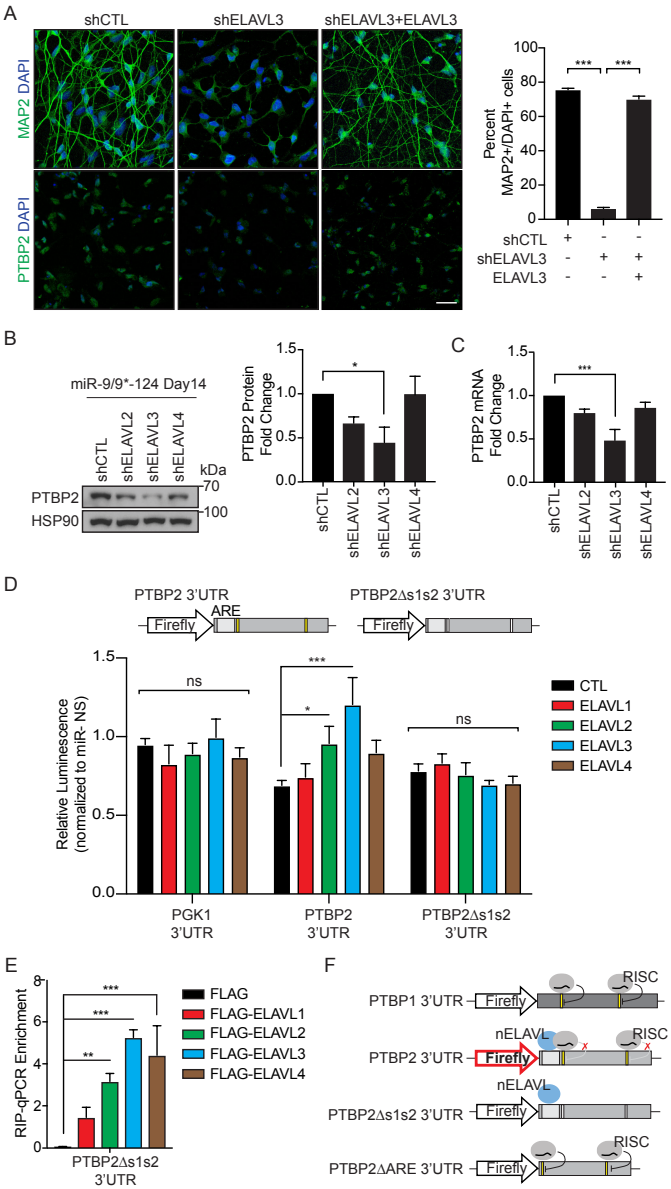

Figure 5. PTBP2 upregulation requires the synergism of nELAVL and miR-124
(A) Left, day 30 miNs with shRNA knockdown against CTL, ELAVL3, and ELAVL3 with ELAVL3 cDNA rescue. Cells were immunostained for MAP2 and PTBP2. Scale bar 50 = μm. Right, quantification of the percentage of MAP2-positive cells over the total number of DAPI-positive cells with two or more neurites (left). Data represented as mean ± SEM. One-way ANOVA followed by Tukey's test (from left, *** P < 0.0001, *** P < 0.0001). shCTL n = MAP2 803/1060; shELAVL3 n = MAP2 67/1052; shELAVL3 + ELAVL3 n = MAP2 431/617.
(B) Left, immunoblot analysis of PTBP2 in day14 miNs with knockdown against CTL, ELAVL2, ELAVL3, and ELAVL4. Right, quantification of the PTBP2 band intensity as a relative fold change compared to shCTL normalized to HSP90 in four independent experiments. Data are represented by mean ± SEM. One-way ANOVA followed by Dunnett's test (* P = 0.0422).
(C) The relative quantity of PTBP2 transcript upon individual nELAVL knockdown compared to CTL at day14 miNs determined by qPCR. Data are represented by mean ± SEM from 3 independent experiments. One-way ANOVA followed by Dunnett's test (*** P = 0.0001).
(D) Top, a diagram of luciferase constructs containing PTBP2 3'UTR with or without miR-124 sites (PTBP2Δs1s2). Bottom, luciferase assays with the addition of individual ELAVLs in PGK1 control, PTBP2, or PTBP2Δs1s2 3'UTR. Luminescence was measured 48 hrs after transfection and normalized miR-9/9*-124 to miR-NS control of each condition. Data are represented by mean ± SEM from at least three independent experiments.Two-way ANOVA followed by Dunnett's test (* P = 0.0312, *** P = 0.0001).
(E) RIP of individual FLAG-tagged ELAVLs in PTBP2Δs1s2 3'UTR 48 hrs after transfection. Enrichment normalized to input determined through qPCR against PTBP2 3'UTR. Data are represented by mean ± SEM from three independent experiments. Two-way ANOVA followed by Dunnett's test (from left, PTBP2Δs1s2 3'UTR ** P = 0.0018, *** P = 0.0001, *** P = 0.0001).
(F) A schematic summary of nELAVL and RISC activities on PTB 3'UTRs.

PTBP2Δs1s2 3'UTR histograms) (Figure 5D). This result is in contrast to wild-type *PTBP2* 3'UTR where ELAVL3 can enhance luciferase activity in the presence of miR-124 target sites (Figures 4D, 5D). Interestingly, the lack of the increased luminescence with ELAVL3 addition was not due to the failure of ELAVL binding to *PTBP2Δs1s2* 3'UTR because qPCR analysis with nELAVL-RIP showed persistent binding of ELAVLs to *PTBP2Δs1s2* 3'UTR (Figure 5E). These results altogether suggest the requirement of both ARE and miR-124 sites in *PTBP2* 3'UTR for PTBP2 upregulation (Figure 5F).

Neuronal genes are downregulated upon loss of miR-124 and ELAVL3 in human neurons

To test whether the synergism of miR-124 and ELAVL3 for miRNA-mediated upregulation is unique to PTBP2 or a broader mechanism applicable to other genes beyond reprogrammed neurons, we performed loss-of-function studies on primary human neurons (HNs). With the same TuD-miR-124 and shELAVL3 constructs used in reprogrammed neurons, miR-124 and ELAVL3 were knockdown in HNs and processed for RNA-seq (Figures 6A-B and S6A). To identify potential targets upregulated by miR-124 and ELAVL3 in HNs, we focused on genes suppressed upon expression of TuD-miR-124 and shELAVL3 (KD, $Log_2FC \leq -1$; adj.P-value < 0.05) compared to CTL (Figure 6B). Many of these downregulated genes are neuronal-related, including *MAP2*, *PTBP2*, *SCN1A*, and *SEMA6A* (Figure 6B). Despite the downregulation of several neuronal transcripts, overall neuronal identity remains intact as expression of neuronal markers such as *RBFOX2*, *FMR1*, and *NEFL* remain similar between CTL and KD HNs (Figure S6B). Furthermore, we also do not observe an emergence of progenitor marker expression upon knockdown of both miR-124 and ELAVL3 (Figure S6B).

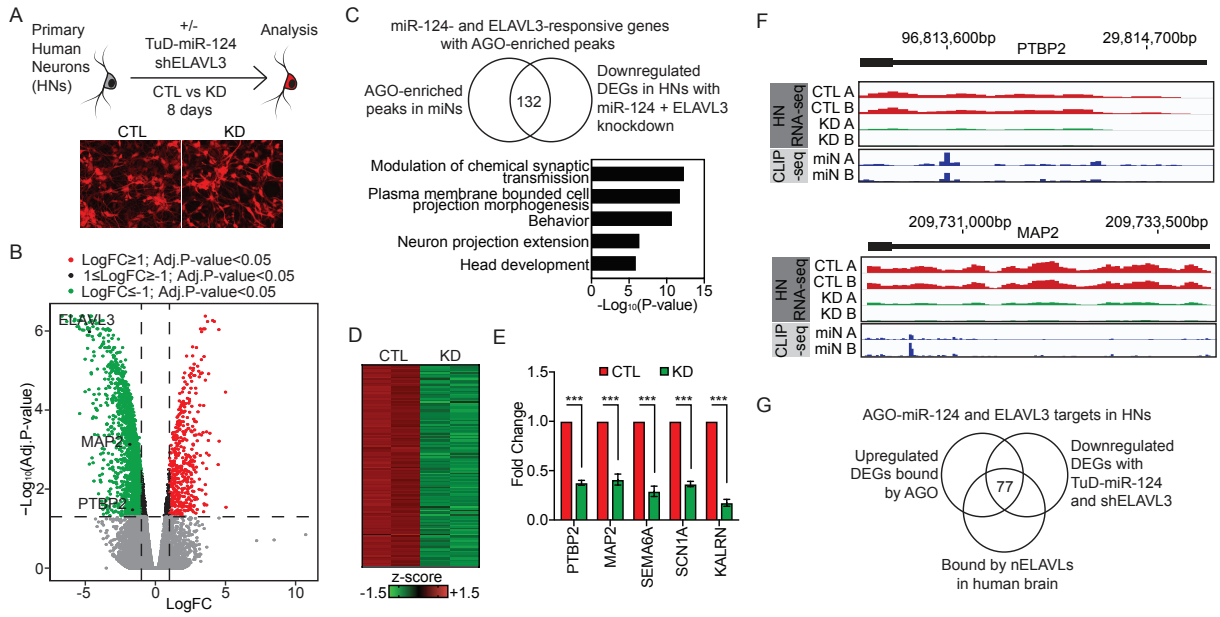

Figure 6. MiRNA-mediated upregulation of neuronal genes in primary human neurons

(A) Top, a schematic diagram of the experimental procedure using primary human neurons (HNs). Bottom, images of HNs marked by TurboRFP reporter in the non-specific miRNA or miR-124 tough decoy.

(B) A volcano plot of differentially expressed genes between CTL and KD conditions with TuD-miR-124 and shELAVL3 treatment. A selection of downregulated genes are highlighted (ELAVL3, MAP2, and PTBP2). Red dots, HN mRNA expression Log2FC ≥ 1; adj.P-value < 0.05. Green dots, HN mRNA expression Log2FC ≤ -1; Adj.P-value < 0.05.

(C) Top, by overlapping downregulated DEGs in (A) to previously identified upregulated AGO-enriched targets (Figure 1), 132 genes were identified to habor AGO peaks in miNs and are downregulated with miR-124 an ELAVL3 knockdown in HNs. Bottom, top biological GO terms associated with the 102 genes.

(D) A heatmap of z-scores of the 132 genes identified in (B) from RNA-seq comparing KD and CTL in HNs.

(E) RT-qPCR validation of a selection of the identified downregulated genes in HNs (C) that are found to be commonly targeted by both miNs and HNs (B). Data are represented in ± SEM from three independent experiments. Two-tailed unpaired t-test (all, *** P < 0.001).

(F) Track views of HN RNA-seq tracks (top) and miN AGO HITS-CLIP tracks (bottom) for gene examples showing reduced expression upon knockdown of miR-124 and ELAVL3 in HNs (over CTL), and AGO-enriched peaks at the 3'UTR.

(G) A venn diagram of AGO-miR-124 targets in HNs overlapped with nELAVL-bound targets in the human brain.

To ensure that these downregulated genes are miR-124 targets, we compared the downregulated DEGs from HNs to upregulated DEGs in day 20 miNs that also harbor AGO-enriched peaks (Figure 1). This comparison resulted in a set of 132 target genes associated with biological GO terms related to neuronal development and projection (Figure 6C, Table S3), further validating miR-124 as a positive regulator of the neuronal program. Examples of some these identified targets in HNs also validated in qPCR include *PTBP2*, *MAP2*, *SEMA6A*, *SCN1A*, and *KALRN* (Figures 6D-F). Together our data support the notion that miR-124-mediated upregulation of neuronal genes is not unique to PTBP2 in reprogramming context, but applicable to other neuronal genes in actual human neurons.

MiR-124 and nELAVL interaction for other neuronal transcripts

Using existing nELAVL HITS-CLIP of the human brain (Scheckel et al., 2016), we performed a comparative analysis with our HNs dataset to examine if these upregulated neuronal transcripts are likely targets of nELAVLs. First, by overlapping i) upregulated neuronal DEGs bound by AGO HITS-CLIPs (Figure 1), ii) DEGs responsive to miR-124 tough decoy and *ELAVL3* shRNA in HNs (Figure 6), and iii) genes bound by nELAVLs in the human brain (Scheckel et al., 2016), we identified 77 genes, including *PTBP2*, *MAP2*, *SLCA48, KALRN, BCL7A,* and *SCN1A* enriched for neuronal biological terms generally involved in synaptic processes (Figures 6G and S7, Table S4). Based on these comparisons, similar to what we observed in miNs, miR-124 and ELAVL3 appear to collectively upregulate a set of neuronal genes that are likely critical for neuronal function in primary HNs.

Neuronal properties affected by miR-124 and nELAVLs

As our AGO-HITS-CLIP and miR-124 knockdown data in miNs indicate that neuronal genes are preferentially targeted as cells acquire the neuronal fate (Figures 1 and 2), we examined the global transcriptome changes of our knockdown (KD) and control (CTL) conditions in HNs with LONGO analysis to assess changes in long gene expression (LGE), a measure of neuronal identity and maturation (Gabel et al., 2015; King et al., 2013; McCoy et al., 2018; McCoy and Fire, 2020; Sugino et al., 2014). Overall, knockdown of miR-124 and ELAVL3 (KD, green) in HNs resulted in reduced LGE compared to control (CTL, red), suggesting that both players are likely essential for the expression of long genes (Figure 7A).

As a number of identified neuronal genes targeted by AGO-miR-124 and ELAVL3 in HNs are implicated in neuronal function and morphology such as *SCN1A*, *SLC4A8*, *ANK3*, and *MAP2*, reflective of reduced overall LGE (Figures 7A and S7A, Table S4), we examined a few neuronal properties in CTL and KD HNs. We first performed electrophysiology and found KD HNs exhibited reduced inward sodium current as compared to CTL HNs (Figures 7B and S6C-D) which we reasoned to be attributed to a number of downregulated channel genes in KD HNs. However, other electrical properties such as resting membrane potential and action potential firing appear similar between CTL and KD HNs (Figures S6D-E). In addition, as we observed reduced neurite complexity in our KD cells compared to CTL HNs, we sought to measure features such as average neurite length and average number of neurite branches between the two conditions. Overall, we found that KD HNs not only have shorter average neurite length per cell, but also have fewer branches per cell compared to CTL (Figures 7C-E).

Reduced LGE in primary HNs with both miR-124 and ELAVL3 knockdown suggests that LGE is a transcriptomic phenotype reflective of altered neuronal features observed and

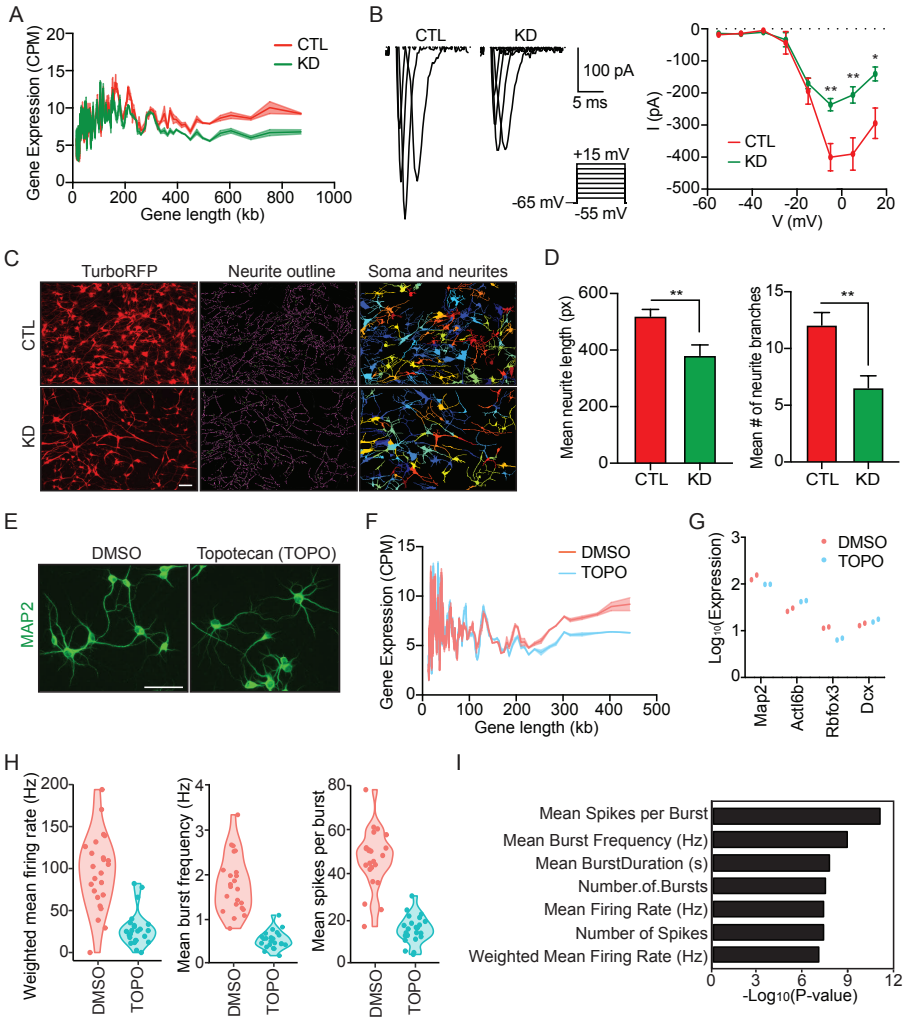

Figure 7. Long gene dysregulation results in altered neuronal properties
(A) LONGO plot showing reduced long gene expression upon knockdown of miR-124 and ELAVL3 (KD; green) compared to CTL (red). Lines show mean gene expression and ribbons show standard error of the mean (SEM).
(B) Left, voltage-clamp traces of CTL and KD (TuD-miR-124 and shELAVL3) HNs. Right, average I-V curve of for all recorded CTL and KD HNs. Data are represented in ± SEM from seven recorded cells from each condition. Two-tailed unpaired t-test (from left, ** P = 0.00434 ; ** P < 0.00681 ; * P = 0.01233).
(C) Representative images of CTL and KD HNs marked by TurboRFP reporter. Processed images by CellProfiler to identify neurites and associated cell soma. Scale bar = 100 µm.
(D) Left, mean neurite length measurement of CTL and KD HNs. Data are represented in ± SEM from seven separate fields of view; CTL n = 768, KD n = 677. Two-tailed unpaired t-test (** P = 0.0092). Right, mean number of neurite branches in CTL and KD HNs. Data are represented in ± SEM from seven separate fields of view; CTL n = 768, KD n = 677. Two-tailed unpaired t-test (** P = 0.0038).
(E) Representative images of primary rat neurons stained for MAP2 after treatment with DMSO control or Topotecan (TOPO).
(F) LONGO plot showing reduced long gene expression upon treatment with TOPO (blue) compared to DMSO (red) in primary rat neurons. Lines show mean gene expression and ribbons show standard error of the mean (SEM).
(G) Expression of a select unaffected neuronal markers between DMSO and TOPO treatments.
(H) MEA readout for mean firing rate, burst frequency, and spikes per bursts of primary rat neurons treatment with DMSO or TOPO.
(I) P-value of the various measured electrophysiological properties from MEA including those shown in (H).

measured in HNs. To independently validate the correlation between LGE and neuronal maturity, we also treated primary rat neurons with Topotecan (TOPO), an inhibitor of Topoisomerase I known to reduce LGE in neurons (King et al., 2013; Mabb et al., 2016, 2014). Primary rat neurons treated with TOPO (blue) were found to display a reduction in LGE when compared to the control condition (DMSO, red) (Figures 7E-F) while the TOPO-treated cells still maintained the expression of other neuronal markers such as *Map2*, *Actl6b*, *Rbfox3* and *Dcx* (Figure 7G). To further assess the consequences of LGE reduction in neurons, we measured electrophysiological properties using a microelectrode array (MEA). TOPO-treated neurons exhibited altered electrophysiological properties compared to DMSO control, including reduced mean firing rate, mean burst frequency, and number of spikes per burst (Figures 7H-I), demonstrating that LGE is a transcriptomic feature related to the functional maturity of neurons. Therefore, our results support the notion that miR-124, in synergy with ELAVL3, promote neuronal maturity by positively regulating their target genes, as evidenced by their effect on LGE in human neurons. Based on PTBP2, we delineated a mechanism on how miR-124 and ELAVL3 can promote the expression of their targets and we anticipate that some of the additional identified long genes important for neuronal differentiation and function are likely upregulated in a similar manner.

Materials and Methods

Cell culture

Primary human fibroblasts used in this study was from a 22-year-old female (GM02171, NIGMS Coriell Institute for Medical Research) while human neonatal fibroblasts (ScienCell, 2310) was used exclusively for the HITS-CLIP experiment. Fibroblasts were maintained in high

glucose Dulbecco's Modified Eagle Medium (Gibco, 11960044) containing 10% FBS (Gibco, 10437028), MEM non-essential amino acids (Gibco, 11140050), sodium pyruvate (Gibco, 11360070), GlutaMAX (Gibco, 35050061), HEPES (Gibco, 15630080), penicillin-streptomycin (Gibco, 15130122), and 2-mercaptoethanol (Gibco, 21985023) at 37°C. Primary human neurons were obtained commercially (ScienCell, 1520) with gender and age of the source undisclosed Human neurons were maintained in neuronal media (NM; ScienCell, 1521) at 37°C. E18 rat cortex (BrainBits®, FSDECX1M) were grown in STEMdiff™ Neural Induction Medium (STEMCELL Technologies, 05835).

Lenti-X 293T (Clontech, 632180) cells were maintained in high glucose Dulbecco's Modified Eagle Medium (Gibco, 11960044) containing 10% FBS (Gibco, 10437028), MEM non-essential amino acids (Gibco, 11140050), sodium pyruvate (Gibco, 11360070), GlutaMAX (Gibco, 35050061), HEPES (Gibco, 15630080), penicillin-streptomycin (Gibco, 15130122), and 2-mercaptoethanol (Gibco, 21985023) at 37°C.
-streptomycin (Gibco, 15130122), and 2-mercaptoethanol (Gibco, 21985023) at 37°C.

MiR-9/9*-124-mediated neuronal conversion

To initiate reprogramming, doxycycline-inducible pT-BclXL-miR-9/9*-124 (Addgene, 60857) and reverse tetracycline-controlled transactivator rtTA (Addgene, 66810) lentivirus with 8 ug/mL polybrene (Sigma, H9268) was added to a plate of confluent fibroblasts and spinfected at 37°C for 30 min at 1,000xG. Full media change with 1 μg/mL doxycycline (DOX; Sigma-Aldrich, D9891) occurred the following day. Two days following transduction, cells underwent another media change supplemented with DOX and respective antibiotics (Puromycin, Life Technologies, A11138-03; Blasticidin S HCl, Life Technologies, A11139-03). Five days after

transduction, cells were plated onto poly-l-ornithine (Sigma-Aldrich, P4957), fibronectin (Sigma-Aldrich, F4759), and laminin (Sigma-Aldrich, L2020) coated coverslips or onto 10cm^2 Primaria plates (Corning, 353803) followed by full media switch to neuronal media (NM; ScienCell, 1521) the next day supplemented with 200 μM dibutyl-cyclic AMP (cAMP; Sigma-Aldrich, D0627), 1 mM valproic acid (VPA; Sigma Aldrich, P4543), 10 ng/mL human BDNF (PeproTech, 450-02), 10 ng/mL human NT-3 (Peprotech, 450-03), 1 μM retinoic acid (RA; Sigma-Aldrich, R2625), RevitaCell supplement (Gibco, A2644501), and antibiotics. DOX was supplemented every 2 days while half media changes occurred every 4 days until day 30.

Plasmids and cloning

For luciferase assay, full length 3'UTR of target transcripts were cloned and ligated into pmirGLO vector. For mutagenizing miR-124 target sites, QuikChange XL site-directed mutagenesis kit (Agilent, 200516) was used according to the manufacturer's protocol. Using the same UTR sequences, 3'UTR was attached immediately downstream of a destablized EGFP reporter and subcloned into lentiviral vector. Sequences for shRNAs were synthesized through Integrated DNA Technologies, annealed, and ligated into the pLKO.1 vector (Addgene, 8453 or 26655). Overexpression vectors of either lentiviral (N106 or N174) or mammalian expression (pcDNA3.1+, Invtrogen, V79020) was cut using NotI cut site (NEB, R0189) for insert ligation. Tough decoy for miR-124 was synthesized (GeneScript) and subcloned into pLemir vector using MluI (NEB, R0198) and NotI sites.

Lentivirus production

Lentivirus was produced as previously described (Richner et al., 2015). Briefly, 1.5 μg pMD2.G, 4.5 μg psPAX2, 6 μg of plasmid in lentiviral backbone, 600 μl Opti-MEM (Life

Technologies, 31985) and 48 µl of 2 mg/mL polyethyleneimine (PEI; Polysciences, 24765) were mixed and transfected into Lenti-X 293T (Clontech, 632180) plated at $6x10^6$ cells per 10 cm^2 dish. Media was changed the following day, and viral supernatant was collected, filtered and spun at 70,000xG for 2 hr at 4°C two days later. The viral pellet collected per 10 cm^2 dish was resuspended in 1 mL PBS.

Immunostaining analysis

Cells were fixed with 4% paraformaldehyde (PFA; Electron Microscopy Sciences, 15710) for 20 mins at room temperature (RT) followed by three washes with PBS. Cells were permeabilized and blocked in 0.3% TritonX-100, 2% normal goat serum (NGS; Jackson ImmunoResearch Laboratories, 005-000-121) and 5% bovine serum albumin (BSA; Sigma-Aldrich, A7906) in PBS for 1 hr at RT prior to incubation with primary antibodies overnight at 4°C. After three washes with PBS, cells were incubated with respective secondary antibodies for 1 hr at RT. Coverslips were mounted onto coverslides with ProLong Gold antifade reagent (Invitrogen, P36934) for imaging using Leica SP5X white light laser confocal system with Leica Application Suite (LAS) Advanced Fluorescence. See Supplemental Table S4 for a list of antibodies used.

SYTOX assay

SYTOX assay was performed as previously described (Victor et al., 2018). Briefly, 0.1 µM SYTOX gene nucleic acid stain (Invitrogen, S7020) and 1 µl/mL of Hoeschst 33342 (Thermo Scientific, 66249) were added into cell medium. Samples were incubated for at least 15 mins in 37°C prior to imaging. Images were taken using Leica DMI 4000B inverted microscope with Leica Application Suite (LAS) Advanced Fluorescence.

Luciferase assay

HEK 293 cells plated in 96-well plate were transfected with 100 ng of pSilencer-miRNA, 100 ng of pmirGLO containing 3'UTR of interest, and PEI (Polysciences, 24765) with Opti-MEM (Life Technologies, 31985). Forty-eight hours after transfection, luciferase activity was assayed using Dual-Glo luciferase assay system (Promega, E2920) according to the manufacturer's protocol using Synergy H1 Hybrid plate reader (BioTek). Luciferase activity was obtained by normalizing firefly luminescence to renilla luminescence (luciferase activity = firefly/renilla) followed by normalizing to respective pSilencer-miR-NS control.

Flow cytometry

Destabilized EGFP reporter with or without 3'UTR of interest was transduced into HEK 293 cells to establish a stable reporter containing cell line with Blasticidin S HCl (Life Technologies, A11139-03) selection. The day following transduction with miR-9/9*-124 lentivirus, media was changed with the addition of DOX (Sigma-Aldrich, D9891). At day 3, media change was supplemented with DOX and puromycin (Life Technologies, A11138-03). DOX was supplemented every 2 days following transduction. At day 10, cells were imaged, and collected for flow cytometry. Briefly, cells were collected in PBS and incubated with propidium iodide (PI; Sigma-Aldrich, P4861) on ice until ready. Using FACSCalibur (BD Biosciences), all PI-negative cell population was obtained for the gating of GFP-negative and -positive cell population.

Quantitative reverse transcription PCR

Total RNA of cells was extracted using TRIzol Reagent (Invitrogen, 15596026). Reverse transcription was performed using SuperScript III first strand synthesis system for RT-PCR (Invitrogen, 18080-051) according to the manufacturer's protocol from fibroblasts, reprogrammed neurons, and human brain total RNA (Invitrogen, AM7962). Quantitative PCR was performed using SYBR Green PCR master mix (Applied Biosystems, 4309155) and StepOnePlus Real-Time PCR system (Applied Biosystems, 4376600) according to the manufacturer's protocol against target genes.

HITS-CLIP

AGO HITS-CLIP was performed on cells after 2 weeks into reprogramming of miR-NS or miR-9/9*-124-expressing neonatal fibroblasts (ScienCell, 2310) at day 14 and day 21. Cells were harvested, UV-crosslinked, lysed, and processed according to Moore et al. 2014. Briefly, cross-linked cells were lysed and treated with RQ1 DNase (Promega, M6101) and RNaseA (Thermo). Complex containing AGO-miRNA-mRNA were immunoprecipitated overnight at 4°C with pan-AGO antibody. The immunoprecipitated complex was radio-labelled and extracted after running on NuPAGE gel (Thermo). RNA from the 130kDa band was extracted for sequencing using TruSeq Small RNA Library Preparation Kits (San Diego, CA). Samples were sequences using Illumina HiSeq 2500 platform at the Genome Technology Access Center (GTAC) at Washington University School of Medicine, St. Louis.

MiRNA Tough Decoy RNA-seq

Total RNA was extracted from day 20 cells expressing miR-9/9*-124 + TuD-miR-NS, and miR-9/9*-124 + TuD-miR-124 using TRIzol Reagent (Invitrogen, 15596026) in combination with RNeasy micro kit (Qiagen, 74004). RNA quality (RIN $\geq$ 9.6) was determined

with 2100 Bioanalyzer (Agilent) and samples underwent low input Takara-Clontech SMARTer kit (Takara, 639490) library preparation. Samples were sequenced using NovaSeq S4 and processed at the Genome Technology Access Center (GTAC) at Washington University School of Medicine, St. Louis. For human neurons, total RNA was extracted from HNs after 8 days of tough decoy and shRNA treatment using TRIzol Reagent (Invitrogen, 15596026) in combination with RNeasy micro kit (Qiagen, 74004). RNA quality (RIN ≥ 8.4) was determined with 2100 Bioanalyzer (Agilent) and samples underwent TruSeq Stranded total RNA sequencing kit library preparation. Samples were sequenced using NovaSeq6000 through DNA Link (San Diego, CA).

Human Clariom D Microarray

For Human Clariom D Array (Affymetrix), total RNA was extracted from day 14 cells expressing miR-NS, miR-9/9*-124 + shCTL, and miR-9/9*-124 + shPTBP2 using TRIzol Reagent in combination with RNeasy mini kit (Qiagen, 74104). RNA quality (RIN > 9.6) was determined with 2100 Bioanalyzer and samples (biological duplicates each) underwent amplification and hybridization according to manufacturer's protocol by GTAC at Washington University School of Medicine, St. Louis.

Immunoblot analysis

Cells were lysed with sonication (Diagenode, UCD-200) in RIPA buffer (Thermo Scientific, 89900) supplemented with protease inhibitor cocktail tablet (Roche, 04693132001). Protein concentration of cleared lysate was measured using Pierce BCA protein assay kit (Thermo Scientific, 23227) and read with Synergy H1 Hybrid plate reader (BioTek). Lysate and sample buffer (Life Technologies, NP0008) were boiled, separated with Bis-Tris gels, and transferred to nitrocellulose membrane (GE Healthcare Life Sciences, 10600006). Membrane

was blocked with 5% milk for 1 hr at RT and incubated with primary antibody overnight at 4°C. After three washes of TBST (1X TBS and 0.1% Tween-20), the membrane was incubated with respective horseradish peroxidase-conjugated antibody for 1 hr at RT followed by three washes with TBST. Blots were developed with ECL system (Thermo Scientific, 34580) and imaged or developed onto film. See Supplemental Table S3 for a list of antibodies used.

Immunoprecipitation analysis

Cells were lysed with sonication (Diagenode, UCD-200) in IP buffer (20 mM HEPES, 150 mM NaCl, 10% glycerol, 5 mM EDTA, 1% Triton X-100) supplemented with protease inhibitor cocktail tablet (Roche, 04693132001). Cleared lysate was incubated with anti-FLAG M2 magnetic beads (Sigma-Aldrich, M8823) overnight with rotation at 4°C. The beads were washed three times with IP buffer and bound proteins were boiled and eluted with sample buffer (Life Technologies, NP0008), separated with Bis-Tris gels, and immunoblotted.

RNA-IP

Cells were lysed with sonication (Diagenode, UCD-200) in IP buffer (20 mM HEPES, 150 mM NaCl, 10% glycerol, 5 mM EDTA, 1% Triton X-100) supplemented with protease inhibitor cocktail tablet (Roche, 04693132001). Cleared lysate was incubated with anti-FLAG magnetic beads (Sigma-Aldrich, M8823) overnight with rotation at 4°C beads. The beads were washed three times with IP buffer and resuspended in 90 ul of IP buffer with proteinase K (NEB, P8107S) for 30 mins at 37°C. To extract RNA, 1 mL of TRIzol Reagent (Invitrogen, 15596026) was added to the bead slurry. Final RNA was DNase I (Invitrogen, 18068015) treated prior to RT-qPCR.

Electrophysiology

Whole-cell patch-clamp recordings were performed as previously described (Victor et al., 2018). Briefly, HNs (ScienCell, 1521) were recording within 8 to 10 days after tough decoy and shRNA transduction. Recordings were acquired using pCLAMP 10 software, multipliclamp 700B amplifier, and Digidata 1550 digitizer (Molecular Devices, CA). Glass electrode pipettes were pulled from borosilicate glass (1B120F-4, World Precision) to obtain pipette resistance ranging from 5 – 8 MΩ using next generation micropipette puller (P-1000, Sutter Instrument). External solution is consist of 140 mM NaCl, 3 mM KCl, 10 mM Glucose, 10 mM HEPES, 2 mM $CaCl_2$ and 1 mM $MgCl_2$, and internal solution is consist of 130 mM K-Gluconate, 4 mM NaCl, 2 mM $MgCl_2$, 1 mM EGTA, and 10 mM HEPES (adjusted to pH 7.25 with KOH) were used for recording. For all recordings, the membrane potentials were held at -65 mV.

Microelectrode array

E18 rat cortical neurons (BrainBits, FSDECX1M) were plated onto a 24-well cell culture microelectrode array plate (Axion Biosystems, M384-tMEA-24W). Prior to plating, 1 ml of sterile water and 10 µl of PEI (Sigma-Aldrich, 03880) at 0.5% diluted in 0.1 M HEPES pH 8.0 (Caymen Chemical Company, 700014) was added to the center of each well. After incubating overnight at 37 °C, each well was washed 4x with sterile water, and allowed to dry for 15 minutes. 10 µl of Laminin (Sigma-Aldrich, L2020) at 10 µg/mL diluted in cold DMEM/F-12 (ThermoFisher, 11320082) was added to each well and incubated at 37 °C for 2 hours. Laminin was aspirated prior to plating neurons. 24 hours after plating, neurons were cultured in BrainPhys Neuronal Medium and SM1 supplement (STEMCELL Technologies, 05792) with either Topotecan (Sigma-Aldrich, T2705) at a final concentration of 300 nM in DMSO (0.05% DMSO

final concentration) or DMSO control for one week before recording electrophysiological activity using a Maestro MEA plate reader (Axion Biosystems).

GO enrichment analysis

Gene ontology analyses were performed using Metascape (Tripathi et al., 2015) with minimum overlap of 3, P-value cutoff of 0.01, and minimum enrichment of 1.5. Entire gene list was used for each GO analysis.

RNAhybrid miRNA-target duplex analysis

To predict the presence of miR-124-3p binding sites at HITS-CLIP peaks, peak sequences were extracted by on the genomic coordinates and processed through RNAhybrid (Rehmsmeier, 2004) against miR-124-3p miRNA sequence with at least a free energy threshold of -20 kcal/mol.

RBP binding analysis

RNA-binding protein prediction database/software, RBPDB (Cook et al., 2011), RBPmap (Paz et al., 2014), and beRBP (Yu et al., 2018) for *PTBP2* 3'UTR sequence were used. Default criteria were selected for all three software for non-bias prediction of any human RBP motifs.

Neurite length measurement

Images of HNs marked by TurboRFP were processed through CellProfiler 3.1.9 (McQuin et al., 2018). Briefly, neurite feature was enhanced prior to the identification of primary object or soma between 25 – 100 pixel unit in diameter, followed by the identification of secondary object based on neurite feature. A morphological skeleton was made based on overlaying the identified

objects and mean neurite lengths and branches were then measured using measure object skeleton module.

LONGO analysis

LGE for human and rat neurons were determined by through the LONGO platform (McCoy et al., 2018) . LONGO analysis output of gene expression (CPM) over gene length was used to generate the LONGO plot.

Data Analyses

AGO HITS-CLIP reads for miR-NS and miR-9/9*-124-expressing cells at least two weeks into reprogramming were trimmed and aligned to human genome hg38 using STAR with default parameters. Differential peaks between miR-9/9*-124 and miR-NS conditions were detected using MACS (Feng et al., 2012; Zhang et al., 2008) with the following criteria: mfold bound of 5 – 50, fragment size of 100, and FDR > 0.05. HITS-CLIP datasets will be publicly available.

RNA-seq for day 20 miNs expressing either CTL TuD-miR-NS or TuD-miR-124 was analyzed by GTAC's RNA-seq pipeline. Briefly, reads were aligned to hg38 with STAR and processed through EdgeR (Robinson et al., 2010) to obtain differentially expressed genes with adj. p-value of < 0.05. RNA-seq dataset consisting of TuD-miR-NS and TuD-miR-124 at day 20 will be publicly available.

RNA-seq for HNs treated with either CTL or tough decoy against miR-124 and shRNA against ELAVL3 (KD) was aligned through Partek® Flow® software (Partek Inc., 2020) to generate gene counts. Briefly, reads were aligned to hg38 with STAR and processed through

EdgeR (Robinson et al., 2010) to obtain differentially expressed genes with adj. p-value of < 0.05 and Log_2FC of ≤ -1 and ≥ 1. RNA-seq dataset consisting of CTL and KD treatments from HNs will be publicly available.

RNA-seq for primary rat neurons treated with either DMSO or Topotecan (TOPO) were aligned to the Ensembl release 76 top-level assembly with STAR. Transcript counts were produced by Sailfish version 0.6.3. All gene-level and transcript counts were then imported into the R/Bioconductor package EdgeR and TMM normalization size factors were calculated to adjust samples for differences in library size. RNA-seq dataset consisting of DMSO and TOPO treatments from rat neurons will be publicly available.

Human Clariom D Array data was analyzed using manufacturer's software, Expression Console followed by Transcriptome Analysis Console (TAC). For gene level analysis, genes comparing miR-9/9*-124 vs miR-NS linear fold change of ≥ 1.5 and ANOVA $P < 0.05$ were considered to upregulated in neuronal conditions. For splicing analysis, splicing events with linear splicing index ≤ -2 and ≥ 2, ANOVA $P < 0.05$ were considered significant splicing events. Human Clariom D array dataset consisting of miR-NS, miR-9/9*-124 with shCTL, and miR-9/9*-124 with shPTBP2 at day 14 will be publicly available.

Author Contributions

Y.L.L. conducted experiments shown in Figures 2-7 and associated supplementary Figures 1, 3-8. Y.J.L. conducted experiments shown in Figure 1 and supplementary Figure 2. M.J.M. conducted experiments shown in Figure 7. A.S.Y. supervised the study. Y.L.L. and A.S.Y. wrote the manuscript.

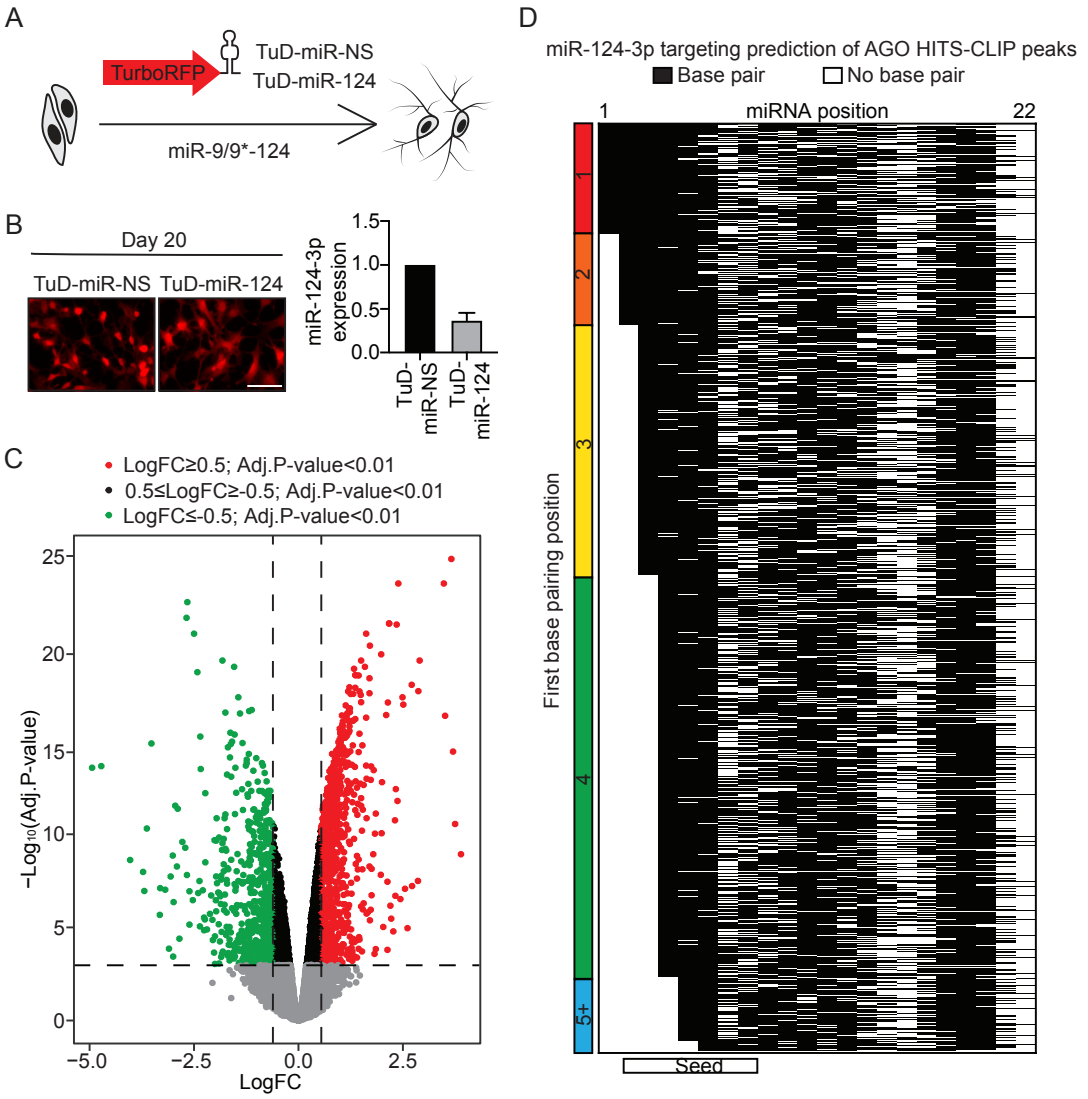

Figure S1. MiR-124 target genes during neuronal reprogramming
(A) A schematic diagram of the construct expressing the turbo-RFP reporter attached to the tough decoy (TuD) delivered into miNs.
(B) Left, day 20 miNs showing RFP expression of cells with TuD-miR-NS or TuD-miR-124. Right, Taqman qPCR for mature miR-124-3p showing reduced miR-124 expression upon TuD-miR-124 treatment compared to TuD-miR-NS control. Scale bar = 75 μm.
(C) A volcano plot of DEGs (TuD-miR-124 over the TuD-miR-NS control) in day 20 miNs.
(D) RNAhybrid predictions of base-pairing between miR-123-3p and extracted CLIP sequences of targets from Figure 2 with an energy threshold of -20 kcal/mol or less. The heatmap shows the base-pairing position between miR-124-3p and extracted sequences from AGO HITS-CLIP peaks: base-pairing = black, and gaps or no base-pairing = white.

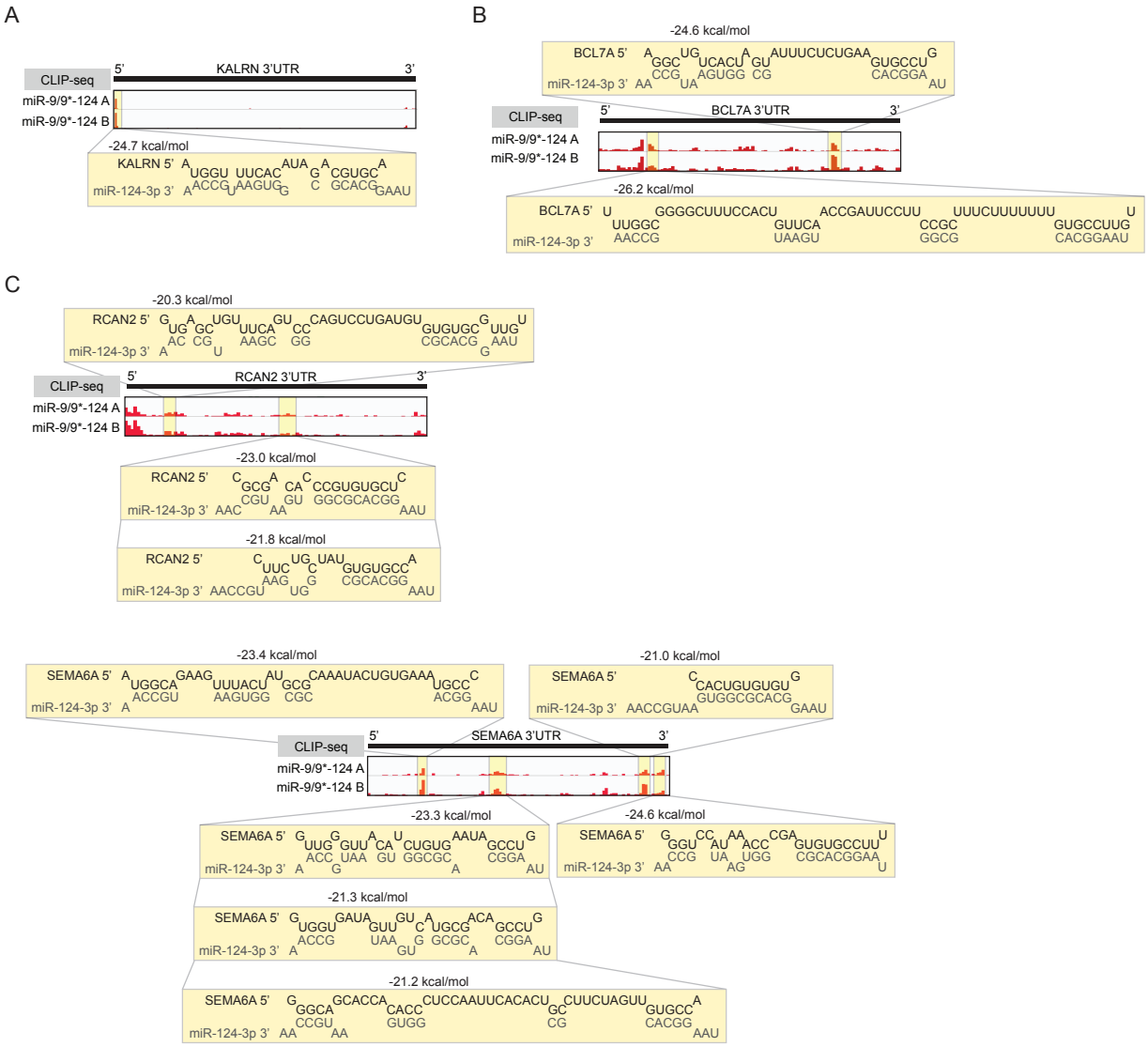

Figure S2. Examples of RNAhybrid prediction of miR-124-3p hybridization to enriched 3'UTR HITS-CLIP peak sequences of day 20 upregulated DEGs in miNs
(A) *KALRN* contains one enriched AGO HITS-CLIP peak for miR-124-3p at 3'UTR highlighted in yellow.
(B) *BCL7A* 3'UTR contains two predicted miR-124-3p sites within the AGO HITS-CLIP peaks highlighted in yellow.
(C) *RCAN2* and *SEMA6A* 3'UTRs contain multiple miR-124-3p target sites within the AGO HITS-CLIP peaks highlighted in yellow.

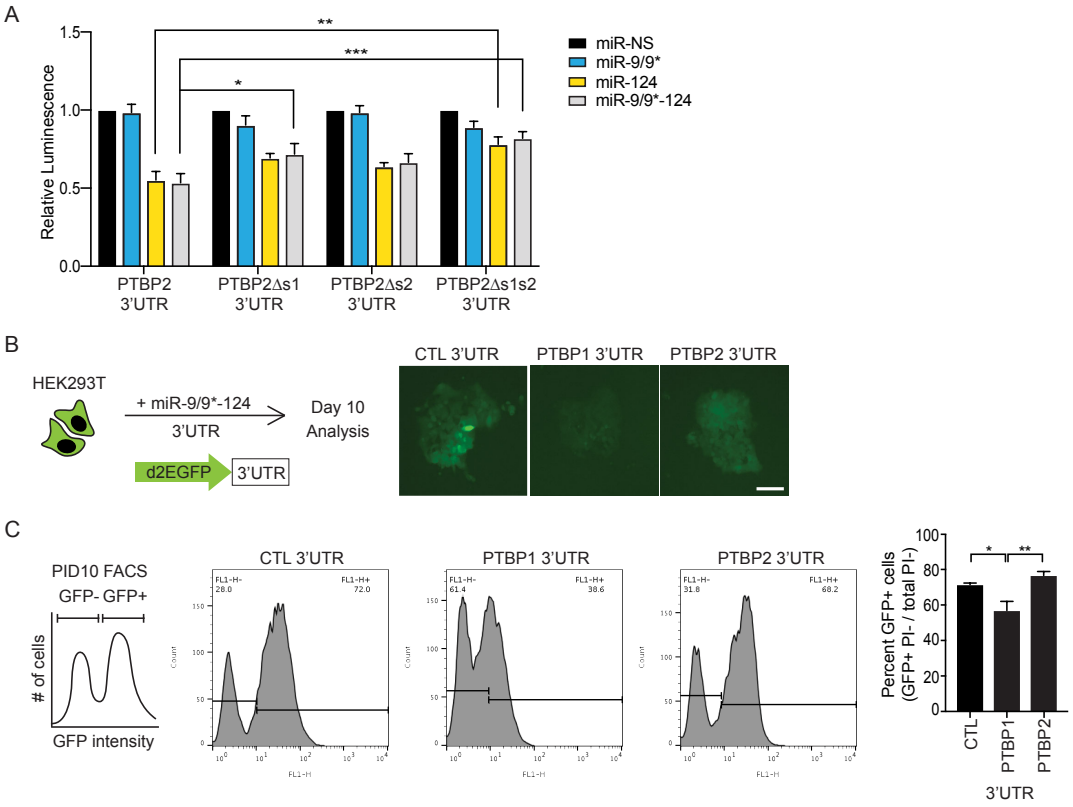

Figure S3. MiR-124 target site validation, and assessment of miR-124 promoting PTBP2 expression via targetting PTBP2 3'UTR with the prolonged neurogenic input.
(A) Luciferase assays in HEK293T cells of PTBP2 3'UTR with miR-124 site(s) mutagenized. Luminescence was measured 48 hrs after transfection and normalized to miR-NS control of each condition. Data are represented by mean ± SEM from four independent experiments. Two-way ANOVA followed by Dunnett's test (from left, miR-124 ** P = 0.001; miR-9/9*-124 * P = 0.0104, *** P = 0.0001).
(B) Left, a schematic diagram of the reporter construct and experiments. HEK293T cells were transduced with destabilized EGFP reporter to monitor the 3'UTR activity. Right, representative images of GFP fluorescence of HEK293T cells measured 10 days after miR-9/9*-124 transduction. Scale bar = 100 μm.
(C) Left, schematic of a histogram of flow cytometry analysis with gating of EGFP intensity to separate GFP-negative and GFP-positive cell populations at day 10. Middle, representative images of histograms following flow cytometry. Right, quantification flow cytometry to determine percent GFP-positive, PI-negative cells over the total PI-negative cells. Data represented in mean ± SEM from five independent experiments. One-way ANOVA followed by Tukey's test (from left, * P = 0.0222; ** P = 0.0031).

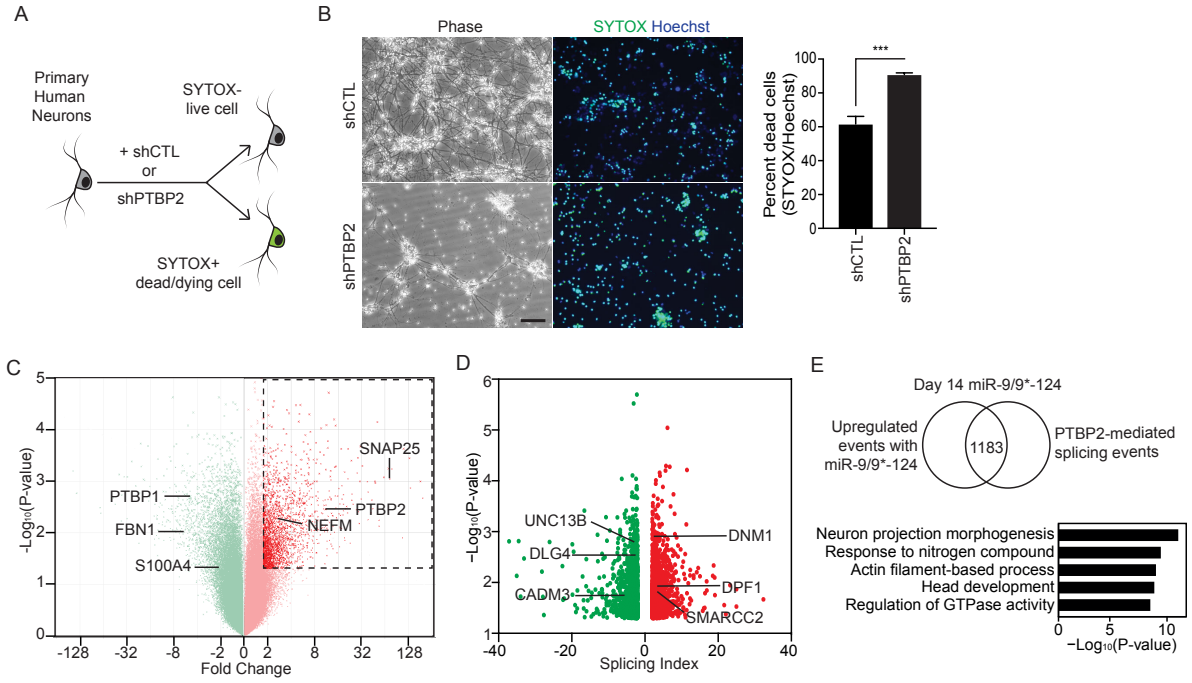

Figure S4. PTBP2 plays an essential role during miRNA-mediated neuronal conversion
(A) A schematic diagram of SYTOX assay. Knockdown of PTBP2 with shRNA in primary human neurons resulted in increased cell death measured by SYTOX after 10 days.
(B) Left, representative images of phase contrast and SYTOX staining 10 days after knockdown with CTL or PTBP2 shRNA. Right, quantification of SYTOX-positive cells over total Hoechst-positive cells. Scale bar = 75 μm. Data are represented by mean ± SEM. shGFP n = SYTOX 1237/2073; shPTBP2 n = 1589/1759 scored from independent fields of view. Unpaired t-test (*** P = < 0.0001).
(C) A volcano plot comparing gene expression between miR-9/9*-124 and miR-NS expression on day 14. Red dots within the enclosed box indicate differentially expressed genes (fold change ≥ 1.5, ANOVA p < 0.05) that are upregulated in miR-9/9*-124 condition. Examples of non-neuronal and neuronal genes are highlighted in green and red dots, respectively.
(D) A volcano plot of differentially spliced events (splicing index ≥ 2, ANOVA P < 0.05) at day 14 comparing shPTBP2 to shCTL in the miR-9/9*-124 expression background. Examples of spliced targets are highlighted with gene names corresponding to the differential splicing events.
(E) Top, target genes of interest were obtained by overlapping upregulated neuronal-associated events in (C) to all differentially spliced events by PTBP2 in (D). Bottom, top biological GO terms associated with the1183 unique events of genes upregulated during neuronal reprogramming and targetted by PTBP2.

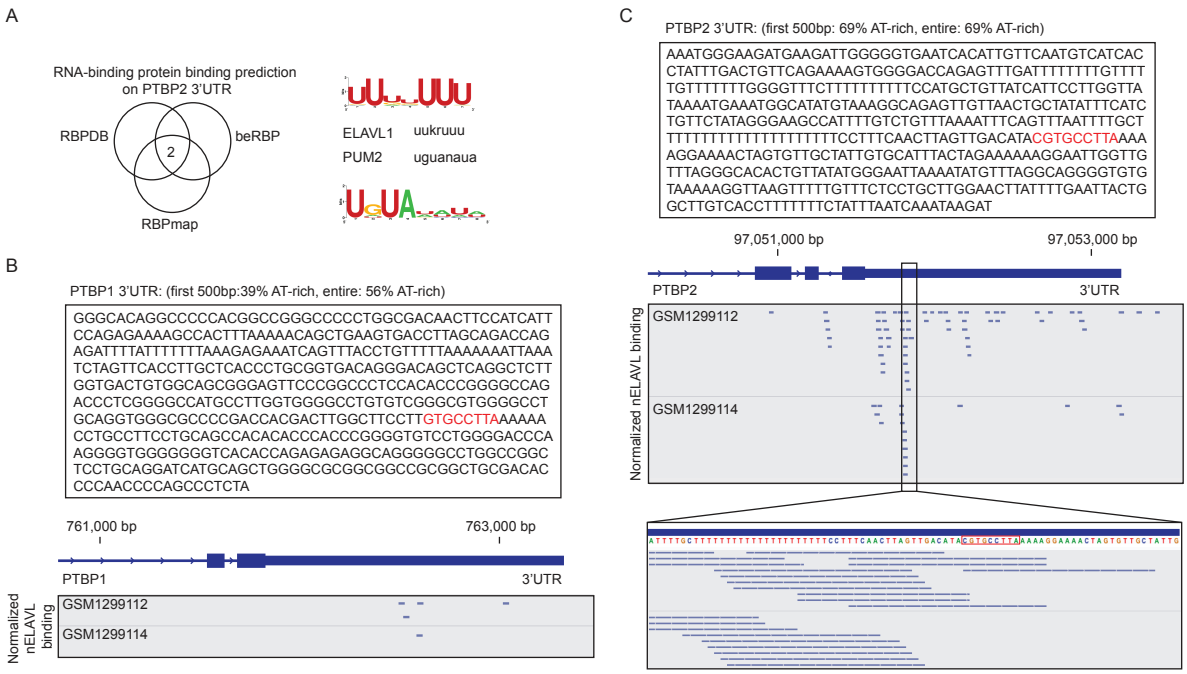

Figure S5. nELAVLs bind preferentially to PTBP2 and not PTBP1 3'UTR in the human brain
(A) Left, a Venn diagram overlapping all RNA-binding proteins predicted to bind to PTBP2 3'UTR using three different RNA-binding protein prediction databases. Right, binding motifs on PTBP2 3'UTR of the two predicted candidate RNA-binding proteins (left) based on all predicted motifs on PTBP2 3'UTR from RBPmap.
(B) Top, first 500 bp of PTBP1 3'UTR with the first conserved miR-124 target site in red. Bottom, track views of nELAVL HITS-CLIP of the human brain at PTBP1 3'UTR (GSM129912, GSM129914).
(C) Top, first 500 bp of PTBP2 3'UTR with the first conserved miR-124 target site in red. Bottom, track views of nELAVL HITS-CLIP of the human brain at PTBP2 3'UTR (GSM129912, GSM129914). The enclosed red box denotes the miR-124 target site.

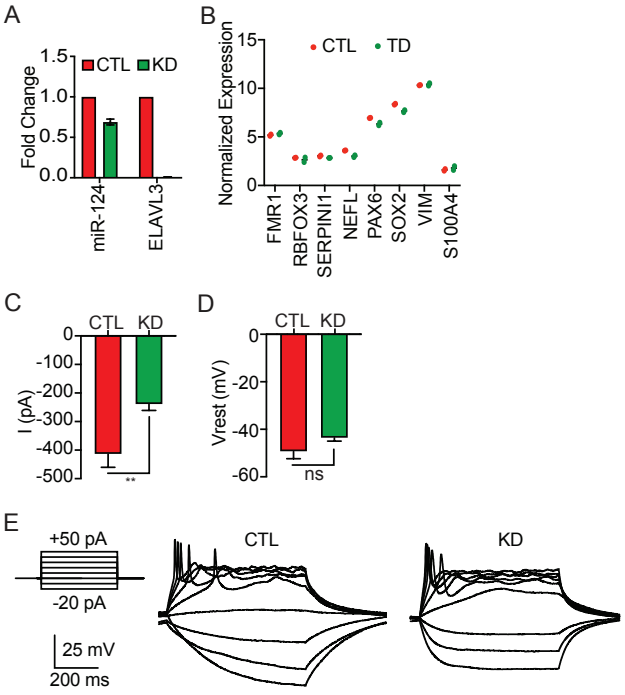

Figure S6. Neuronal long genes are targets of miR-124 and nELAVLs
(A) RT-qPCR for mature miR-124 expression and ELAVL3, showing reduced miR-124 and ELAVL3 expression upon KD treatment compared to CTL.
(B) Expression of genes associated with neuronal and neuronal progenitor identity in CTL and KD HNs.
(C) Peak inward sodium current amplitude of CTL and KD HNs. Data are represented in ± SEM from seven recorded cells from each condition. Two-tailed unpaired t-test (** P = 0.005).
(D) Resting membrane potential of CTL and KD HNs. Data are represented in ± SEM from seven recorded cells from each condition. Two-tailed unpaired t-test (ns P = 0.1191).
(E) Representative current-clamp traces of CTL and KD HNs.

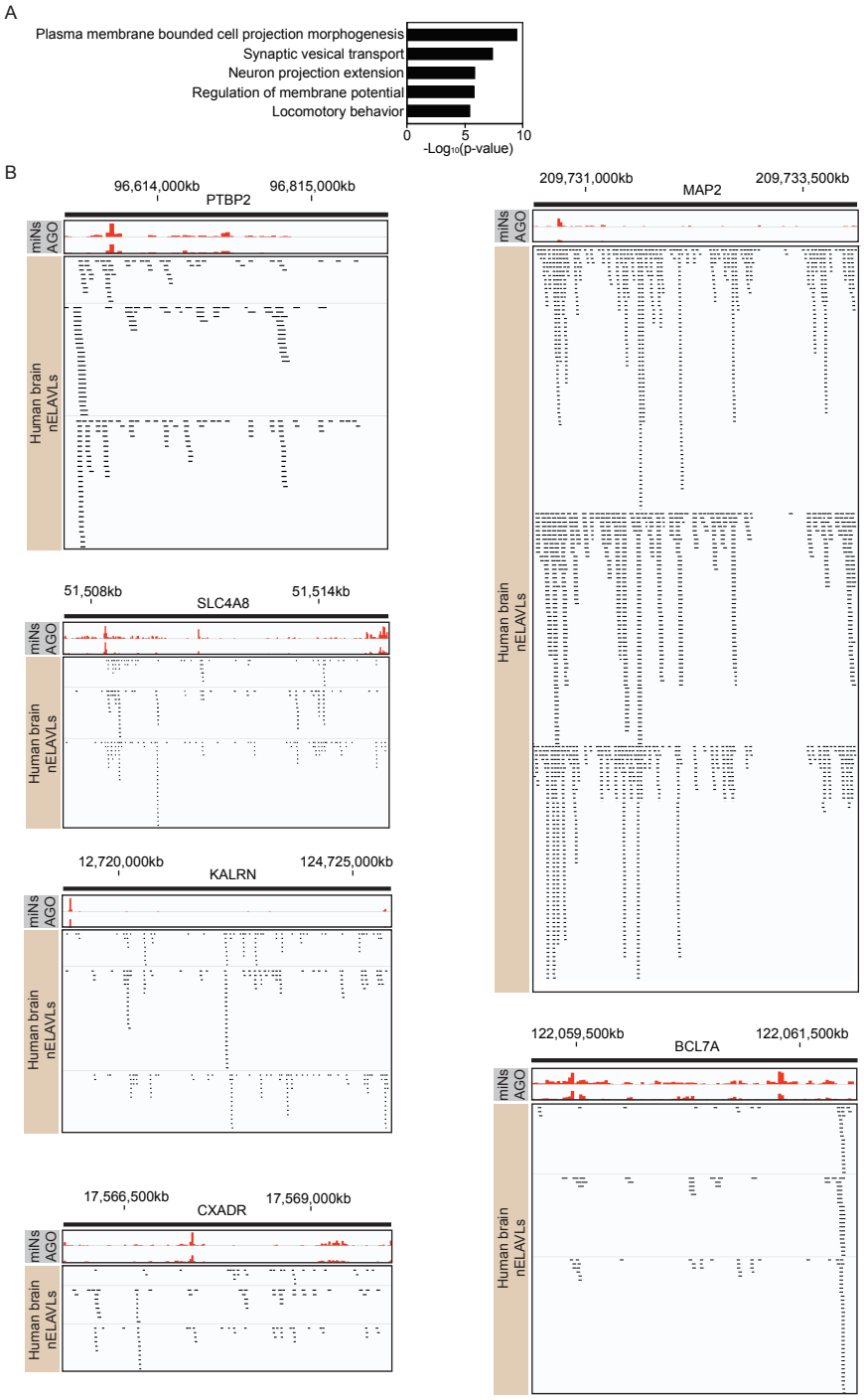

Figure S7. Identified neuronal transcripts that are bound by AGO and nELAVLs in HNs
(A) Top biological GO terms associated with the 77 genes that are predicted to be targeted by both AGO-miR-124 and ELAVL3, based on AGO HITS-CLIP in miNs, nELAVL HITS-CLIP in human brain, and HN RNA-seq with miR-124 and ELAVL3 knockdown.
(B) Track views of AGO HITS-CLIP in miNs and nELAVL HITS-CLIP in the human brain (GSM1299112, GSM1885137, GSM129911) of a select neuronal transcript 3'UTRs identified to be targets of AGO-miR-124 in miNs and HNs with nELAVL binding.

Gene name	logFC	adj.P.Val
ACAD10	2.69E-01	1.25E-03
ACER2	-6.41E-01	2.75E-06
ALAS1	4.42E-01	6.48E-08
ANGPTL1	2.62E-01	1.11E-04
ANK3	-1.06E+00	4.61E-12
APBA1	-3.58E-01	5.20E-03
APOE	3.11E-01	2.59E-04
ARHGAP20	-2.58E-01	1.14E-03
ARHGEF7	-2.45E-01	3.73E-04
ATP6V0A1	-3.55E-01	4.02E-06
ATP6V1G2	-7.71E-01	1.91E-11
BCL7A	-5.14E-01	2.80E-04
BDH2	2.56E-01	1.23E-04
BMF	-9.39E-01	6.06E-10
C14orf132	2.55E-01	8.72E-05
CAMK4	-9.30E-01	6.86E-10
CAMSAP1	-4.72E-01	1.66E-04
CDK15	-8.77E-01	3.34E-08
CDS1	-1.53E+00	4.75E-08
CDS2	-1.55E-01	6.90E-03
CEP85L	-5.40E-01	4.77E-09
CERS6	-3.93E-01	1.22E-04
CFI	1.73E-01	5.31E-03
CHRDL1	-3.77E-01	4.16E-03
CLCN4	-2.56E-01	1.76E-03
CLCN6	-6.20E-01	5.98E-10
CLDN11	4.59E-01	1.06E-07
CLUL1	-1.53E+00	4.41E-16
CNNM1	-8.45E-01	1.74E-05
CNTN1	-1.15E+00	2.06E-05
COX6C	4.76E-01	1.44E-08
CPE	2.48E-01	1.51E-03
CRY1	-8.57E-01	1.47E-09
CRY2	-6.05E-01	1.25E-07
CXADR	-1.06E+00	1.24E-10
DCLK1	-8.70E-01	4.73E-13
DHX30	-3.00E-01	8.47E-05
DKK2	-5.74E-01	1.69E-06
DNAJB5	-6.00E-01	2.77E-09
DOCK3	-4.80E-01	2.08E-04
DTNA	-3.15E-01	4.16E-05
DUSP26	-1.36E+00	3.71E-05
DUSP8	-1.98E+00	3.49E-07
EEF1A2	-1.95E+00	4.25E-08
EFR3B	-8.75E-01	6.22E-11
ENOX1	-7.19E-01	1.34E-03
EPB41	-3.94E-01	2.63E-03
EPHA4	2.73E-01	9.07E-04
FADS2	2.97E-01	2.50E-04
FAIM2	2.85E-01	8.55E-04
FAM110B	-2.19E-01	1.48E-03
FAM13C	-3.07E-01	4.61E-06
FAM184A	-8.65E-01	3.96E-06
FILIP1	-7.07E-01	3.53E-09
FKBP5	-3.28E-01	2.16E-03
FRMD4A	-4.16E-01	3.84E-05
FSD1L	-2.44E-01	9.50E-03
GABRE	-2.10E-01	1.21E-03
GAD1	-9.23E-01	4.01E-07
GDF11	-1.93E-01	9.47E-03
GDF5	-1.90E+00	1.49E-10
GPM6A	-8.05E-01	9.82E-03
GPNMB	1.55E-01	7.24E-03
GRIA2	-9.12E-01	1.05E-03
GRIA4	-1.44E+00	1.39E-04

Gene name	logFC	adj.P.Val
MDM1	-2.89E-01	1.26E-04
MFHAS1	-3.46E-01	4.90E-03
MGAT4C	-9.34E-01	1.15E-03
MITF	-3.52E-01	5.53E-03
MRPL35	2.00E-01	2.01E-03
MTHFR	-4.84E-01	2.25E-07
NEFM	-7.36E-01	3.27E-06
NINJ1	3.22E-01	1.49E-05
NLGN2	2.99E-01	8.63E-03
OGFRL1	-3.40E-01	7.90E-04
OSBPL1A	4.04E-01	2.55E-06
OXR1	-2.10E-01	5.70E-04
PASK	-7.59E-01	2.82E-03
PBX3	-9.96E-01	1.24E-09
PCDH7	4.33E-01	8.56E-06
PCLO	-1.42E+00	1.78E-04
PELP1	-4.45E-01	2.19E-03
PER3	-5.22E-01	8.66E-06
PFKM	4.86E-01	9.38E-10
PGM2L1	3.27E-01	2.03E-05
PHKA1	-4.32E-01	4.44E-04
PHLPP1	-3.60E-01	1.38E-03
PHYHIPL	-7.93E-01	1.30E-03
PLD6	-6.71E-01	1.74E-03
PNISR	-2.62E-01	1.39E-05
PPA2	2.47E-01	1.13E-04
PPM1D	-3.89E-01	1.96E-04
PPM1H	-9.24E-01	3.05E-11
PPP1R9A	-1.14E+00	2.39E-11
PTBP2	2.45E-01	2.20E-04
PTN	-8.37E-01	8.82E-11
RALGAPA1	-2.61E-01	4.19E-03
RALGPS1	-5.08E-01	1.06E-03
RANBP3L	-9.82E-01	8.23E-12
RAPGEF4	-1.70E+00	6.51E-09
RASL10B	-6.35E-01	8.25E-04
RCAN2	-7.31E-01	1.90E-12
RIC3	-1.50E+00	6.66E-08
RIMBP2	-1.19E+00	9.69E-05
RIMS2	-3.26E-01	2.58E-03
RNF157	-4.66E-01	6.72E-06
RNFT2	-8.03E-01	3.39E-11
RRAGD	-1.64E+00	7.49E-15
SAMD12	-1.21E+00	3.44E-09
SCARB1	4.19E-01	6.87E-03
SCN1A	-7.43E-01	8.57E-08
SCN2A	-2.24E-01	4.95E-03
SCN9A	-4.44E-01	4.53E-04
SDHA	4.27E-01	1.05E-08
SEMA6A	-1.15E+00	1.18E-09
SENP7	-2.45E-01	3.82E-03
SESN3	-3.27E-01	4.58E-04
SFMBT2	-9.75E-01	2.02E-03
SFRP4	4.41E-01	4.72E-06
SH3BP2	3.52E-01	2.16E-04
SLC12A7	-6.84E-01	7.60E-04
SLC25A11	2.73E-01	4.66E-05
SLC25A13	4.31E-01	1.64E-07
SLC2A8	-8.54E-01	2.39E-03
SLC4A8	3.30E-01	2.34E-04
SLC7A14	-3.73E-01	3.33E-05
SLITRK4	-6.47E-01	2.55E-03
SMARCB1	-4.41E-01	1.38E-04
SNAP25	-5.52E-01	5.29E-10
SPARCL1	-7.89E-01	1.32E-04

HMGCS1	-5.84E-01	3.64E-11
HTR2B	-6.42E-01	6.61E-03
IGF1	2.00E-01	1.21E-03
IGSF10	-4.78E-01	1.99E-04
INPP1	3.61E-01	7.75E-06
IRF6	-2.34E+00	3.13E-14
ITM2A	-5.17E-01	2.47E-03
KALRN	-2.41E-01	3.41E-03
KAT2B	-3.56E-01	3.43E-03
KCNK1	-6.44E-01	9.90E-03
KIAA1109	-3.48E-01	3.91E-05
KIAA1217	-4.34E-01	3.00E-06
KIF5A	-4.88E-01	3.85E-09
KIF5C	-9.14E-01	1.40E-11
KLLN	-4.85E-01	7.94E-04
KPNA5	-4.18E-01	8.78E-06
LCOR	-3.31E-01	3.87E-05
LDB2	-2.28E-01	5.54E-03
LDHB	4.57E-01	4.91E-09
LMBR1	3.07E-01	1.54E-03
LRRN3	-1.62E+00	1.43E-15
MAGI2	-7.78E-01	1.74E-09
MAMDC2	3.69E-01	5.44E-04
MAN1C1	-3.73E-01	2.77E-06
MANSC1	-3.27E-01	2.30E-03
MAP2	-2.94E-01	6.73E-05
MAP3K14	-3.27E-01	4.81E-03
MAPRE3	-5.43E-01	3.36E-04
MBP	-1.18E+00	5.45E-11
MCM3	-1.75E-01	9.94E-03
MCOLN1	-3.55E-01	1.23E-03

SPP1	-8.26E-01	3.11E-07
STAC2	4.69E-01	2.91E-03
STMN2	2.14E-01	3.39E-03
STRBP	-6.99E-01	4.99E-07
STX1B	-2.83E-01	6.24E-03
SULT1C4	-5.37E-01	1.42E-05
SV2A	1.74E-01	4.14E-03
SYBU	-7.80E-01	3.87E-09
TBC1D9	-3.30E-01	5.43E-03
THSD7A	-6.27E-01	2.14E-03
TKT	2.56E-01	4.20E-05
TLE1	-4.92E-01	1.57E-05
TM7SF3	2.20E-01	5.34E-03
TMEM63B	4.40E-01	9.37E-04
TMEM8B	-3.26E-01	5.29E-03
TMOD2	-4.14E-01	2.88E-06
TNFRSF14	-4.38E-01	4.31E-04
TNFRSF21	4.14E-01	3.92E-06
TRAPPC9	-3.39E-01	6.05E-03
TRPC3	-1.97E+00	1.84E-08
TSHZ1	-7.13E-01	5.06E-09
TSPAN14	2.02E-01	3.98E-03
TSPAN7	-1.55E+00	4.65E-04
TXLNB	-1.35E+00	3.82E-13
UPF3B	2.19E-01	8.66E-03
UQCRC1	3.26E-01	1.40E-06
WDR7	-3.75E-01	1.51E-05
ZNF518A	-3.87E-01	2.06E-04
ZNF577	-3.15E-01	8.04E-04
ZNF738	-2.97E-01	2.23E-03
ZSWIM7	-3.30E-01	1.35E-04

Table S1. MiR-124-responsive genes that harbor AGO-enriched peaks in miNs
List of upregulated genes during conversion harboring AGO-enriched peaks and are not upregulated upon miR-124 knockdown in miNs(TuD-miR-124 /TuD-miR-NS; $Log_2FC \geq -0.5$; adj. P.value > 0.01).

SEPT4	ANK1	ATP9A	CALR	CNTN1	DIP2B	FAIM2
AAK1	ANK2	ATPAF1	CAMK2D	COA5	DIS3L2	FAM102A
AASDHPPT	ANKRD20A11P	ATXN1	CAMK2N1	COL1A2	DJA2	FAM122C
AASS	ANKRD36C	ATXN10	CAMKK1	COL21A1	DJB6	FAM126B
ABCA1	ANKRD44	AVL9	CAMSAP1	COL24A1	DJC5	FAM135A
ABCA12	ANKRD46	AXIN2	CAMTA1	COL3A1	DJC6	FAM13B
ABCA7	ANO8	B3GAT3	CAPZB	COL4A5	DJC7	FAM13C
ABCB4	ANP32A	B3GLCT	CBX5	COL5A2	DKK3	FAM169A
ABCC6P1	ANXA11	B4GALT3	CCBE1	COLEC12	DLD	FAM196B
ABCC9	ANXA6	BAALC	CCDC136	COLGALT2	DLEU2	FAM198B
ABCD2	AP1B1	BAG6	CCDC149	COMMD2	DLG4	FAM20C
ABCD3	AP1M1	BAZ2B	CCDC64	COPG2	DLG5	FAM234B
ABCG4	AP1S2	BBS9	CCDC7	COX6C	DMPK	FAM49B
ABHD6	AP2S1	BCAS1	CCDC74A	CPEB3	DMXL2	FAM65B
ABLIM3	AP5M1	BCL7A	CD109	CPEB4	DNM1	FAM66E
ABR	APBB1	BCL9	CD14	CPQ	DNM3	FAM69B
ABTB1	APC	BDH2	CD36	CPSF6	DNPH1	FAM96A
AC083843.4	APCDD1	BEND5	CD74	CREB1	DOCK10	FAP
ACAD11	APLP2	BEND6	CDH18	CREM	DOCK4	FAR2
ACAD8	APOL4	BLID	CDH6	CRLS1	DOK5	FAR2P2
ACADM	APOO	BMP1	CDK14	CRMP1	DOT1L	FASTKD1
ACAN	APP	bP-21264C1.1	CDK15	CROT	DPF1	FAT4
ACAP3	AQP9	BRD3	CDK16	CS	DPP3	FBLN2
ACAT1	ARFGEF1	BRE	CDK18	CSRNP3	DPT	FBXL17
ACBD5	ARG2	BRI3BP	CDKL1	CTB-52I2.4	DPYSL2	FBXO9
ACER2	ARHGAP12	BRMS1L	CDS1	CTPS2	DPYSL4	FCMR
ACER3	ARHGAP20	BRWD3	CEACAM1	CTSO	DROSHA	FER
ACSF2	ARHGAP26	BTRC	CEMIP	CTSS	DST	FGD4
ACSL4	ARHGAP32	C10orf10	CENPW	CUL3	DT	FGD6
ACTR10	ARHGAP42	C11orf49	CEP85L	CXADR	DUSP23	FGF13
ACTR3B	ARHGEF10L	C12orf75	CFI	CXCL12	DUSP6	FH
ACVR1B	ARL5A	C14orf37	CH17-472G23.4	CYB5R4	dydorbo	FHOD3
ACVR2A	ARMC9	C15orf39	CHD4	CYFIP2	DYNC1I2	FIBIN
ACVR2B	ARRDC4	C15orf57	CHFR	CYGB	DYRK2	FILIP1
ADAM17	ARSF	C16orf45	CHI3L2	CYP3A4	EDIL3	FKBP2
ADAM19	ARV1	C18orf54	CHR3	CYP3A5	EDNRA	flawfybo
ADAM22	ASAH1	C1orf220	CHRM2	CYP3A7	EEF2K	FN3K
ADAM23	ASAP1	C1QTNF1	CHST10	CYP46A1	EEPD1	FNDC1
ADAMTS12	ASB9	C1QTNF6	CHST11	CYTH2	EFR3B	FNDC4
ADARB1	ATAD2B	C2orf27A	CIITA	DAAM2	EHBP1	FNDC5
ADCY1	ATAT1	C4A	CISH	DAB1	EIF5A2	FOXN3
ADD2	ATF6B	C4B	CIT	DAPK1	ELN	FRAS1
ADGRA3	ATF7IP	C4orf27	CKB	daseebo	EMCN	FRK
ADGRL1	ATG4D	C8orf34	CLASP2	DCBLD1	EML6	FRMD4A
ADGRL2	ATP13A2	C9orf3	CLCN4	DCLK1	EMP2	FRMD5
ADK	ATP1A3	CABLES1	CLEC16A	DCLK2	EN1	FAIM2
AES	ATP1B1	CABLES2	CLNS1A	DCTPP1	ENPP5	FAM102A
AF131217.1	ATP2B4	CABP2	CLSTN3	DCUN1D4	ENSA	FAM122C
AF186192.5	ATP5A1	CAC1A	CLTA	DDAH1	EPB41L1	FAM126B
AGAP1	ATP5B	CAC1G	CLTC	DDIT4L	EPB41L3	FAM135A
AGAP2	ATP5C1	CAC2D3	CLU	DDR1	EPHA4	FAM13B
AIFM1	ATP5G2	CACHD1	CLUH	DDT	EPHB2	FAM13C
AIG1	ATP5L	CACNB2	CLUL1	DDX39B	EPHX2	FAM169A
AK5	ATP6AP1	CACNB4	CLYBL	DGCR8	EPS15	FAM196B
ALAD2	ATP6V0A1	CACNG7	CNIH2	DHODH	ETS1	FAM198B
ALG9	ATP6V0E2	CADM1	CNIH3	DHX15	EVL	FAM20C
AMPD3	ATP6V1B2	CADM3	CNKSR2	DHX30	EXOC1	FAM234B
AMPH	ATP6V1C1	CALM1	CNOT8	DHX9	EXOC4	FAM49B
ANGEL2	ATP6V1G2-DDX39B	CALM3	CNTFR	DICER1	FABP3	FAM65B

FRMD5	HLF	KIF26B	MAP2	MYLK	NEFM	PCBP3
FRMPD3	HMG20A	KIF3B	MAP2K6	MYO1B	NEGR1	PCBP4
FRY	HMGB1	KIF3C	MAP3K12	MYO5A	NEK10	PCCA
FYB	HNRNPA3P3	KIF5C	MAP3K13	MYOZ2	NELFCD	PCCB
GAB1	HOMER1	KLC1	MAP4K3	NBEA	NET1	PCDHA9
GABRA3	HOXA10	KLF3	MAPK10	NBEAP1	NETO2	PCDHB16
GABRE	HOXA13	KLHL13	MAPRE2	NCALD	NEURL4	PCDHB18P
GABRR1	HR	KLRC4-KLRK1	MAPRE3	NCAM1	NFAT5	PCDHB8
GAD1	HRAT17	KMT5B	MAPT	NCOA1	NFYC	PCDHGC3
GALC	HSBP1	KP5	MATR3	NDN	NID2	PCMTD1
GALNT11	HSD17B4	LACC1	mawgar	NDRG1	NIPSP3A	PCSK5
GALNT14	HSP90B1	LACTB	MBOAT1	NDRG2	NKIRAS1	PCSK7
GALNT5	HSPA12A	LAMB1	MBTD1	NDRG4	NLGN4X	PCYOX1L
GAS1RR	HSPB7	LARGE	MCC	NDUFAF5	NLK	PDCL
GAS7	HTT	LBH	MCM4	NDUFS1	NNT	PDE1A
GBP2	HUNK	LCN	MCOLN3	NDUFS2	NOL4L	PDE3A
GDF11	INA	LEPR	MCTP1	NDUFV2	NOMO3	PDE4B
GGCT	IAH1	LGALSL	MDH1B	NECAB3	NONO	PDGFD
GIPC1	IBTK	LIMCH1	ME3	NEFL	NPNT	PDGFRA
GLI3	IDH2	LINC00673	MEG3	NEFM	NRCAM	PDK1
GLUL	IGFBP2	LINC00702	MEGF8	NEGR1	NREP	PDP1
GNB5	IGFBP3	LINC00886	MEIS3	NEK10	NRG1	PDS5B
GNG2	IGFL4	LINC01091	MEMO1	NELFCD	NRP1	PDZRN3
GP1BB	IGK	LINC01535	MEST	NET1	NSF	PELI2
GPAA1	IGSF10	LINC01621	MET	NETO2	NSFP1	PFKM
GPCPD1	IKZF2	LLGL1	METTL9	NEURL4	NSG1	PFN2
GPI	IL17RB	LMBR1	MFAP2	NFAT5	NSL1	PGD
GPM6B	IL17RD	LMBR1L	MGAT5	NFYC	NSMF	PGM2L1
GPR155	IL6R	LMO7	MGP	NID2	NT5C2	PHACTR1
GPR162	IL7	LOC100507002	MGST3	NIPSP3A	NT5C3A	PHACTR3
GPR173	IMMT	LOC101927686	MICAL2	NKIRAS1	NT5DC1	PHKA1
GPR75-ASB3	INPP4B	LOC101929710	MICU1	NLGN4X	NTN4	PHYHIPL
GPRC5B	INPP5A	LOC102723373	MICU3	NLK	NTNG1	PI4KA
GRAMD1B	INSRR	LOC102723769	MID1	NNT	NTRK1	PI4KAP1
GRAMD4	IQCJ	LOC105378663	MINOS1P1	NOL4L	NTRK3	PI4KAP2
GREM1	ITGA11	LOC220729	MIR22HG	NOMO3	NUAK1	PIAS4
GS	ITGA2	LOC645513	MIR29A	NONO	NUDCD3	PIK3CB
GSR	ITGA5	LOC728730	MIR4500HG	NPNT	NUDT22	PIK3R1
GSTM2	ITGAV	LPAR6	MIR573	NRCAM	NUDT3	PIK3R2
GTF2I	ITM2A	LPCAT1	MIR99AHG	NREP	OBSCN	PIK3R3
GTF2IP1	ITSN1	LPP-AS2	MLIP	MYLK	OGDH	PIN1
GTF3C1	JARID2	LRP4	MLLT11	MYO1B	OGFRL1	PIP4K2A
GTF3C2	JPH2	LRP5	MMD	MYO5A	OIP5-AS1	PIP5K1C
GUCY1B3	KALRN	LRRC32	MMP16	MYOZ2	ORMDL3	PITPNM1
GULP1	KCB2	LRRC40	MOB4	NBEA	OSBP2	PKIA
GXYLT2	KCNC4	LRRC49	moymoyby	NBEAP1	OSBPL1A	PKIG
H2AFY	KCNH5	LRRK2	MPC1	NCALD	OSCP1	PKM
H2AFY2	KCNK2	LSAMP	MREG	NCAM1	OSR1	PLA2G15
H3F3B	KCNMA1	LUCAT1	MROH7	NCOA1	OXTR	PLA2G4A
HABP4	KDM4C	LYNX1	MRPL35	NDN	P1L5	PLAGL1
HAGH	KDM5B	LYST	MRPS7	NDRG1	P4HTM	PLCB1
HDAC5	KHDRBS1	maby	MSI1	NDRG2	PAFAH1B2	PLCB4
HDAC9	KIAA0391	MAFB	MT1F	NDRG4	PAK1	PLCD4
HECW1	KIAA0895L	MAGI1	MTMR1	NDUFAF5	PANK1	PLCH1
HEPH	KIAA0922	MAGI3	MTMR9	NDUFS1	PARM1	PLD1
HIST4H4	KIAA1109	MAMDC2	MTSS1L	NDUFS2	PARP8	PLEKHA2
HK1	KIAA1644	MAN1C1	MTUS1	NDUFV2	PB	PLEKHA5
HK2	KIF1B	MAOA	MXRA5	NECAB3	PBX1	PLIN2
HLA-DRA	KIF21A	MAP1B	MYH10	NEFL	PBX3	PLK2
PLPPR4	RALGAPA1	SCP2	SLC9B2	SVILP1	TP53I11	WARS2-IT1
PLS3	RALGAPA2	SCRG1	SLIT2	SYNE1	TP53I3	WASF3
pluspar	RALGDS	SDCCAG8	SMAD1	SYNGR3	TP63	WBP2

PLXDC1	RALGPS1	SDHA	SMARCA2	SYNJ1	TPCN1	WDR37
PLXDC2	RANBP3L	SDHAP3	SMARCA4	SYNJ2	TPD52L1	WDR41
PLXNC1	RAP1GAP2	SDK2	SMARCC2	SYNPO2	TRAK1	WDR63
PLXND1	RASA3	SEC14L1	SMG6	SYPL2	TRAPPC2	WDR7
PMAIP1	RASGRP3	SEC61A2	SMIM10L2A	SYT1	TRDMT1	weewerby
POLR2E	RASL10B	SECTM1	SNN	T14	TRERF1	WHSC1
POLR3A	RBM12B	SEMA3D	SNRPA	TADA2A	TRIB1	WWP2
POLR3F	RBM24	SEMA6B	SNRPA1	TANC1	TRIM16L	XPNPEP1
POMGNT1	RBMX	SEMA6D	SOCS2	TAPT1	TRIM2	YAF2
POMK	RERE	SENP7	SOCS2-AS1	TBC1D12	TRIM24	yara
POR	REREP3	SEPN1	SOGA3	TBC1D8	TRMT2B	YLPM1
POSTN	REV3L	SEPT7P2	SORBS1	TBCB	TRPC3	YPEL3
PPARD	RFTN1	SEPW1	SORL1	TBCK	TSPAN13	YWHAE
PPARGC1A	RGL1	SERPINF1	SOX4	TCIRG1	TSPAN15	ZC2HC1A
PPFIA4	RGS16	SERPINI1	SPAG17	TCN2	TSPAN18	ZC3H12B
PPIA	RGS3	SETBP1	SPARC	TCONS_l2_00002184	TSPAN3	ZCCHC2
PPIAL4C	RGS4	SFRP4	SPARCL1	TCONS_l2_00026703	TSPAN5	ZDHHC13
PPP1R12B	RGS8	SGIP1	SPATA13	TCONS_l2_00030954	TSPAN7	ZDHHC15
PPP1R14B	RHOBTB1	SH3BP2	SPATA20	TDO2	TSSC1	ZDHHC16
PPP1R21	RIMS2	SH3BP5	SPATA6	TENM4	TTC13	ZDHHC9
PPP2R1B	RIT1	SH3GLB2	SPC3	TFAM	TTC19	ZEB1-AS1
PPP2R2B	RMDN2	SHOX2	SPIDR	TGFBI	TTC33	ZFAND5
PPP2R2D	RNF150	SHTN1	SPOCK1	TGM2	TTLL6	ZFAND6
PPP2R3A	RNF38	SIAE	SPRY1	THRA	TTYH3	ZFHX4
PPP5C	RNFT2	SIPA1L3	SPRYD3	THRB	TUBA4A	ZFP14
PQLC2L	ROR1	SIRPA	SPSB1	THSD7A	TUBB3	ZFP30
PREP	RP11-353N14.1	SIRT2	SPTLC3	TIAF1	TUBG2	ZMIZ1
PREX1	RP11-359M6.1	SIX1	SRD5A1	TIMM8B	TXNRD2	ZMYND8
PREX2	RP11-368L12.1	SLAIN1	SRGAP2	TIPARP	UACA	ZNF124
PRH1	RP11-395N3.2	SLC16A3	SRSF1	TKT	UBA5	ZNF195
PRICKLE1	RP11-402L1.11	SLC16A4	SRSF3	TLE3	UBE2N	ZNF24
PRIM2	RP11-417J8.3	SLC16A7	SSBP3	TLN2	UBP1	ZNF254
PRKAA2	RP11-435B5.5	SLC1A2	ST3GAL3	TLR1	UBR7	ZNF33A
PRKCA	RP11-442J21.2	SLC22A17	ST3GAL5	TLR4	UNC13B	ZNF347
PRKCQ-AS1	RP11-575F12.3	SLC22A23	ST3GAL6	TMCC1	UPRT	ZNF385D
PRKG1	RP11-61O11.1	SLC22A3	ST6GALC6	TMEM108	UQCRB	ZNF430
PRKG2	RP11-782C8.2	SLC25A12	ST8SIA4	TMEM120A	UQCRC1	ZNF436
PRLR	RP11-88I18.2	SLC25A13	STAC2	TMEM132A	UQCRH	ZNF444
PROS2P	RP4-665J23.1	SLC25A23	STAU2	TMEM136	UROS	ZNF454
PRSS12	RP5-1172A22.1	SLC25A27	STK32B	TMEM161B	USP11	ZNF493
PRTFDC1	RPS6KA3	SLC25A29	STK33	TMEM173	USP33	ZNF506
PRUNE2	RPS6KA6	SLC25A5	STMN1	TMEM178A	USP46	ZNF540
PSD3	RPUSD3	SLC2A5	STMN2	TMEM2	UTRN	ZNF608
PSMB8-AS1	RRAGD	SLC35B4	STON2	TMEM25	V1	ZNF609
PTBP2	RSRC1	SLC38A1	STX12	TMEM50B	V3	ZNF618
PTGDS	RUFY3	SLC38A2	STX1B	TMEM59L	VAMP4	ZNF676
PTGFR	RUNX1T1	SLC38A7	STX7	TMEM63B	VAV3	ZNF680
PTPN13	S1PR1	SLC39A10	STXBP1	TMEM8A	VCAM1	ZNF708
PURG	SACS	SLC4A2	STXBP5	TMOD2	VDAC1	ZNF709
PXYLP1	SAMD14	SLC4A4	SUB1	TMOD3	VEZT	ZNF718
PYGB	SARDH	SLC4A7	SUCLA2	TMTC2	VNN1	ZNF75D
RAB13	SBF2	SLC6A17	SULF2	TMTC4	VOPP1	ZNF85
RAB26	SCG5	SLC6A8	SUMO2P18	TNFRSF19	VPS13C	ZNRF2
RAB3A	SCML1	SLC7A6	SUN1	TNIK	VPS36	ZYG11B
RAB3C	SCN1A	SLC8A1	SUSD4	TNRC6B	VSNL1	
rahiyu	SCN1B	SLC9A9	SVIL	TNS3	vubler	

Table S2. Neuronal genes with PTBP2-mediated splicing events
List of neuronal genes (upregulated in miNs / HAFs; FC ≥ 1.5; ANOVA P < 0.05) exhibiting splicing events associated with PTBP2 during reprogramming (shPTBP2 / shCTL; splicing index ≥ 2; ANOVA P < 0.05).

Gene name	logFC	Adj.P.Val
ABCD2	-1.83E+00	9.79E-03
ADAM22	-1.65E+00	9.21E-04
ADAM23	-1.25E+00	1.76E-02
ADCY1	-2.44E+00	5.06E-05
AMOT	-1.20E+00	2.04E-02
ANK3	-1.07E+00	7.83E-03
ANKRD6	-2.24E+00	1.15E-05
APBA1	-1.71E+00	3.05E-04
APBB1	-1.35E+00	1.87E-03
APOE	-1.87E+00	3.09E-04
ARHGEF7	-1.03E+00	3.36E-03
ASTN1	-1.64E+00	3.52E-04
ATP6V1G2	-1.33E+00	2.66E-02
BAALC	-2.20E+00	3.83E-05
BCL7A	-1.24E+00	1.66E-03
C14orf132	-2.08E+00	4.63E-05
CALB2	-3.41E+00	7.54E-05
CAMK4	-1.05E+00	2.17E-02
CAMSAP1	-1.28E+00	2.73E-03
CDC7	-1.98E+00	1.97E-03
CERS6	-2.50E+00	6.64E-05
CHRDL1	-2.53E+00	1.88E-05
CKB	-1.40E+00	2.44E-03
CLCN4	-1.32E+00	5.14E-03
CNTFR	-1.23E+00	2.41E-02
CNTN1	-1.81E+00	9.97E-03
CPE	-1.29E+00	2.47E-03
CRISPLD1	-2.00E+00	3.63E-04
CRMP1	-2.33E+00	1.23E-04
CRY1	-1.30E+00	1.28E-03
CSRNP3	-1.57E+00	1.22E-02
CXADR	-1.62E+00	2.73E-02
CYFIP2	-1.14E+00	6.06E-03
DCLK1	-2.28E+00	4.58E-05
DCLK2	-2.34E+00	7.21E-06
DPF1	-2.38E+00	8.68E-05
EFR3B	-1.24E+00	5.25E-03
ENOX1	-1.85E+00	5.62E-03
FADS2	-1.73E+00	4.46E-04
FAM110B	-1.36E+00	7.31E-04
FAM131B	-1.31E+00	1.75E-03
FAT3	-1.51E+00	9.85E-04
FGD4	-1.51E+00	8.35E-03
FOXP2	-2.99E+00	3.85E-02
FRY	-1.86E+00	5.51E-05
FZD3	-1.45E+00	2.68E-02
GAD1	-1.28E+00	7.76E-04
GDAP1	-1.34E+00	7.20E-03
GPC2	-1.86E+00	1.37E-04
GPD1L	-2.63E+00	4.06E-04
GPM6A	-2.35E+00	3.96E-04
GPR173	-1.19E+00	1.81E-02
GRIA2	-1.74E+00	2.32E-03
GRIA4	-1.33E+00	6.84E-03
GRM5	-2.06E+00	3.30E-02
GUCY1A2	-1.54E+00	1.75E-02
HMGCS1	-2.22E+00	6.55E-03
IL17RD	-2.54E+00	9.18E-06
JPH4	-1.31E+00	6.71E-03
KALRN	-1.45E+00	4.23E-04
KCTD12	-2.29E+00	1.44E-04
KIAA0513	-1.34E+00	1.41E-03
KIF5C	-1.34E+00	4.06E-03
KLHL25	-1.32E+00	1.78E-03
LRRC4	-1.37E+00	4.46E-03
MAGI3	-1.48E+00	3.88E-04
MAP2	-1.79E+00	5.20E-04
MCM3	-1.40E+00	3.98E-04
METTL7A	-1.80E+00	5.74E-05
MGAT4C	-2.81E+00	5.42E-03
NCALD	-2.21E+00	3.83E-05
NCAM1	-1.66E+00	8.27E-04
NELL2	-2.45E+00	2.15E-05
NFIB	-1.33E+00	3.05E-03
OGFRL1	-2.46E+00	2.85E-05
P2RY1	-2.81E+00	1.78E-03
PASK	-1.53E+00	4.18E-02
PEG10	-3.04E+00	2.97E-06
PHYHIPL	-2.49E+00	9.40E-05
PLCXD2	-2.58E+00	1.68E-04
PODXL2	-1.18E+00	7.68E-03
PPM1L	-1.60E+00	2.84E-04
PPP1R12B	-1.76E+00	5.18E-05
PRRT2	-2.31E+00	7.95E-05
PTBP2	-1.70E+00	3.41E-02
PTCHD1	-1.34E+00	4.35E-02
RAB3A	-2.17E+00	1.87E-04
RALGPS1	-2.01E+00	2.87E-05
RIMS3	-1.61E+00	3.27E-04
RIMS4	-1.85E+00	5.99E-04
RNF144A	-1.18E+00	3.01E-03
RNF157	-1.38E+00	1.33E-03
RNFT2	-1.37E+00	4.52E-04
RRAGD	-1.05E+00	2.73E-02
RUFY3	-1.98E+00	1.46E-03
SBK1	-1.75E+00	3.09E-03
SCD5	-1.08E+00	3.36E-03
SCN1A	-3.60E+00	1.65E-05
SEMA6A	-1.29E+00	1.66E-03
SERTAD4	-2.34E+00	1.04E-02
SESN3	-3.07E+00	1.32E-03
SFRP4	-3.54E+00	1.99E-02
SH3BP2	-1.28E+00	1.50E-03
SHF	-2.00E+00	4.03E-04
SIAH3	-2.40E+00	4.45E-04
SLAIN1	-2.35E+00	4.30E-05
SLC1A2	-2.34E+00	1.89E-04
SLC4A8	-1.07E+00	3.90E-03
SMAP1	-1.01E+00	1.27E-02
SNAP25	-1.29E+00	2.67E-03
SNCAIP	-3.29E+00	9.75E-07
SPARCL1	-1.35E+00	1.21E-02
SPTBN2	-1.14E+00	6.80E-03
SRGAP3	-1.01E+00	1.13E-02
STMN2	-3.04E+00	1.01E-05
STMN3	-2.03E+00	1.84E-04
STRBP	-1.40E+00	3.94E-03
SYBU	-2.25E+00	5.04E-05
SYT1	-1.25E+00	8.81E-03
THRA	-1.09E+00	8.51E-03
THSD7A	-1.32E+00	3.91E-03
TMEM108	-1.26E+00	6.35E-03
TMOD2	-1.76E+00	1.57E-03
TMTC2	-1.29E+00	1.11E-03
TNFRSF21	-1.07E+00	2.03E-02
TSPAN14	-1.11E+00	5.54E-03
TSPAN5	-1.34E+00	1.07E-03
TSPAN7	-2.67E+00	8.68E-06
TUB	-1.31E+00	8.61E-04
TUBB3	-2.41E+00	1.08E-04
ZNF300	-1.49E+00	6.27E-03
ZNF536	-1.16E+00	1.39E-02

Table S3. MiR-124-responsive genes that harbor AGO-enriched peaks in HNs
List of downregulated DEGs (KD / CTL; $Log_2FC \geq 1$; adj. P.value > 0.05) in HNs with miR-124 and ELAVL3 knockdown that harbor AGO-enriched peaks determined by HITS-CLIP in miNs

ABCD2	PHYHIPL
ADAM22	PLCXD2
ADAM23	PPM1L
ADCY1	PPP1R12B
ANK3	PTBP2
APBA1	RALGPS1
ARHGEF7	RIMS3
ASTN1	RNF144A
BAALC	RUFY3
BCL7A	SCD5
CAMSAP1	SCN1A
CLCN4	SEMA6A
CNTN1	SESN3
CPE	SLAIN1
CXADR	SLC1A2
CYFIP2	SLC4A8
DCLK1	SMAP1
DCLK2	SNAP25
EFR3B	SPARCL1
ENOX1	SRGAP3
FAM110B	STRBP
FAM131B	SYT1
FAT3	TMEM108
FGD4	TMTC2
FRY	TNFRSF21
FZD3	TSPAN5
GDAP1	TSPAN7
GPD1L	TUB
GPM6A	ZNF536
GRIA2	
GRIA4	
GRM5	
GUCY1A2	
HMGCS1	
JPH4	
KALRN	
KCTD12	
KIAA0513	
KIF5C	
MAGI3	
MAP2	
METTL7A	
MGAT4C	
NCALD	
NCAM1	
NELL2	
NFIB	
PEG10	

Table S4. MiR-124-responsive genes predicted to be bound by nELAVLs in HNs
List of miR-124-responsive genes predicted to be bound by nELAVLs (Scheckel et al., 2016) in HNs.

Chapter 4: PTBP2-mediated alternative splicing of DPF1

PTBP2 targets chromatin modifiers to facilitate histone mark recognition

A significant subset of the identified PTBP2 targets during neuronal reprogramming was chromatin regulators (Chapter 3), suggesting the role of PTBP2 in regulating epigenetic effectors during neuronal fate acquisition. One of the identified targets in the array was *DPF1* (Chapter 3). DPF1 (also known as BAF45B) is a subunit of the BAF chromatin remodeling complex that is specifically expressed in neurons and define the neuron specific-assembly of BAF complexes along with BAF45C and BAF53B (Lee et al., 2018; Lessard et al., 2007; Wu et al., 2007) (Figure 1A). We found that PTBP2 mediates the exclusion of a 30 base pair sequence in *DPF1* transcript, which is confirmed by RT-PCR using primers that flank the target spliced exon to generate amplicons corresponding to 216 bp (*DPF1-Long*/*DPF1-L*) and 186 bp (*DPF1-Short*/*DPF1-S*) in length (Figure 1B-C). In our reprogrammed neurons or miNs, the shorter isoform *DPF1-S* transcript is the primary isoform, which shifts to include more of the *DPF1-L* isoform after PTBP2 knockdown (Figure 1B). While both *DPF1-L* and *DPF1-S* isoforms are detected in the human brain (Figure 1D), spike-in sequencing of *DPF1* transcripts from human primary neurons indicated that majority of the *DPF1* population 79.4%, maps to *DPF1-S* while 20.6% maps to *DPF1-L* (Figure 7E). This miN-enriched *DPF1-S* appears to be a neuronal-enriched isoform as in the human cerebral cortex (Figure 1D) (Uhlen et al., 2015).

The 30 bp difference between *DPF1-S* and *DPF1-L* falls within the second functional plant homeodomain (PHD) (Figure 1F). We examined the functional implications of having different PHD lengths. First, we found that both isoforms could still interact with BRG1, the core ATPase subunit of the BAF complex (Figures 1G). We then asked if either isoform would

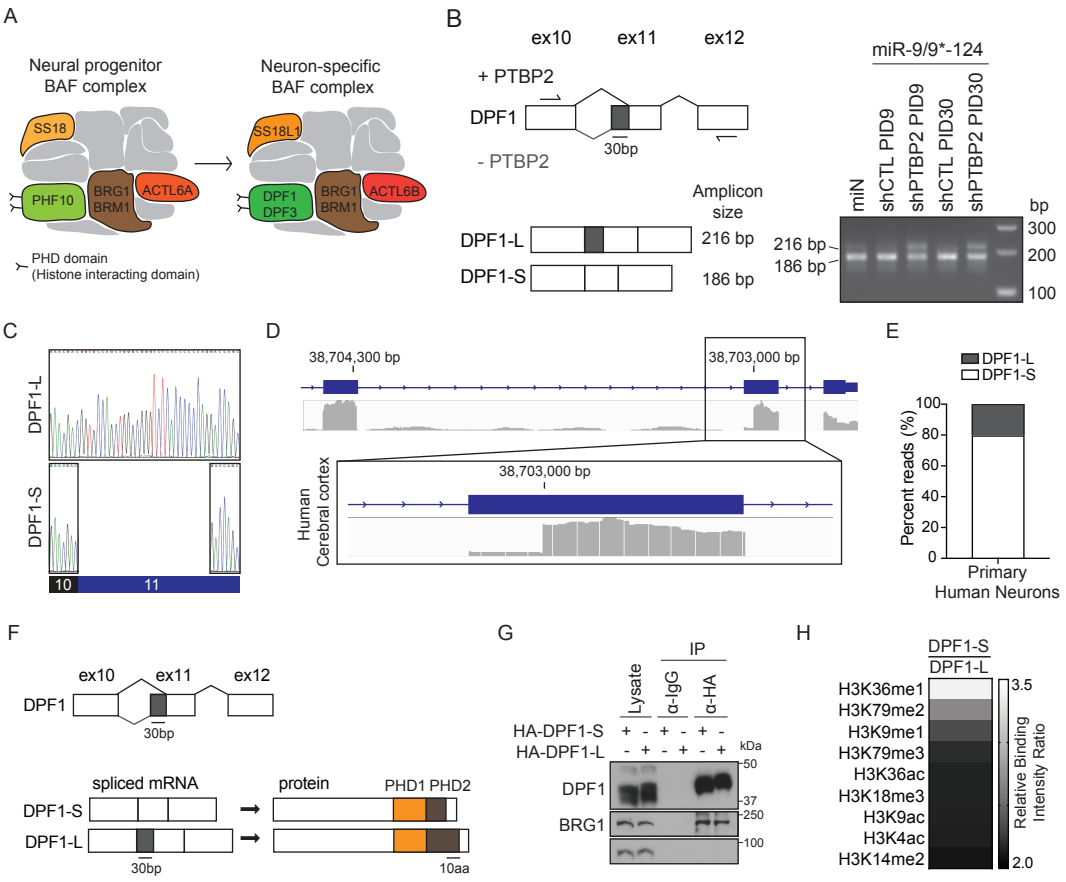

Figure 1. Spliced DPF1 isoforms in human neurons differed in PHD domain length
(A) Schematic representing the switching of homologous subunits within the chromatin remodeling BAF (BRG1/BRM-associated factor) complex during neurogenesis. ACTL6A, SS18,
and PHF10 of the neural progenitor BAF complex switches to ACTL6B, SS18L1, and DPF1/DPF3, respectively, for the neuron-specific BAF complex.
(B) Left, schematic of primers used to confirm DPF1 splicing event from the array to generate amplicons of 216 bp and 186 bp corresponding to DPF1-L and DPF1-S, respectively. Right, RT- PCR of DPF1 splicing events in different backgrounds.
(C) Chromatograms showing Sanger sequencing results from 2 clones with (DPF1-L) or without (DPF1-S) the 30 bp spliced sequence from human brain cDNA library.
(D) Track view of DPF1 from the human cerebral cortex (ERX288614) (adapted from Uhlen et al., 2015) showing two DPF1 isoforms with the shorter isoform (DPF1-S) being more dominant in the brain.
(E) Spike-in sequencing of primary human neuron cDNA to determine the percentage of DPF1- S (79.4%) and DPF1-L (20.6%) isoforms from total reads.
(F) Diagram of DPF1 splicing pattern with alternative 3' splice site for exon 11 generating two spliced DFP1 mRNAs, DPF1-S and DPF1-L, corresponding to differences in PHD2 domain length.
(G) Co-IP analysis revealed that both DPF1 isoforms could interact and incorporate into BRG1/BAF complex.

interact preferentially to different histone H3 marks as previous studies indicated the ability of proteins with PHD fingers to interact with histone H3 modifications (Huber et al., 2017; Lange et al., 2008; Sanchez and Zhou, 2011). Using histone H3 peptide array ELISA, we compared the ratio of binding intensity between DPF1-S and DPF1-L. We found that DPF1-S was able to bind nine H3 modifications much more robustly than DPF1-L (≥ 2 fold difference), including H3K9ac, H3K79me2, and H3K9me1 (Figure 1H). These results suggest that DPF1-S may likely be involved in the enhancement of BAF complex activity to recognize specific histone marks.

PTBP2 is crucial for neuronal conversion

Reducing PTBP2 expression led to the increased appearance of *DPF1-L* (Figure 1B) confirming that PTB switching in neurons is critical to confer the alternative splicing of *DPF1* to *DPF1-S* isoform. Our results thus demonstrate the significance of PTBP2 function in executing the proper processing of neuronal genes activated in response to miR-9/9*-124 while the loss of PTBP2 would block neuronal conversion (Chapter 3; Figure 2A). Contrastingly, sequential knockdown of PTBP1 and PTBP2 proteins have been shown to be able to reprogram human fibroblasts into neurons (Xue et al., 2016). However, comparing the conversion efficiency by miR-9/9*-124 and PTBP1/2 sequential knockdowns points to the limited efficacy with PTB knockdowns only (Figure 2B-C). This difference is likely due to the presence of neurogenic factors such as nELAVLs (Chapter 3) and/or other neuronal RBPs evoked by miR-9/9*-124 ensuring robust PTBP2 expression and activation of the neuronal program (Chapter 3), including the proper splicing of DPF3.

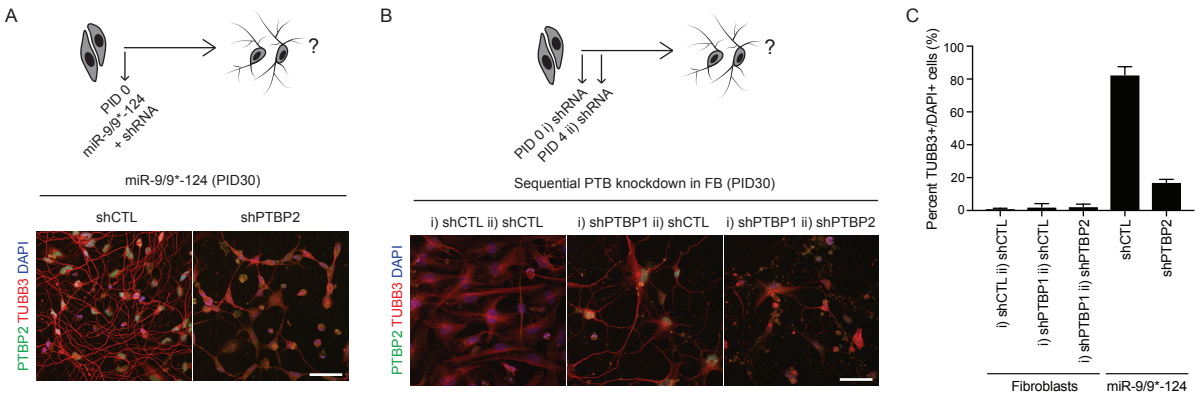

Figure 2. PTBP2 is crucial for neuronal conversion
(A) Top, schematic of miRNA-mediated reprogramming paradigm in which both miR-9/9*-124 and shRNA against PTBP2 were transduced together at PID 0. Bottom, PID 30 miNs with CTL or PTBP2 knockdown immunostained with PTBP2 and TUBB3. Scale bar = 50 μm.
(B) Top, schematic of sequential reprogramming. The first shRNA was transduced at PID 0 followed by a second shRNA transduced at PID 4 or 4 days after the first shRNA transduction. Bottom, PID 30 cells after sequential knockdown using shRNAs against CTL, PTBP1, and/or PTBP2 immunostained with PTBP2 and TUBB3. Scale bar = 50 μm.
(C) Quantification of TUBB3-positive cells over DAPI-positive cells with two or more processes in (A) and (B). Data represented as mean ± SEM. i) shCTL ii) shCTL n = TUBB3 2/293; i) shPTBP1 ii) shCTL n = TUBB3 1/67; i) shPTBP1 ii) shPTBP2 n = TUBB3 2/54; miR-9/9*-124 shCTL n = TUBB3 383/464; miR-9/9*-124 shPTBP2 n = TUBB3 112/635 scored from independent fields of view.

Chapter 5: Conclusions

In this thesis, we uncovered the role of miR-124 in the upregulation of genes associated with neuronal differentiation and function during the neuronal conversion of human fibroblasts. This finding provides insights into the function of miRNAs in addition to their canonical role as a repressor of downstream target genes. Of the bound AGO transcripts are *bona fida* miR-124 target genes in which the 3'UTRs can be repressed in a non-neuronal context, but reverses upon neuronal induction. By examining the mutually exclusive regulation of *PTBP1* and *PTBP2*, we reveal how miR-124 plays a bifunctional role depending on the sequence composition at the 3'UTR, the availability of neuronal ELAVLs, and the interaction with AGOs to mediate the switching of PTB homolog expression during the neuronal conversion of HAFs. Although we focus specifically on the interplay between miR-124 and ELAVL3 for PTBP2 upregulation, future studies should also examine if similar mechanism is used to promote other identified neuronal transcripts or if other RBPs can also synergize with AGOs for such target gene regulation. For example, FXR1, an RBP, has been shown in previous studies to interact with AGOs to facilitate gene expression in non-neuronal cells (Truesdell et al., 2012; Vasudevan et al., 2007; Vasudevan and Steitz, 2007).

The selective role of ELAVL3, and not ubiquitous ELAVL1 or neuronal-specific ELAVL2 and ELAVL4, in mediating PTBP2 induction in neurons highlights the functional specificity of ELAVL family members in neurons. Like ELAVL3, ELAVL1 binds AREs and has been shown to interact with RISC components (Kim et al., 2009; Vasudevan and Steitz, 2007). Although different studies reveal opposing consequence of RISC and ELAVL family interaction on target genes, downstream functional output of AGO-ELAVL is likely context dependent. This context depends on not only the concurrent availability of RBP and target transcript, but also the 3'UTR sequence. Our results clearly define the functional specificity inherent in ELAVL3 that

cannot be replaced by ELAVL1, especially for regulating PTBP2 expression with miR-124 in neurons. We found that the specificity is, at least in part, driven by the hinge region inferred by the region-swapping experiments between ELAVL1 and ELAVL3. As there is no known ARE recognition unique to each ELAVL family member, it is likely that interactors associating with the hinge region may be regulating ELAVL specificity and targeting (Fujiwara et al., 2012; Hinman et al., 2013).

To investigate if the synergism of miR-124 and nELAVLs for transcript stabilization and activation can be generalized to other neuronal transcripts beyond *PTBP2* outside the conversion system, we also knockdown miR-124 and ELAVL3 in primary human neurons. Our results indicate that several neuronal transcripts are induced by miR-124 and ELAVL3 that are critical for neuronal program. Furthermore, by examining existing nELAVL HITS-CLIP datasets in the human brain (Scheckel et al., 2016), we uncovered that miR-124- and nELAVL-mediated upregulation of target transcripts may not be a unique occurrence to *PTBP2*, but likely an overlooked mechanism that maintains gene expression in neurons. Interestingly, as we identified numerous neuronal genes to be targets of miR-124, such as *MAP2, CAMK1D,* and *SEMA6A*, we argue that miR-124 may be critical for enhancing the overall neuronal program as measured by the reduced sodium current, and neurite length and branches through its regulation on long genes. By chemically inhibiting LGE in rat neurons, mimicking the transcriptomic phenotype observed in HNs with reduce miR-124 and ELAVL3 activity, we observed a variety of altered electrical properties. This finding also indicates that miR-9/9*-124 is highly neurogenic as these miRNAs not only allow for the conversion of HAFs into neurons (Abernathy et al. 2017; Yoo et al. 2011), but also enhanced the expression of neuronal markers, such as *MAP2*, when overexpressed during neuronal differentiation of human pluripotent stem cell-derived neurons

(Ishikawa et al., 2020; Sun et al., 2016). Although further tests are required to see if all the identified transcripts targeted by both miR-124 and nELAVLs share the same mechanism as *PTBP2*, our loss-of-function results from in both reprogramming and primary human neuron systems, and its effect on other neuronal genes lend support to the general role of miR-124 as a positive regulator of select target genes in neurons. Future experiments taking a closer look at RNA structure, motif proximity with RBPs, and additional interacting proteins will provide further mechanistic insights to how a single miRNA can simultaneously repress and activate different transcripts in a cell context-dependent manner.

Our study offers insights into the bifunctional mode of miR-124 conferring miRNAs as a reprogramming effector that can contribute to the neuronal program by upregulating specific neuronal genes. As miRNAs have been typically checked for their targets in non-neuronal cell lines, it is plausible that the dual-mode of miRNAs may not be unique to miR-124 in neurons, but instead utilized and altered in other cellular contexts with the help of cell type-specific RBPs. The governance of miRNA activity by the sequences within 3'UTR highlights the role of cell type-specific RBPs as core regulators of gene expression.

References

Abernathy DG, Kim WK, McCoy MJ, Lake AM, Ouwenga R, Lee SW, Xing X, Li D, Lee HJ, Heuckeroth RO, Dougherty JD, Wang T, Yoo AS. 2017a. MicroRNAs Induce a Permissive Chromatin Environment that Enables Neuronal Subtype-Specific Reprogramming of Adult Human Fibroblasts. *Cell Stem Cell* **21**:332-348.e9. doi:10.1016/j.stem.2017.08.002

Bak RO, Hollensen AK, Primo MN, Sorensen CD, Mikkelsen JG. 2013. Potent microRNA suppression by RNA Pol II-transcribed "Tough Decoy" inhibitors. *RNA* **19**:280–293. doi:10.1261/rna.034850.112

Ballas N, Grunseich C, Lu DD, Speh JC, Mandel G. 2005. REST and Its Corepressors Mediate Plasticity of Neuronal Gene Chromatin throughout Neurogenesis. *Cell* **121**:645–657. doi:10.1016/j.cell.2005.03.013

Boutz PL, Stoilov P, Li Q, Lin C-H, Chawla G, Ostrow K, Shiue L, Ares M, Black DL. 2007. A post-transcriptional regulatory switch in polypyrimidine tract-binding proteins reprograms alternative splicing in developing neurons. *Genes & Development* **21**:1636–1652. doi:10.1101/gad.1558107

Cook KB, Kazan H, Zuberi K, Morris Q, Hughes TR. 2011. RBPDB: a database of RNA-binding specificities. *Nucleic Acids Research* **39**:D301–D308. doi:10.1093/nar/gkq1069

Feng J, Liu T, Qin B, Zhang Y, Liu XS. 2012. Identifying ChIP-seq enrichment using MACS. *Nat Protoc* **7**:1728–1740. doi:10.1038/nprot.2012.101

Fujiwara T, Fukao A, Sasano Y, Matsuzaki H, Kikkawa U, Imataka H, Inoue K, Endo S, Sonenberg N, Thoma C, Sakamoto H. 2012. Functional and direct interaction between the RNA binding protein HuD and active Akt1. *Nucleic Acids Research* **40**:1944–1953. doi:10.1093/nar/gkr979

Gabel HW, Kinde B, Stroud H, Gilbert CS, Harmin DA, Kastan NR, Hemberg M, Ebert DH, Greenberg ME. 2015. Disruption of DNA-methylation-dependent long gene repression in Rett syndrome. *Nature* **522**:89–93. doi:10.1038/nature14319

Haraguchi T, Ozaki Y, Iba H. 2009. Vectors expressing efficient RNA decoys achieve the long-term suppression of specific microRNA activity in mammalian cells. *Nucleic Acids Research* **37**:e43–e43. doi:10.1093/nar/gkp040

Hinman MN, Zhou H-L, Sharma A, Lou H. 2013. All three RNA recognition motifs and the hinge region of HuC play distinct roles in the regulation of alternative splicing. *Nucleic Acids Research* **41**:5049–5061. doi:10.1093/nar/gkt166

Iadevaia V, Gerber A. 2015. Combinatorial Control of mRNA Fates by RNA-Binding Proteins and Non-Coding RNAs. *Biomolecules* **5**:2207–2222. doi:10.3390/biom5042207

Ince-Dunn G, Okano HJ, Jensen KB, Park W-Y, Zhong R, Ule J, Mele A, Fak JJ, Yang C, Zhang C, Yoo J, Herre M, Okano H, Noebels JL, Darnell RB. 2012. Neuronal Elav-like (Hu) Proteins Regulate RNA Splicing and Abundance to Control Glutamate Levels and Neuronal Excitability. *Neuron* **75**:1067–1080. doi:10.1016/j.neuron.2012.07.009

Ishikawa M, Aoyama T, Shibata S, Sone T, Miyoshi H, Watanabe H, Nakamura M, Morota S, Uchino H, Yoo AS, Okano H. 2020. miRNA-Based Rapid Differentiation of Purified Neurons from hPSCs Advancestowards Quick Screening for Neuronal Disease Phenotypes In Vitro. *Cells* **9**:532. doi:10.3390/cells9030532

Jiang P, Coller H. 2012. Functional Interactions Between microRNAs and RNA Binding Proteins. *MicroRNA e* **1**:70–79. doi:10.2174/2211536611201010070

Kim HH, Kuwano Y, Srikantan S, Lee EK, Martindale JL, Gorospe M. 2009. HuR recruits let-7/RISC to repress c-Myc expression. *Genes & Development* **23**:1743–1748. doi:10.1101/gad.1812509

King IF, Yandava CN, Mabb AM, Hsiao JS, Huang H-S, Pearson BL, Calabrese JM, Starmer J, Parker JS, Magnuson T, Chamberlain SJ, Philpot BD, Zylka MJ. 2013. Topoisomerases facilitate transcription of long genes linked to autism. *Nature* **501**:58–62. doi:10.1038/nature12504

Lee SW, Oh YM, Lu Y-L, Kim WK, Yoo AS. 2018. MicroRNAs Overcome Cell Fate Barrier by Reducing EZH2-Controlled REST Stability during Neuronal Conversion of Human Adult Fibroblasts. *Developmental Cell* **46**:73-84.e7. doi:10.1016/j.devcel.2018.06.007

Lessard J, Wu JI, Ranish JA, Wan M, Winslow MM, Staahl BT, Wu H, Aebersold R, Graef IA, Crabtree GR. 2007. An Essential Switch in Subunit Composition of a Chromatin Remodeling Complex during Neural Development. *Neuron* **55**:201–215. doi:10.1016/j.neuron.2007.06.019

Li Q, Zheng S, Han A, Lin C-H, Stoilov P, Fu X-D, Black DL. 2014. The splicing regulator PTBP2 controls a program of embryonic splicing required for neuronal maturation. *eLife* **3**. doi:10.7554/eLife.01201

Licatalosi DD, Yano M, Fak JJ, Mele A, Grabinski SE, Zhang C, Darnell RB. 2012. Ptbp2 represses adult-specific splicing to regulate the generation of neuronal precursors in the embryonic brain. *Genes & Development* **26**:1626–1642. doi:10.1101/gad.191338.112

Lin K, Zhang S, Shi Q, Zhu M, Gao L, Xia W, Geng B, Zheng Z, Xu EY. 2018. Essential requirement of mammalian *Pumilio* family in embryonic development. *MBoC* **29**:2922–2932. doi:10.1091/mbc.E18-06-0369

Lu J, Ji H, Tang H, Xu Z. 2018. microRNA-124a suppresses PHF19 over-expression, EZH2 hyper-activation, and aberrant cell proliferation in human glioma. *Biochemical and Biophysical Research Communications* **503**:1610–1617. doi:10.1016/j.bbrc.2018.07.089

Mabb AM, Kullmann PHM, Twomey MA, Miriyala J, Philpot BD, Zylka MJ. 2014. Topoisomerase 1 inhibition reversibly impairs synaptic function. *Proc Natl Acad Sci USA* **111**:17290–17295. doi:10.1073/pnas.1413204111

Mabb AM, Simon JM, King IF, Lee H-M, An L-K, Philpot BD, Zylka MJ. 2016. Topoisomerase 1 Regulates Gene Expression in Neurons through Cleavage Complex-Dependent and -Independent Mechanisms. *PLoS ONE* **11**:e0156439. doi:10.1371/journal.pone.0156439

Makeyev EV, Zhang J, Carrasco MA, Maniatis T. 2007. The MicroRNA miR-124 Promotes Neuronal Differentiation by Triggering Brain-Specific Alternative Pre-mRNA Splicing. *Molecular Cell* **27**:435–448. doi:10.1016/j.molcel.2007.07.015

McCoy MJ, Fire AZ. 2020. Intron and gene size expansion during nervous system evolution. *BMC Genomics* **21**:360. doi:10.1186/s12864-020-6760-4

McCoy MJ, Paul AJ, Victor MB, Richner M, Gabel HW, Gong H, Yoo AS, Ahn T-H. 2018. LONGO: an R package for interactive gene length dependent analysis for neuronal identity. *Bioinformatics* **34**:i422–i428. doi:10.1093/bioinformatics/bty243

McQuin C, Goodman A, Chernyshev V, Kamentsky L, Cimini BA, Karhohs KW, Doan M, Ding L, Rafelski SM, Thirstrup D, Wiegraebe W, Singh S, Becker T, Caicedo JC, Carpenter AE. 2018. CellProfiler 3.0: Next-generation image processing for biology. *PLoS Biol* **16**:e2005970. doi:10.1371/journal.pbio.2005970

Moore MJ, Zhang C, Gantman EC, Mele A, Darnell JC, Darnell RB. 2014. Mapping Argonaute and conventional RNA-binding protein interactions with RNA at single-nucleotide resolution using HITS-CLIP and CIMS analysis. *Nat Protoc* **9**:263–293. doi:10.1038/nprot.2014.012

Neo WH, Yap K, Lee SH, Looi LS, Khandelia P, Neo SX, Makeyev EV, Su I. 2014. MicroRNA miR-124 Controls the Choice between Neuronal and Astrocyte Differentiation by Fine-tuning Ezh2 Expression. *Journal of Biological Chemistry* **289**:20788–20801. doi:10.1074/jbc.M113.525493

Okano HJ, Darnell RB. 1997. A Hierarchy of Hu RNA Binding Proteins in Developing and Adult Neurons. *The Journal of Neuroscience* **17**:3024–3037. doi:10.1523/JNEUROSCI.17-09-03024.1997

Packer AN, Xing Y, Harper SQ, Jones L, Davidson BL. 2008. The Bifunctional microRNA miR-9/miR-9* Regulates REST and CoREST and Is Downregulated in Huntington's Disease. *Journal of Neuroscience* **28**:14341–14346. doi:10.1523/JNEUROSCI.2390-08.2008

Partek Inc. 2020. Partek Flow. St. Louis.

Paz I, Kosti I, Ares M, Cline M, Mandel-Gutfreund Y. 2014. RBPmap: a web server for mapping binding sites of RNA-binding proteins. *Nucleic Acids Research* **42**:W361–W367. doi:10.1093/nar/gku406

Plass M, Rasmussen SH, Krogh A. 2017. Highly accessible AU-rich regions in 3' untranslated regions are hotspots for binding of regulatory factors. *PLOS Computational Biology* **13**:e1005460. doi:10.1371/journal.pcbi.1005460

Rehmsmeier M. 2004. Fast and effective prediction of microRNA/target duplexes. *RNA* **10**:1507–1517. doi:10.1261/rna.5248604

Richner M, Victor MB, Liu Y, Abernathy D, Yoo AS. 2015. MicroRNA-based conversion of human fibroblasts into striatal medium spiny neurons. *Nature Protocols* **10**:1543–1555. doi:10.1038/nprot.2015.102

Robinson MD, McCarthy DJ, Smyth GK. 2010. edgeR: a Bioconductor package for differential expression analysis of digital gene expression data. *Bioinformatics* **26**:139–140. doi:10.1093/bioinformatics/btp616

Scheckel C, Drapeau E, Frias MA, Park CY, Fak J, Zucker-Scharff I, Kou Y, Haroutunian V, Ma'ayan A, Buxbaum JD, Darnell RB. 2016. Regulatory consequences of neuronal ELAV-like protein binding to coding and non-coding RNAs in human brain. *eLife* **5**. doi:10.7554/eLife.10421

Schoenherr C, Anderson D. 1995. The neuron-restrictive silencer factor (NRSF): a coordinate repressor of multiple neuron-specific genes. *Science* **267**:1360–1363. doi:10.1126/science.7871435

Spassov DS, Jurecic R. 2002. Cloning and comparative sequence analysis of PUM1 and PUM2 genes, human members of the Pumilio family of RNA-binding proteinsq 10.

Staahl BT, Tang J, Wu W, Sun A, Gitler AD, Yoo AS, Crabtree GR. 2013. Kinetic Analysis of npBAF to nBAF Switching Reveals Exchange of SS18 with CREST and Integration with Neural Developmental Pathways. *Journal of Neuroscience* **33**:10348–10361. doi:10.1523/JNEUROSCI.1258-13.2013

Sugino K, Hempel CM, Okaty BW, Arnson HA, Kato S, Dani VS, Nelson SB. 2014. Cell-Type-Specific Repression by Methyl-CpG-Binding Protein 2 Is Biased toward Long Genes. *Journal of Neuroscience* **34**:12877–12883. doi:10.1523/JNEUROSCI.2674-14.2014

Sun AX, Yuan Q, Tan S, Xiao Y, Wang D, Khoo ATT, Sani L, Tran H-D, Kim P, Chiew YS, Lee KJ, Yen Y-C, Ng HH, Lim B, Je HS. 2016. Direct Induction and Functional Maturation of Forebrain GABAergic Neurons from Human Pluripotent Stem Cells. *Cell Reports* **16**:1942–1953. doi:10.1016/j.celrep.2016.07.035

Tripathi S, Pohl MO, Zhou Y, Rodriguez-Frandsen A, Wang G, Stein DA, Moulton HM, DeJesus P, Che J, Mulder LCF, Yángüez E, Andenmatten D, Pache L, Manicassamy B, Albrecht RA, Gonzalez MG, Nguyen Q, Brass A, Elledge S, White M, Shapira S, Hacohen N, Karlas A, Meyer TF, Shales M, Gatorano A, Johnson JR, Jang G, Johnson T, Verschueren E, Sanders D, Krogan N, Shaw M, König R, Stertz S, García-Sastre A, Chanda SK. 2015. Meta- and Orthogonal Integration of Influenza "OMICs" Data Defines a Role for UBR4 in Virus Budding. *Cell Host & Microbe* **18**:723–735. doi:10.1016/j.chom.2015.11.002

Truesdell SS, Mortensen RD, Seo M, Schroeder JC, Lee JH, LeTonqueze O, Vasudevan S. 2012. MicroRNA-mediated mRNA Translation Activation in Quiescent Cells and Oocytes Involves Recruitment of a Nuclear microRNP. *Scientific Reports* **2**. doi:10.1038/srep00842

Tsutsui Ken, Tsutsui Kimiko, Sano K, Kikuchi A, Tokunaga A. 2001. Involvement of DNA Topoisomerase IIβ in Neuronal Differentiation. *Journal of Biological Chemistry* **276**:5769–5778. doi:10.1074/jbc.M008517200

Vasudevan S, Steitz JA. 2007. AU-Rich-Element-Mediated Upregulation of Translation by FXR1 and Argonaute 2. *Cell* **128**:1105–1118. doi:10.1016/j.cell.2007.01.038

Vasudevan S, Tong Y, Steitz JA. 2007. Switching from Repression to Activation: MicroRNAs Can Up-Regulate Translation. *Science* **318**:1931–1934. doi:10.1126/science.1149460

Victor MB, Richner M, Hermanstyne TO, Ransdell JL, Sobieski C, Deng P-Y, Klyachko VA, Nerbonne JM, Yoo AS. 2014. Generation of Human Striatal Neurons by MicroRNA-Dependent Direct Conversion of Fibroblasts. *Neuron* **84**:311–323. doi:10.1016/j.neuron.2014.10.016

Victor MB, Richner M, Olsen HE, Lee SW, Monteys AM, Ma C, Huh CJ, Zhang B, Davidson BL, Yang XW, Yoo AS. 2018. Striatal neurons directly converted from Huntington's disease patient fibroblasts recapitulate age-associated disease phenotypes. *Nature Neuroscience*. doi:10.1038/s41593-018-0075-7

Visvanathan J, Lee S, Lee B, Lee JW, Lee S-K. 2007. The microRNA miR-124 antagonizes the anti-neural REST/SCP1 pathway during embryonic CNS development. *Genes & Development* **21**:744–749. doi:10.1101/gad.1519107

Vuong JK, Lin C-H, Zhang M, Chen L, Black DL, Zheng S. 2016. PTBP1 and PTBP2 Serve Both Specific and Redundant Functions in Neuronal Pre-mRNA Splicing. *Cell Reports* **17**:2766–2775. doi:10.1016/j.celrep.2016.11.034

Watanabe M, Tsutsui Ken, Tsutsui Kimiko, Inoue Y. 1994. Differential expressions of the topoisomerase IIa and IIb mRNAs in developing rat brain. *Neuroscience Research* **19**:51–57.

Xue Y, Qian H, Hu J, Zhou B, Zhou Y, Hu X, Karakhanyan A, Pang Z, Fu X-D. 2016. Sequential regulatory loops as key gatekeepers for neuronal reprogramming in human cells. *Nature Neuroscience* **19**:807–815. doi:10.1038/nn.4297

Yoo AS, Staahl BT, Chen L, Crabtree GR. 2009. MicroRNA-mediated switching of chromatin-remodelling complexes in neural development. *Nature* **460**:642–646. doi:10.1038/nature08139

Yoo AS, Sun AX, Li L, Shcheglovitov A, Portmann T, Li Y, Lee-Messer C, Dolmetsch RE, Tsien RW, Crabtree GR. 2011. MicroRNA-mediated conversion of human fibroblasts to neurons. *Nature* **476**:228–231. doi:10.1038/nature10323

Yu H, Wang J, Sheng Q, Liu Q, Shyr Y. 2018. beRBP: binding estimation for human RNA-binding proteins. *Nucleic Acids Research*. doi:10.1093/nar/gky1294

Zhang Y, Liu T, Meyer CA, Eeckhoute J, Johnson DS, Bernstein BE, Nussbaum C, Myers RM, Brown M, Li W, Liu XS. 2008. Model-based Analysis of ChIP-Seq (MACS). *Genome Biol* **9**:R137. doi:10.1186/gb-2008-9-9-r137

Zheng S, Gray EE, Chawla G, Porse BT, O'Dell TJ, Black DL. 2012. PSD-95 is post-transcriptionally repressed during early neural development by PTBP1 and PTBP2. *Nature Neuroscience* **15**:381–388. doi:10.1038/nn.3026

Zhou S, Gao R, Hu W, Qian T, Wang N, Ding G, Ding F, Yu B, Gu X. 2014. miR-9 inhibits Schwann cell migration by targeting Cthrc1 following sciatic nerve injury. *Journal of Cell Science* **127**:967–976. doi:10.1242/jcs.131672